Casimir Forces and Geometry

Inaugural-Dissertation
zur
Erlangung des Doktorgrades
der Mathematisch-Naturwissenschaftlichen Fakultät
der Universität zu Köln

vorgelegt von
Rauno Büscher
aus Göttingen

2005

Berichterstatter: Prof. Dr. A. Altland
Prof. Dr. A. Rosch
Dr. T. Emig

Tag der mündlichen Prüfung: 6. Juli 2005

Abstract

Casimir interactions are interactions induced by quantum vacuum fluctuations and thermal fluctuations of the electromagnetic field. Using a path integral quantization for the gauge field, an effective Gaussian action will be derived which is the starting point to compute Casimir forces between macroscopic objects analytically and numerically. No assumptions about the independence of the material and shape dependent contributions to the interaction are made. We study the limit of flat surfaces in further detail and obtain a concise derivation of Lifshitz' theory of molecular forces [73]. For the case of ideally conducting boundaries, the Gaussian action will be calculated explicitly. Both limiting cases are also discussed within the framework of a scalar field quantization approach, which is applicable for translationally invariant geometries. We develop a non–perturbative approach to calculate the Casimir interaction from the Gaussian action for periodically deformed and ideally conducting objects numerically. The obtained results reveal two different scaling regimes for the Casimir force as a function of the distance between the objects, their deformation wavelength and amplitude. The results confirm that the interaction is non–additive, especially in the presence of strong geometric deformations. Furthermore, the numerical approach is extended to calculate lateral Casimir forces. The results are consistent with the results of the proximity–force approximation for large deformation wavelengths. A qualitatively different behaviour between the normal and lateral force is revealed. We also establish a relation between the boundary induced change of the density of states for the scalar Helmholtz equation and the Casimir interaction using the path integral method. For statically deformed boundaries, this relation can be expressed as a novel trace formula, which is formally similar to the so–called Krein–Friedel–Lloyd formula [64]. While the latter formula describes the density of states in terms of the S–matrix of quantum scattering at potentials, the new trace formula is applied to the free Green function, evaluated at the boundary surfaces of the confining geometry. This latter formulation is non–approximative and hence exact.

Contents

A Introduction

1 Fluctuation induced interactions

Casimir interactions are one of the manifestations of quantum physics which can not be explained classically. The classical notion of vacuum is an empty space where all particles are removed. Imagine this classical vacuum being free of fields, so that quantum mechanical particles as photons are also removed. The problem now is that classical voidness has no quantum mechanical analogon. Heisenbergs uncertainty principle sets the limit of knowledge of pairs of physical parameters as the position x and the momentum p of a particle to the order of Planck's constant, $\Delta x \cdot \Delta p \geq \hbar/2$. Another pairing is time and energy, $\Delta E \cdot \Delta t \geq \hbar/2$, which forbids the precise knowledge of an unique value for the energy of a system at a unique point in time. The quantum mechanical solution is to assume the existence of *fluctuations*. Particles are smeared out by considering them as probability distributions with a finite width around an average value (which corresponds to the classical point–like value), they can *merge* "virtually" within a given time interval and carry an energy which is allowed by the time–energy uncertainty relation. Quantum mechanics allows for the existence of zero–point energy, and a foam of virtual particles and fields in the "vacuum". Since the geometry of spacetime and the existence of particles and fields are linked with each other, the fluctuations on Planck scale also concern the topology of spacetime itself, see Fig. A.1.

Naturally, the question arises if these quantum fluctuations can have an influence on the interaction of microscopic or even macroscopic objects. This is in fact the case. To begin with, the notion of fluctuation induced interactions shall be clarified from a more general point of view. Obviously, fluctuations exist at small length scales, but not merely there. They can also be of classical or thermal nature. To capture an idea of interactions caused by fluctuations, a fluctuating medium is to be considered, as e.g. the zero point fluctuations of the electromagnetic field, and secondly, objects which are immersed into that medium. In case of the electromagnetic field, one can think of atoms, dipole molecules or more macroscopic objects like conductors. If the mere presence of the objects modifies the fluctuations, these objects will get into interaction *via the change of the fluctuations of the medium*. For example, the surface of a conductor poses the constraint that the tangential components

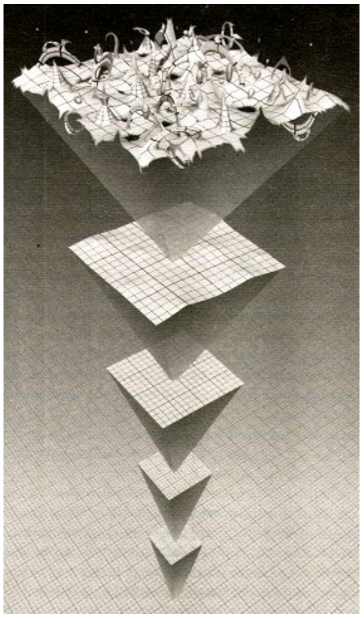

Figure A.1: Fluctuating space–time. (see www.casimir.rl.ac.uk)

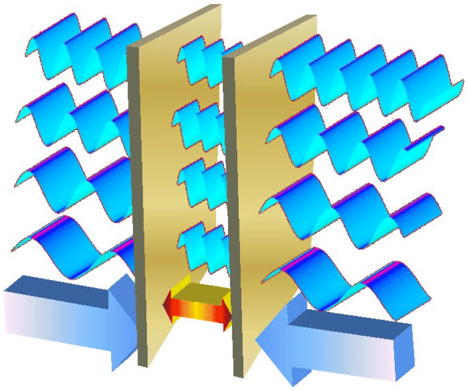

Figure A.2: Fluctuation induced pressure. (see www.casimir.rl.ac.uk)

of the electric field vanish on it. This suppresses some fluctuations of the zero point field compared to the space *without* the conductor. This *change* of fluctuations determines the interaction between the conductor surfaces. An example for thermal fluctuations is given by the Brownian motion of a particle. The locations of the particle are characterized by a Boltzmann distribution $e^{-U(r)/k_{\rm B}T}$ with the potential $U(r)$ at each positions. Fluctuations in the movement are then of the order $\sim k_{\rm B}T$. The van–der–Waals force provides an example for classical fluctuation induced forces.

Fluctuation induced interactions between objects depend on the characteristic features of the objects as their topology or material properties. These features take influence on the boundary constraints which are imposed on the fluctuating field. On the other hand, the kind of field on which these conditions are imposed govern the interaction between the objects.

Fluctuation induced interactions have a broad range of relevance, cf. Refs. [83, 78, 14, 91]. To give some examples, they are important e.g. in cosmology since they are related to zero point energies of fields [111]. Fluctuations of gluon fields confined by boundaries were discussed in [81, 82], see also [21]. But they are also important in exotic areas such as the physics related to biological problems including the dynamic behaviour of membranes [92, 93, 47, 85, 86], or the sticking of large molecules as proteins on membranes which is related to the theory of correlated fluids [60].

The Casimir force is a striking example that vacuum fluctuations are not merely a theoretical construct but have *real* consequences. This makes the Casimir effect globally significant not only to quantum physics, but in all fields where fluctuation induced phenomena occur, cf. [56, 78, 83, 60].

We return to the quantum fluctuations of the electromagnetic field. While quantum fluctuations can be expected for any quantum field, especially for the electromagnetic field, which is a long ranged fundamental interaction, measurable effects can be expected. The zero point energy of the vacuum state is formally infinite and it is commonly disregarded by normal ordering the Hamiltonian, since it is a constant which commutes with the creation and annihilation operators of photons and has therefore no influence on the quantum dynamics governed by the Heisenberg equations of motion. However, the vacuum energy is not arbitrary and subject to *changes* due to boundary constraints. In fact, these are *observable*, as predicted by Hendrik Casimir in the year 1948 [22]. Between two infinitely extended parallel conducting plates at distance H, Casimir predicted an *attractive* force per surface area A of

$$\frac{F_0}{A} = -\frac{\pi^2}{240}\frac{\hbar c}{H^4} \tag{A1.1}$$

at zero temperature.

Figure A.3: Hendrik Brugt Gerhard Casimir (1909 – 2000). (see www.casimir.rl.ac.uk)

The presence of the plates constricts the quantized normal photon modes in the cavity between the plates. They are described by harmonic oscillators with wave vector $\mathbf{k} = (k_x, k_y, \pi n/H)$ and frequency $\omega(\mathbf{k}) = c|\mathbf{k}|$, and their ground state energy is $\hbar\omega(\mathbf{k})/2$. The ground state energy of the vacuum in the presence of the two plates is given by the sum over all modes of these energy contributions, $\hbar/2\sum_{\mathbf{k}}\omega(\mathbf{k})$. This zero point energy is formally infinite and must be regularized, which can be done by subtracting the asymptotic expression of the sum for infinite surface distance. The force F_0 is given by the derivative of the regularized energy with respect to the plate distance. A detailed calculation is given e.g. in Ref. [78]. The boundary induced restrictions to the field fluctuations inside the gap between the surfaces and outside beyond the gap leads to a difference of radiation pressures of the fluctuating zero point field, which induces the *attractive* Casimir force between the surfaces.

This is illustrated in Fig. A.2. Historically, Casimir's work was rooted in studies of colloidal suspensions. The stability of those suspensions was explained by the interplay of repulsive and attractive forces, where the attractive force was attributed to the London van–der–Waals interaction at short distances. Experiments showed that for large colloidal molecules [110], retardation due to the finite velocity of light has to be taken into account for the interaction. Casimir and Polder [23] demonstrated that the London van–der–Waals inter atomic potential $U(r) \sim -r^{-6}$ is modified by retardation and falls of as $U(r) \sim -\alpha_1\alpha_2\hbar c/r^7$, where α_1, α_2 are the static polarizabilities of the interacting molecules. For a deeper understanding of this result and inspired by an advice from Bohr, who noted that the van–der–Waals force "must have something to do with zero point energy", Casimir found that the retarded van–der–Waals interaction between fluctuating dipoles can be related to the change of the zero point energy of the electromagnetic field generated by the presence of the dipoles. This thread gave the motivation to consider metallic plates.

The first experiments to detect Casimir interactions macroscopically were performed by Abricosova and Derjaguin in 1951 with dielectric materials [28, 29], namely with a flat glass plate and spherical lenses with radii of $R = 10$ cm and $R = 25$ cm. The distance between the plate and the lenses were taken between $H = 0.07\mu$m and $H = 0.5\mu$m. This configuration is easier to adjust than the exact parallelization of two flat plates. The finite curvature of the lens can be well accounted for by the "Derjarguin approximation" [27] or proximity force approximation (PFA). The PFA method considers the sum of local contributions to the interaction from small flat surface elements opposite to each other, assuming that they behave as infinitesimally small parallel plates. This phenomenological approach is restricted to surfaces that have a small degree of non-parallelism. This is a small local curvature in the case of curved surfaces, as in Derjaguin's experiments for a plate and a sphere, where the radius of the sphere is much larger than the minimum distance between the surfaces. However, if the curvature becomes larger, the distance between the small flat surface elements changes rapidly, it can no longer be determined unambiguously, see Fig. A.4, and the assumption of summing local contribution becomes unreliable due to diffraction effects.

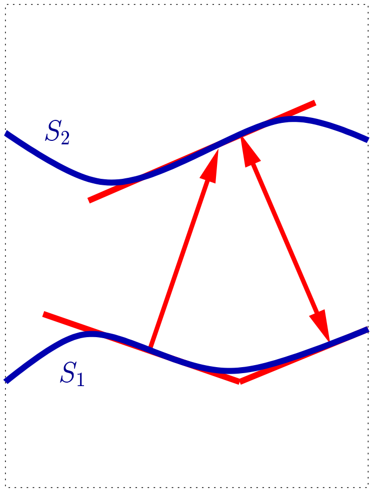

Figure A.4: Proximity force approximation (PFA). The curved boundary surfaces are approximated locally by flat surface segments.

Experiments with flat glass plates with distances between $H = 0.6\mu$m and $H = 1.5\mu$m were performed by Overbeek and Sparnaay (1954) [95]. The first experiment with conducting aluminium plates to verify Eq. (A1.1) was performed by Sparnaay (1958) [102] at distances between $H = 0.5\mu$m and $H = 2\mu$m. The results agreed qualitatively with Casimir's prediction, at best. Further early experiments are reviewed in [55]. Their problems were mainly technical, e.g. the alignment of the plates or the avoidance of residual charges. But later high precision experiments [68, 87] confirm Casimir's theoretical prediction to high accuracy. These experiments will be discussed in the following section in more detail.

The assumption of perfect conductivity of the surfaces which led to Eq. (A1.1), is idealized. These surfaces are reflecting for the electromagnetic spectrum at all wavelengths. However, since any real metal becomes transparent for frequencies larger than the plasma frequency of the material, a frequency cutoff is effectively posed by real surfaces. Since the main contribution to the force results from modes with wavelengths of the order of the surface distance, Eq. (A1.1) is expected to hold if the distance H between the surfaces is large compared to the plasma wavelength λ_p, which is of the order of 0.1 to 10 microns in recent experiments. For smaller H, the force will be reduced compared to the ideal result F_0 in Eq. (A1.1).

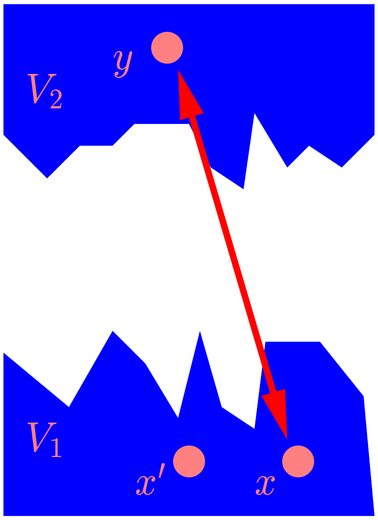

Figure A.5: Pair–wise summation of potentials (PWS) to calculate van–der–Waals forces between macroscopic bodies of arbitrary shape. The interaction between two dipoles x and y is not independent from the presence of other dipoles, as x'.

On the theoretical side, a way to include finitely conducting boundaries is to consider the van–der–Waals interaction of fluctuating dipoles in the materials and to sum over the pair–wise contributions of the dipole interaction. This approximative method is known as pair–wise summation of potentials (PWS). However, it was early recognized that the van–der–Waals interaction is in general not additive, i.e. the interaction between two atoms is *influenced* by the presence of a third atom, see Fig. A.5. The additivity assumption is justified for dilute media only, where the distances between the interacting molecules are large. The alteration of the interaction due to the additivity assumption is illustrated by a model calculation in Ref. [78], which shows that the pair–wise summation of Casimir–Polder potentials between a single molecule and an infinite conducting half space leads to a force which is about 80% of the real Casimir force between them.

The discrepancies between the results from the early experiments with dielectric materials and the theoretical results based on this microscopic assumption of pair wise additivity of intermolecular Casimir–Polder potentials for the van–der–Waals interaction gave the stimulus to search for a theoretical description which allows for finite conductivity beyond the microscopic additivity assumption.

This was achieved by Lifshitz in 1956, who developed a *macroscopic* theory of the fluctuation induced forces between dielectrics [73], see also [69], by treating the dielectric matter as continua with a frequency dependent dielectric susceptibility $\epsilon(\omega)$. In the limit of ideal conductivity, Lifshitz' result reduces to Casimir's result, cf. Eq. (A1.1). In the opposite limit of dielectric susceptibilities close to unity, the result is in coincidence with the microscopic approach of pair–wise summation of retarded van–der–Waals potentials [31, 32]. Lifshitz solved Maxwell's equations in two half spaces filled with dielectric media and in the vacuum gap in between with the standard matching conditions at the boundary surfaces. In general, any dielectric medium can be assumed instead of the vacuum gap. The equations read

$$\nabla \times \mathbf{E} = \frac{i\omega}{c}\mathbf{B}, \tag{A1.2}$$

$$\nabla \times \mathbf{B} = -\frac{i\omega}{c}\epsilon(\omega)\mathbf{E} - \frac{i\omega}{c}\mathbf{K}. \tag{A1.3}$$

Here, a random source field $\mathbf{K}$ is introduced to account for the quantum fluctuations of the field. The fluctuation–dissipation relation enforces the correlations

$$\left\langle K_i(\mathbf{x})K_j(\mathbf{x}')\right\rangle = 2\hbar\,\mathrm{Im}\,\epsilon(\omega)\,\delta_{ij}\delta^{(3)}\left(\mathbf{x}-\mathbf{x}'\right), \tag{A1.4}$$

so that only the dissipative part of the dielectric function described by $\mathrm{Im}\,\epsilon(\omega)$ matters. From this relation, correlation functions for the fields are calculated, and from the latter, the Maxwell stress tensor is obtained. The Casimir pressure onto the (flat) surfaces is then calculated from the zz–component of the stress tensor. The Lifshitz theory for the interaction of dielectric media is generally accepted as to the description of Casimir forces between real dielectric media since it had been supported by accurate experiments which measure the thinning of liquid Helium films with an acoustic interferometry technique [96]. Further experiments confirming the Lifshitz theory were performed by Van Blokland and Overbeek 1978 [106] on chromium. Other experiments are reviewed by Derjaguin et. al. [30] and Sparnaay [103], a more recent review is provided by Elizalde et. al. [33].

In 1968, van Kampen and collaborators [107] rederived the Lifshitz theory in the non–retarded limit. The concept behind their approach was similar to Casimir's idea of considering the fluctuations of the zero point energy, but with dielectric boundaries instead of ideal metals. This approach was extended in 1973 to the general case including retardation [70, 99]. But in this approach, absorption does not show up explicitly, which is reflected by the fact that only a real dielectric function occurs, contrary to the Lifshitz theory which is based on the fluctuation–dissipation–relation and requires for a complex dielectric function. Barash and Ginzburg proved the equivalence of both approaches in 1973 [10].

An alternative approach to the description of Casimir forces without direct reference to the fluctuations of the vacuum field was provided by Schwinger's source theory in the year 1978 [100, 101], see also [77, 80]. Schwinger considers the radiation reaction or source fields induced between dipoles to derive the Casimir forces. However, the dipole radiation reaction field is linked to the fluctuating zero point field by the fluctuation–dissipation relation. This explains the deducibility of the Casimir force using Schwinger's more unconventional concept of source fields and thus the equivalence to Casimir's vacuum field approach, although the physical premises of both approaches appear to be different. In fact, the normal ordering of equal time Heisenberg–picture photon operators avoids an immediate reference to the zero point vacuum field and *requires* the source field description. This kind of dual description either via source fields or via the vacuum field had also been performed for the Lamb shift [65].

Although the Lifshitz theory was a significant advance in the theoretical description of macroscopic van–der–Waals or Casimir interactions between real matter, its applicability to general geometries is limited. The problem with Lifshitz' approach is that it is not suited to surfaces with arbitrary deformations, because then, the solution of Maxwell's equations in different regions with matching conditions at the boundary surfaces becomes unpracticable. This difficulty equally applies to the approach of van Kampen and collaborators, who also considered the problem of half spaces separated by infinitely extended flat planes as boundaries. However, the Casimir interaction is expected to be strongly dependent on geometry, and, even the sign of the interaction can vary with geometry, as shown by Boyer, who predicted a *repulsive* Casimir interaction for an ideally conducting sphere [18]. In contrast to that, the local van–der–Waals interaction between two single neutral molecules is always *attractive*. This distinct microscopic and macroscopic behaviour underlines the non–additivity of fluctuation forces.

The important and natural question is how the successful Lifshitz theory can be generalized to include surface deformations. Corrections due to geometric deformations and material dependent or thermal corrections to the ideal Casimir force in Eq. (A1.1) had been discussed independently so far. This seems to be reasonable for the case that the characteristic length scales of each of the modifications are widely different from each other. However, this assumption is often not justified.

So far, the proximity–approximation method had mostly been used to account for geometries in experiments which are "similar" to the system of two flat plates, as e. g. the geometry consisting of a plate and a sphere where $R \gg H$. In arbitrary geometries, however, the PFA can no longer be expected to be applicable, since it becomes unreliable for objects with large curvatures. Contrary to that, the PWS is not affected by short scale changes of the surface structure at small distances. To take the non–additivity of the interaction into account, Mostepanenko and Sokolov [89] proposed a normalization of the Casimir–Polder potential such that the pair–wise summation over two half spaces at distance H yields the exact result for two flat plates. However, correlation effects between surface deformations and the non–additivity are not taken into account by performing this normalization.

On the theoretical side, the changeover to the generalization of the description of the most simple system of two flat plates to systems with deformed surfaces is non–trivial even for ideal metals. It is not merely a technical difficulty, but rather of fundamental nature and closely related to the spectral theory of quantum systems confined by arbitrary geometries [39]. The famous question "Can one hear the shape of a drum ?" was posed by Kac in 1966 [59], illustrating the problem of deducing the shape of a region from its resonance spectrum. 26 years later, this question was negated [51], however, the inverse problem of characterizing the resonance spectrum for a given geometry is not yet solved in general. Pioneering work in this field had been done by Balian and Bloch [2, 3, 4, 5, 6], and Duplantier [7]. Balian and Bloch studied the scalar field wave equation by means of multiple reflection expansions for a closed cavity [2]. This work was extended to the characterization of electromagnetic eigenmodes in cavities [3] and the study of geometric properties of the eigenmodes [5]. A semi-classical calculation of the Green function of a quantum mechanical system which is related to the resonance spectrum was developed by Gutzwiller [52] by considering only closed orbits in phase space. These concepts of spectral theory are closely related to the Casimir problem. The Casimir interaction is highly sensitive to variations of the geometric boundaries, this sensitivity translates to the spectrum $\{\omega(\mathbf{k})\}$ of eigenfrequencies of the photon modes. The analytic knowledge of the spectrum would imply a solution of the Casimir problem for arbitrary geometries. The multiple scattering approach was later considered for the Casimir interaction by Balian and Duplantier [7, 8], it reduces to ray optics in the limit of high frequencies. Recently, Jaffe and collaborators [58] proposed a new approach to calculate the Casimir interaction between deformed metals based on ray optics considering the contributions of all classical optical paths between the boundary surfaces. Schaden and Spruch [97, 98] applied Gutzwiller's semi-classical approach to calculate the Casimir interaction in some simple geometries of ideal metals, as plate and sphere.

Thermal corrections to the Casimir force were also accounted for by Lifshitz [73]. Later in 1967, Mehra [76] inferred from a quantum statistical calculation an additional temperature correction which does not appear in Lifshitz' theory. It was stated that corrections due to thermal fluctuations become important for distances beyond 3μm. At $T \approx 300K$, where most experiments are performed, the de Broglie wavelength of photons is $\lambda_T = \frac{\hbar c}{k_B T} \approx 7\mu$m. It was postulated that temperature increases the force by 15% at a plate distance of 3μm [61]. Since a deviation from Casimir's prediction of this magnitude was not observed in the measurement of Lamoreaux [68], the influence of temperature on the Casimir interaction is an object of current debate [84]. Since the dominant contribution to the force results from frequencies $\omega \sim H^{-1}$, for experiments in the range of $H \approx 1\mu$m, the dominant contributions are from frequencies in the infrared and visible regime, where the Drude model $\epsilon(\omega) = 1 - \omega_{\rm p}^2/\omega^2$ is proposed as to describe real metals [66, 67], where $\omega_{\rm p}$ is the plasma frequency of the metal.

The quantum field theoretical treatment of the Casimir effect with path integral quantization was introduced in 1984 by Bordag, Robaschik and Wieczorek [15], later in 1991 independently also by Li and Kardar [71, 72], who considered the interaction of deformed manifolds in a fluid with long ranged correlations. This approach allows to include arbitrarily deformed manifolds on which any kind of boundary condition can be implemented. This feature makes the approach promising for an analysis of arbitrary geometries. Emig et. al. [35, 36] developed a perturbation theory for the deformation of ideally conducting surfaces based on this method. Finite conductivity can be accounted for by a suitable choice of boundary conditions. The field theoretical approach is also interesting for the dynamic Casimir effect, where the interacting objects are not assumed to be stationary. The dynamic Casimir effect includes moving objects or fluctuating surfaces, as membranes. The creation of radiation by moving mirrors was studied for a one dimensional cavity [88]. This has received attention due to its connections to Hawking and Unruh effects which describe the radiation from black holes and accelerated masses, respectively. A deeper understanding of these connections is expected to be beneficial for QED, relativity and cosmology [111, 26].

2 High precision experiments and applications

While Sparnaay's Casimir force measurement in 1958 [102] could only assert a qualitative coincidence with Casimir's result Eq. (A1.1) and the uncertainty was about 100%, in the year 1997 S. K. Lamoreaux measured the Casimir force between a spherical lens of radius $R = 11.3 \pm 0.1$ cm and a flat plate with a diameter of 2.54 cm at distances between 0.6μm and 6μm in an evacuated vessel [68]. The lens is fixed at a micro-positioning device controlled by a piezoelectric stack, while the flat plate is mounted onto one arm of a torsion pendulum. Both the lens and the plate were gold coated. The other arm of the pendulum is connected to the central electrode of a pair of planar capacitors. Applying voltages to the capacitors allow for a measurement of the restoring force required to balance the pendulum for any torque caused by the Casimir force between lens and sphere. This way, Casimir's prediction could be verified within 5% of accuracy.

Roy and Mohideen [87] performed an improved measurement with an atomic force microscope and reached an agreement between experiment and theory of up to 1%. They used a similar geometric setup with an aluminium coated polystyrene sphere of a diameter of $200 \pm 4\mu$m mounted on a cantilever, see Fig. A.7. The distance to the aluminium coated plate was taken in the range of 0.1μm to 0.9μm. Instead of a torsion pendulum, a deviation of the distance between plate and sphere is detected by a laser beam reflected at the cantilever, which is registered by a pair of photo diodes. A piezo stack is used to bring the flat plate close to the sphere, see Fig. A.7.

In a similar experimental assembly, Chen, Mohideen and co–workers in 2002 [25] demonstrated the existence of *lateral* Casimir forces predicted before [35, 36] which act tangentially between deformed surfaces. They used a plate with uniaxial sinusoidal corrugation of period 1.2μm and a sphere of the same diameter of $200 \pm 4\mu$m with gold coating, on which another sinusoidal corrugation with different amplitude was imprinted. The amplitudes of corrugation on the sphere and the plate were measured with the atomic force microscope as 59 ± 7 nm and 8 ± 1 nm, respectively. The lateral force was measured for a mean distance (which is understood to be the minimum distance between plate and sphere *without* the corrugation) in the range between 0.2μm and 0.3μm. The measured force exhibits the periodicity corresponding to the corrugations.

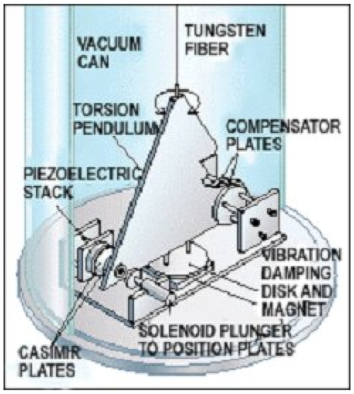

Figure A.6: Experimental setup of Lamoreaux. Picture from Scientific American & S. K. Lamoreaux.

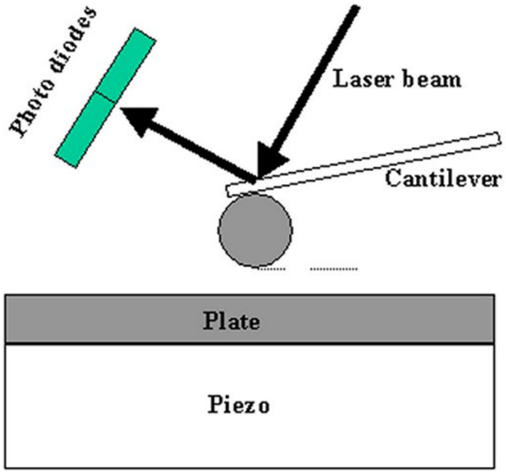

Figure A.7: Mohideen's experiment [87].

A few months prior to this experiment, Chan et. al. at the Bell Laboratories of Lucent Technologies recognized the influence of the Casimir force on Micro– and Nano–electromechanical systems (MEMS,NEMS) due to their topological nature associated with the dependence on the boundary of the electromagnetic field [38]. Boyer's result [18] suggests that the Casimir interaction can strongly be influenced in artificial microstructures. A generally more undesired effect in MEMS which has been ascribed to the *attractive* Casimir force is the sticking of mobile components [19]. Chan's group realized experimentally a driven micromechanical anharmonic oscillator the anharmonic behaviour of which is induced by the Casimir force and thus showed the influence of the Casimir interaction even on dynamic features of MEMS [24].

Chan and Garcia also studied experimentally the critical Casimir force caused by thermal order parameter fluctuations in Helium films near the critical point. They performed an experiment which shows the thinning of ^{4}He–films absorbed on a stack of copper electrodes near the super fluid transition [43], see also Refs. [44, 105, 54].

The latter experiments make explicit that a potential area of application of Casimir interactions lay in micro– and nanotechnological applications as MEMS and NEMS. Primarily, it would be interesting if surface geometries can be designed in a way to avoid the sticking of mobile parts. Related to this is the question if repulsive forces can appear between *disconnected* surface components [74]. There is still an amount of theoretical work to be done to answer this question. It can be expected that a combination of normal and lateral Casimir forces by a suitable design of surface profiles can be used to construct ratchet–like machines which can rectify fluctuations using the Casimir force.

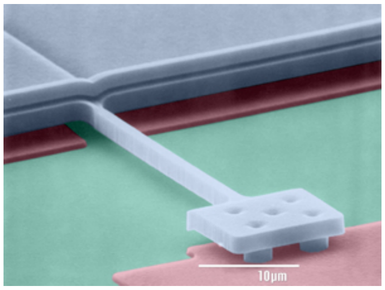

Figure A.8: Micromecanical Oscillator [24].

B Casimir interaction between dielectric materials

The aim of this chapter is to develop an approach for the calculation of molecular interactions between macroscopic surfaces of general shape. The approach is based on the path integral quantization of the fluctuating electromagnetic field A^{μ}. In the free vacuum space, the field quantization is described by the vacuum partition function

$$\mathcal{Z} = \int \mathscr{D}[A]\, e^{iS\{A\}}, \tag{B0.1}$$

which is governed by the Gaussian action $S\{A\}$. Here and in the following, we choose unities such that $\hbar = 1$ and $c = 1$.

The path integral quantization had been applied to calculate fluctuation induced interactions for ideal metals at zero temperature, cf. Refs. [15, 13, 16, 48, 60, 35, 72]. Whereas ideal metals can be described by local boundary conditions for the field components, this is no longer possible for real materials. We will use non–local boundary conditions to describe the interaction of the fluctuating field with the material boundaries. The viewpoint of describing the interaction by field fluctuations in the vacuum with boundary conditions differs from the more elaborated approach of considering the field fluctuations outside and *inside* of the materials [73, 31, 32].

These non–local boundary conditions for the gauge field A^{μ} are based on the extinction theorem of classical electrodynamics, see Refs. [41, 94, 17]. The guiding idea behind this theorem is that an incident field (in the vacuum) induces dipole flutuations in the material. The field of the dipole fluctuations propagates inside the material and a part of it *extinguishes* the incoming field. For this reason the theorem is called "extinction"–theorem. Macroscopically, this extinction can be viewed as caused *at the surface* of the material, see e.g. Ref. [78]. Thus, the theorem establishes a relation between field fluctuations outside and inside of a material via boundary conditions for the quantized field modes, which can be viewed as non–penetrable.

The boundary conditions allow to consider material properties, described by the frequency dependent dielectric function $\epsilon(\omega)$, and geometric deformations *simultaneously*, i.e. no assumptions are made about the correlations between contributions to the force from geometry and material.

An effective Gaussian action is obtained from a path integral quantization. This action is a functional of the dielectric function and the profile function which determines the geometry of the surface, and it serves as a basis for further analytical (e.g. perturbative) or numerical computations to study correlations between material properties and geometry. Thermal fluctuations at finite temperatures are included straightforwardly within this description.

The formalism will be tested by studying first the limit of flat surfaces. This yields the results found by Lifshitz [73] for the interaction of two flat surfaces of real materials in a concise way and without the need to solve Maxwell's equations in separated regions and to considering stress tensor calculations, as done originally by Lifshitz. The Lifshitz theory can also be derived within a scalar field approach. Although this works strictly only for flat surfaces, it is very compact and can be compared with other approaches [107, 70]. Secondly, we consider the action in the limit of ideal metals, where it can be calculated explicitly. A perturbative analysis for this action had been performed in [35, 36] as well as in [34]. An analytic and numeric analysis of this limit will be performed for periodic geometries in later chapters.

1 General approach for material boundaries

We will develop a macroscopic theory which allows to calculate the interaction between materials of rather general shape. Instead of considering directly the field emitted by the fluctuating dipoles in the material, we consider the interaction as generated by the modifications of the quantum (and thermal) fluctuations of the electromagnetic field *between* the materials. No direct reference is made to the electromagnetic field fluctuations in the interior of the materials. The effect of the dipoles induced by the external fluctuating field will be described by material dependent boundary conditions which are defined at the surface of the material. Our method is based on a path integral quantization of the electromagnetic gauge field which has been applied before to ideal metals [15, 13, 48] and penetrable mirrors [16]. This approach has full generality in the sense that it can be applied to any body, characterized by its dielectric function, with any surface profile, described by a height field, at any temperature.

The common approaches for computing the force between materials is to first determine the solution of Maxwell's equations both inside and outside the materials, and then to evaluate the force either from the stress tensor or from the zero point energy of the modes using the so–called argument theorem of complex analysis, see, e.g. Ref. [78]. The problem with these

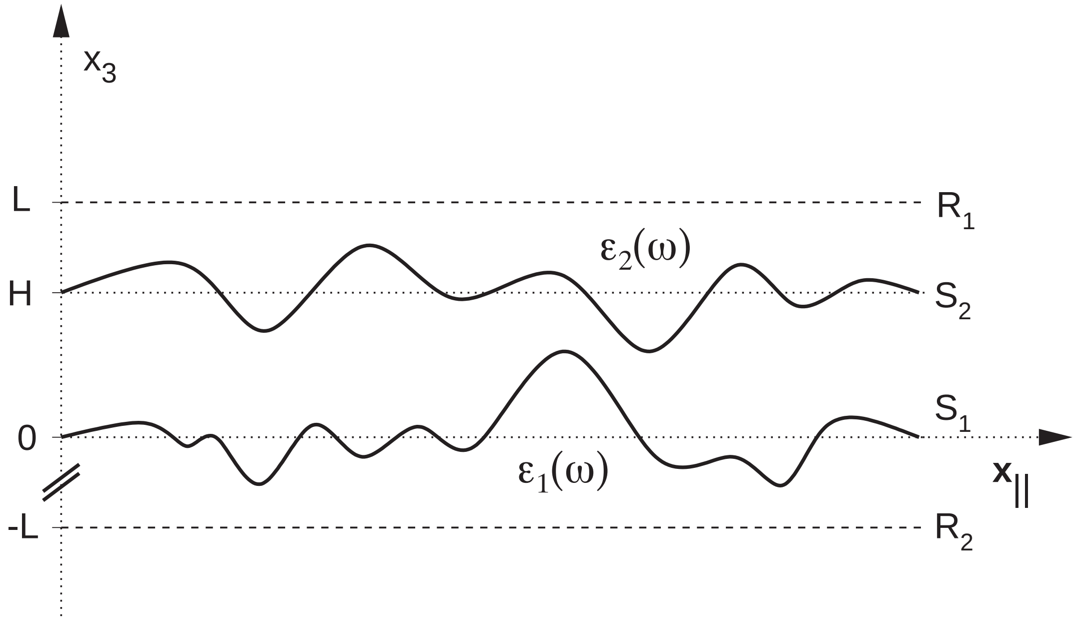

Figure B.1: Two deformed surfaces S_1 and S_2 of dielectric media with dielectric functions $\epsilon_1(\omega)$ and $\epsilon_2(\omega)$, respectively, separated by a gap of mean distance H along the x_3–direction. The meaning of the auxiliary surfaces R_1 and R_2 is explained in the text.

approaches is that they are not suited to treat arbitrary deformations since deformations in general lead to a complicated modification of the mode structure and make the solution of Maxwell's equations a hard task. In the following, we will formulate the interaction between deformed materials within the language of quantum statistical mechanics. Since this formulation makes no explicit use of of the individual eigenfrequencies of the modes it is better targeted for the treatment of deformations.

We consider the two interacting media as filling half spaces which are bounded by deformed surfaces $S_\alpha, \alpha = 1, 2$. The deformations from a coplanar geometry of mean surface distance H are described by the height functions $h_\alpha(\mathbf{x}_{\|})$ with $\mathbf{x}_{\|}$ the lateral surface coordinates, see Fig.B.1. The media are characterized by their complex dielectric functions $\epsilon_\alpha(\omega)$, respectively. The gap between the media is assumed to be vacuum, i.e. $\epsilon(\omega) = 1$.

The free energy $\mathcal{E}$ of the photon gas in the gap between the two surfaces can be calculated from the imaginary time path integral for the electromagnetic gauge field A^μ. In the absence of media, the vacuum partition function $\mathcal{Z}_0$ is given by

$$\mathcal{Z}_0^2 = \int \mathscr{D}[A^* A]\, e^{-S_{\mathsf{E}}\{A^*,A\}}, \tag{B1.2}$$

where we have introduced a complex valued gauge field which leads to a double counting of each degree of freedom. The reason for this will become clear below when we discuss the boundary conditions at the surfaces. Here, the functional integration runs over all fields which are defined on the whole space–time. The Euclidean action $S_{\mathsf{E}}\{A^*, A\}$ is the imaginary time version of the action $S\{A^*, A\}$ of the electromagnetic field in Minkowskian space–time with coordinates $X = (t, \mathbf{x}) = (t, \mathbf{x}_\parallel, x_3)$,

$$S\{A^*, A\} \;=\; -\frac{1}{2}\int_X \left(F^*_{\mu\nu}F^{\mu\nu}\right)(X) - \frac{1}{\xi}\int_X \left(\partial_\mu A^{*\mu}\right)\left(\partial_\nu A^{*\nu}\right)(X), \tag{B1.3}$$

where the first term comes from the Lagrangian of the electromagnetic field $F^{\mu\nu} = \partial^\mu A^\nu - \partial^\nu A^\mu$ and the second term results from the Faddeev–Popov gauge fixing procedure which assures that each physical field configuration is counted only once in the path integral over the gauge field. The parameter ξ allows to switch between different gauges; all gauge invariant quantities calculated from this action like, e.g., the Casimir force, are independent of ξ. In the following, we will use the Feynman gauge corresponding to $\xi = 1$. The coefficients in the action of Eq. (B1.3) differ by a factor of $1/2$ from the conventional definition of the action for a real valued gauge field in order to obtain the correct photon propagator which in Feynman gauge reads $\mathcal{G}_{\mu\nu} = g_{\mu\nu}/K^2$ with momentum $K = (\omega, \mathbf{k}), K^2 = K_\mu K^\mu = \omega^2 - \mathbf{k}^2$ and Minkowskian metric tensor $g_{\mu\nu} = \mathrm{diag}(1, -1, -1, -1)$. The Euclidean action is obtained from Eq. (B1.3) by applying a Wick rotation to imaginary time which amounts to the transformations $t \to -i\tau$, $\omega \to i\zeta$ and $A^0 \to iA^0$, $A^{*0} \to iA^{*0}$ while the remaining components remain unchanged [108, 109]. Since this transformation corresponds to the change $g_{\mu\nu} \to -\delta_{\mu\nu}$ for the metric tensor, the Euclidean action in momentum space becomes

$$S_{\mathsf{E}}\{A^*, A\} \;=\; \frac{1}{\beta}\sum_{n=-\infty}^{\infty}\int_{\mathbf{k}} A^{*\mu}(\zeta_n, \mathbf{k})\, \mathcal{G}^{-1}_{\mathsf{E},\mu\nu}(\zeta_n, \mathbf{k})\, A^\nu(\zeta_n, \mathbf{k}) \tag{B1.4}$$

where we allowed for a finite temperature T by introducing bosonic Matsubara frequencies $\zeta_n = 2\pi n/\beta$ with $\beta = 1/T$. The Euclidean Green function is given by $\mathcal{G}_{\mathsf{E},\mu\nu}(\zeta, \mathbf{k}) = \delta_{\mu\nu}\mathcal{G}_{\mathsf{E}}(\zeta, \mathbf{k})$ with $\mathcal{G}_{\mathsf{E}}(\zeta, \mathbf{k}) = (\zeta^2 + \mathbf{k}^2)^{-1}$. Note that here and in the following, integrals over momenta are always weighted with the factor $(2\pi)^{-n}$, where n is the dimension of the integral.

In the presence of the two media of mean surface separation H the free energy (H–dependent finite part of the total energy) is obtained from a restricted partition function. The restrictions are due to boundary conditions for the gauge field which are imposed by the dielectric properties of the media. It should be mentioned that there is an alternative, microscopic treatment of the Casimir force by considering the coupled system of fluctuating charges in the neutral materials and the gauge field. In the latter description, the Casimir interaction is mediated by the exchange of virtual photons. However, in our macroscopic formulation below we will look at the Casimir force as resulting from the perturbation of normal photon modes as opposed to the exchange of virtual quanta populating the unperturbed modes of the coupled system in unbounded space. Therefore, it is sufficient to derive the boundary conditions from classical electrodynamics which completely determine the normal mode structure in the presence of boundaries.

The restricted partition function will be defined for an auxiliary geometry which consists of three regions which are divided from each other by the infinitely large surfaces S_1 and S_2 which are assumed to be infinitesimally thin. All three regions are assumed to be vacuum space with the same velocity of light. As for the unrestricted partition function, the functional integral extends again over all gauge fields defined on the entire space–time. Below, we will show that the auxiliary geometry "simulates" exactly the original geometry of two half spaces filled with dielectric materials (see Fig.B.1) when appropriate material dependent boundary conditions are defined on the infinitesimally thin surfaces S_1 and S_2. It turns out that there are three boundary conditions on each surface S_α which we number by $j = 1, 2, 3$. Each of these conditions implies the vanishing of a *non–local* linear combination of derivatives of the components of the gauge field. Since the boundary conditions will be non–penetrable, the two infinitesimally thin surfaces separate three regions with independent spectral problems. One can imagine that the two half spaces are replaced by regions which are also bounded by two infinitely large surfaces at $x_3 \to +\infty$ and $x_3 \to -\infty$ on which one imposes the same boundary conditions as on S_1 and S_2, respectively. Depending on the region the observer is located in, the boundary conditions "simulate" a dielectric medium which occupies the entire space behind the surface. Thus, the restricted partition functions formally yield the sum of the energies of three similar spectral problems which differ only by the mean surface distance. The latter distance is sent to infinity for the two outer regions which implies the vanishing of the corresponding Casimir energies. Thus, in this limit, which is always understood in the following, the restricted partition function yields exactly the finite H–dependent Casimir energy of the original geometry of Fig. B.1 The restricted partition function $\mathcal{Z}(H)$ can be written as

$$\mathcal{Z}(H)^2 = \mathcal{Z}_0^{-2} \int \mathscr{D}[A^*A] \prod_{\alpha j} \prod_{\zeta_n} \prod_{\mathbf{x}\in R_\alpha} \delta \left[\int_{\mathbf{x}'\in S_\alpha} \mathcal{L}^{\alpha}_{j\mu}(\zeta_n; \mathbf{x}, \mathbf{x}') A^{\mu}(\zeta_n, \mathbf{x}') \right] e^{-S_{\mathsf{E}}\{A^*, A\}}, \tag{B1.5}$$

where we enforced the boundary conditions by inserting delta functions for all positions $\mathbf{x}$ on (flat) auxiliary surfaces R_α which are placed at $x_3 = \pm L$ with sufficiently large L so that the surfaces S_α are located between them, see Fig. B.1 The final result for the force between the media should (and will) be independent of L. The differential operators $\mathcal{L}^\alpha_{j\mu}$ depend via both the dielectric function ϵ_α and the normal vector $\hat{\mathbf{n}}_\alpha$ on the surface index α. Their actual form will be computed below. The interaction (Casimir) free energy of the two surfaces S_α is given by

$$\mathcal{E}(H) = -\frac{1}{\beta} \ln \left[\mathcal{Z}(H) \mathcal{Z}_\infty^{-1}(H) \right] , \tag{B1.6}$$

where $\beta = 1/T$ is the inverse temperature. $\mathcal{Z}_\infty$ is the asymptotic limit of $\mathcal{Z}$ for $H \to \infty$ so that $\mathcal{E}$ is measured relative to two surfaces which are infinitely apart from each other. The Casimir force per unit area A between the surfaces is then given by $F/A = -\partial_H \mathcal{E}/A$.

1.1 Boundary conditions

In this section, we will derive the boundary conditions at the surfaces of the dielectric media. The boundary conditions are based on the optical extinction theorem of Ewald [41] and Oseen [94], see also [17]. This theorem states that part of the electromagnetic field produced by the molecular dipoles inside a medium exactly cancels the incident field, while the remainder propagates according to Maxwell's equations in continuous media. Ewald and Oseen proved the theorem for crystalline media and amorphous, isotropic dielectrics, respectively, using an approach based on classical molecular optics. Later, Born and Wolf extended the theorem to more general classes of materials [17]. A relationship between the extinction theorem and the Lifshitz theory of dispersion forces for continuous media has been pointed out by Milonni and Lerner [79]. They use the fact that the extinction theorem permits a reduction of the multiple scattering problem for the molecular dipoles to the solution of the wave equation for the gauge field A^μ with appropriate boundary conditions. From this they conclude that the extinction theorem shows that the macroscopic Lifshitz theory for continuous media correctly accounts for all multiple scattering *non–additive* contributions to the force between flat surfaces. We will demonstrate that these concepts are useful to describe the interaction of even deformed surfaces.

We will use an (equivalent) reformulation of the extinction theorem as a non–local boundary condition which enforces the laws of reflection and refraction at the surfaces of the interacting media. Our derivation of the boundary conditions follows closely the approach outlined in [75]. We start with the common problem of finding solutions of Maxwell's equations in the presence of a single interface separating two half spaces of materials with different dielectric functions. We assume that one half space is filled with a dielectric material described by $\epsilon(\omega)$

whereas the other half space is vacuum. The standard approach to this problem is to solve *simultaneously* the Maxwell equations in both half spaces by connecting them at the interface. The corresponding matching conditions state that (in the absence of surface charges and currents) the magnetic field $\mathbf{B}$ and the tangential components of $\mathbf{E}$ are continuous while the normal component of $\mathbf{E}$ jumps across the interface such that the normal component of $\mathbf{D} = \epsilon(\omega)\mathbf{E}$ is continuous. We assumed that the magnetic permeability is equal in both half spaces.

In what follows we are interested in the spectral properties of the electromagnetic field in the vacuum gap between two surfaces. Thus, it suffices to know the field on one side of the interface only. Therefore, we would like to find a more efficient way to solve the matching problem. We will show below that it is in fact possible to obtain the solution in one half space by solving the appropriate Maxwell equations in this region *only* subject to boundary conditions which contain all necessary information about the material behind the surface. We assume the observer to be in the vacuum gap and solve the equations *there* which are then subject to *material dependent* boundary conditions. Note that the latter point of view is a standard concept for ideal metals where the matching conditions are trivially fulfilled by vanishing tangential components of the electric field. Thus, the boundary conditions considered here can be interpreted as a generalization of the latter concept to dielectric media.

In order to obtain the boundary conditions, we first derive a general statement on a vector field (here the magnetic field $\mathbf{B}$) which is assumed to be a solution of the Helmholtz wave equation inside a volume V occupied by a medium with dielectric function $\epsilon(\omega)$ and with boundary surface $S = \partial V$,

$$\left(\nabla^2 + \epsilon(\omega)\omega^2\right)\mathbf{B}(\omega, \mathbf{x}) = 0. \tag{B1.7}$$

Here, $\mathbf{B}$ can be subjected to a boundary condition on S which, however, remains unspecified for the time being. In addition to that, we define the standard *free* Green function $\mathcal{G}^\epsilon$, which is defined on the unbounded space–time which, however, is assumed to be filled with a dielectric medium described by $\epsilon(\omega)$. It satisfies

$$\left(\nabla'^2 + \epsilon(\omega)\omega^2\right)\mathcal{G}^\epsilon(\omega; \mathbf{x}, \mathbf{x}') = \delta^{(3)}(\mathbf{x} - \mathbf{x}'). \tag{B1.8}$$

Applying Green's theorem to the components of $\mathbf{B}$ and to $\mathcal{G}^\epsilon$, one easily obtains, using Eqs. (B1.7) and (B1.8),

$$\begin{aligned}&\int_{\mathbf{x}' \in S} \left[\mathbf{B}(\omega, \mathbf{x})\left(\hat{\mathbf{n}}' \cdot \nabla' \mathcal{G}^\epsilon(\omega; \mathbf{x}, \mathbf{x}')\right) - \mathcal{G}^\epsilon(\omega; \mathbf{x}, \mathbf{x}')\left(\hat{\mathbf{n}}' \cdot \nabla'\right)\mathbf{B}(\omega, \mathbf{x})\right] \\ &\qquad = \begin{cases} \mathbf{B}(\omega, \mathbf{x}) & \text{if} \quad \mathbf{x} \in V, \\ 0 & \text{if} \quad \mathbf{x} \notin V, \end{cases}\end{aligned} \tag{B1.9}$$

with the normal unit vector $\hat{\mathbf{n}}' = \hat{\mathbf{n}}(\mathbf{x}')$ of the surface pointing to the outside of V. It is important to remark that Eq. (B1.9) does not imply that the actual magnetic field of the matching problem vanishes outside V. Instead, the magnetic field on the vacuum side is not obtainable by matching or boundary conditions. Eq. (B1.9) does not provide a solution for the boundary value problem. It is only an integral statement since the specification of arbitrary values of $\mathbf{B}$ and $(\hat{\mathbf{n}} \cdot \nabla)\,\mathbf{B}$ at the interface would be an overspecification of the boundary value problem. The result of Eq. (B1.9) will be used for the case that the position $\mathbf{x}$ is located outside the medium so that the integral has to vanish. Using some vector algebra, see [57], and the Maxwell equations $\nabla \cdot \mathbf{B} = 0$ and $\nabla \times \mathbf{B} = -i\omega\epsilon(\omega)\mathbf{E}$, the integral of Eq. (B1.9) can be transformed into

$$\begin{aligned}\int_{\mathbf{x}'\in S} \big[-i\omega\epsilon(\omega)\, \big(\hat{\mathbf{n}}' \times \mathbf{E}(\omega, \mathbf{x}')\big) + \big(\hat{\mathbf{n}}' \cdot \mathbf{B}(\omega, \mathbf{x}')\big)\, \nabla' \\ + \big(\hat{\mathbf{n}}' \times \mathbf{B}(\omega, \mathbf{x}')\big) \times \nabla' \,\big]\, \mathcal{G}^{\epsilon}(\omega; \mathbf{x}, \mathbf{x}') \;=\; 0.\end{aligned} \tag{B1.10}$$

The latter integral provides a relation between the field components if the surface is approached from the inside of the dielectric space. The terms in Eq. (B1.10) are all continuous across the surface. This can bee seen from the continuity conditions on the electromagnetic field mentioned above (note that $\hat{\mathbf{n}} \cdot \mathbf{E}$ does not appear in Eq. (B1.10)), and the fact that the Green function $\mathcal{G}^{\epsilon}$ and dielectric function $\epsilon(\omega)$ are continuous at the surface. (The function $\epsilon(\omega)$ is here spatially constant and should not be confused with the spatially varying ϵ in Fig. B.1.)

As a consequence, we can now use the vanishing of the integral as a boundary condition for the electromagnetic field on the *vacuum side* of the surface. As a side remark, we note that if we had started with the wave equation for the electric field instead of the magnetic field we had obtained a similar expression as Eq. (B1.10) containing, however, the normal component of $\mathbf{E}$. Due to the discontinuity of the normal component of the electric field across the surface, the condition that the integral vanishes had not translated to the field on the vacuum side. In the case of ideal conductivity, $\epsilon(\omega) \to \infty$, and the integral in Eq. (B1.10) will be dominated by the first term. In this limit, the integration can be carried out, leading to the local condition $\hat{\mathbf{n}} \times \mathbf{E} = 0$.

The condition of Eq. (B1.10) can now be used to determine the differential operators $\mathcal{L}^{\alpha}_{j\mu}(\zeta; \mathbf{x}, \mathbf{x}')$ appearing in Eq. (B1.5). We express the electric and magnetic field in terms of the gauge field. After a Wick rotation to imaginary time, the corresponding relations read $E_j = -i\partial_j A^0 - \zeta A^j$ and $B_j = \varepsilon_{jkl}\partial_k A^l$ in Euclidean space. Multiplying Eq. (B1.10) with $(\zeta\epsilon_\alpha)^{-1}$ and decomposing $\mathcal{L}^{\alpha}_{j\mu}(\zeta; \mathbf{x}, \mathbf{x}') = \hat{\mathbf{n}}^{\alpha}_{k}(\mathbf{x}')\mathscr{L}^{k\alpha}_{j\mu}(\zeta)\mathcal{G}^{\epsilon_\alpha}_{\mathsf{E}}(\zeta; \mathbf{x} - \mathbf{x}')$ with respect to the components $\hat{\mathbf{n}}^{\alpha}_{k}$ of the normal vector to the surface using the standard summation convention for k, and with respect to the action on the material dependent Euclidean Green function $\mathcal{G}_{\mathsf{E}}^{\epsilon_\alpha}$ defined by Eq. (B1.8), one gets after some algebra the explicit results

$$\mathscr{L}^{1\alpha}(\zeta) = \begin{pmatrix} 0 & -\frac{1}{\zeta\epsilon_\alpha}(\bar{\partial}_3\partial_2-\bar{\partial}_2\partial_3) & \frac{1}{\zeta\epsilon_\alpha}(\bar{\partial}_1\partial_3+\bar{\partial}_3\partial_1) & -\frac{1}{\zeta\epsilon_\alpha}(\bar{\partial}_1\partial_2+\bar{\partial}_2\partial_1) \\ i\partial_3 & -\frac{1}{\zeta\epsilon_\alpha}\bar{\partial}_1\partial_3 & \frac{1}{\zeta\epsilon_\alpha}\bar{\partial}_2\partial_3 & \zeta-\frac{1}{\zeta\epsilon_\alpha}(\bar{\partial}_2\partial_2-\bar{\partial}_1\partial_1) \\ -i\partial_2 & \frac{1}{\zeta\epsilon_\alpha}\bar{\partial}_1\partial_2 & -\zeta+\frac{1}{\zeta\epsilon_\alpha}(\bar{\partial}_3\partial_3-\bar{\partial}_1\partial_1) & -\frac{1}{\zeta\epsilon_\alpha}\bar{\partial}_3\partial_2 \end{pmatrix}, \quad \text{(B1.11)}$$

$$\mathscr{L}^{2\alpha}(\zeta) = \begin{pmatrix} -i\partial_3 & -\frac{1}{\zeta\epsilon_\alpha}\bar{\partial}_1\partial_3 & \frac{1}{\zeta\epsilon_\alpha}\bar{\partial}_2\partial_3 & -\zeta+\frac{1}{\zeta\epsilon_\alpha}(\bar{\partial}_1\partial_1-\bar{\partial}_2\partial_2) \\ 0 & -\frac{1}{\zeta\epsilon_\alpha}(\bar{\partial}_2\partial_3+\bar{\partial}_3\partial_2) & -\frac{1}{\zeta\epsilon_\alpha}(\bar{\partial}_1\partial_3-\bar{\partial}_3\partial_1) & \frac{1}{\zeta\epsilon_\alpha}(\bar{\partial}_2\partial_1+\bar{\partial}_1\partial_2) \\ i\partial_1 & \zeta-\frac{1}{\zeta\epsilon_\alpha}(\bar{\partial}_3\partial_3-\bar{\partial}_2\partial_2) & -\frac{1}{\zeta\epsilon_\alpha}\bar{\partial}_2\partial_1 & \frac{1}{\zeta\epsilon_\alpha}\bar{\partial}_3\partial_1 \end{pmatrix}, \quad \text{(B1.12)}$$

$$\mathscr{L}^{3\alpha}(\zeta) = \begin{pmatrix} i\partial_2 & \frac{1}{\zeta\epsilon_\alpha}\bar{\partial}_1\partial_2 & \zeta-\frac{1}{\zeta\epsilon_\alpha}(\bar{\partial}_1\partial_1-\bar{\partial}_3\partial_3) & -\frac{1}{\zeta\epsilon_\alpha}\bar{\partial}_3\partial_2 \\ -i\partial_1 & -\zeta+\frac{1}{\zeta\epsilon_\alpha}(\bar{\partial}_2\partial_2-\bar{\partial}_3\partial_3) & -\frac{1}{\zeta\epsilon_\alpha}\bar{\partial}_2\partial_1 & \frac{1}{\zeta\epsilon_\alpha}\bar{\partial}_3\partial_1 \\ 0 & \frac{1}{\zeta\epsilon_\alpha}(\bar{\partial}_3\partial_2+\bar{\partial}_2\partial_3) & -\frac{1}{\zeta\epsilon_\alpha}(\bar{\partial}_3\partial_1+\bar{\partial}_1\partial_3) & -\frac{1}{\zeta\epsilon_\alpha}(\bar{\partial}_2\partial_1-\bar{\partial}_1\partial_2) \end{pmatrix}. \quad \text{(B1.13)}$$

The partial differential operators $\bar{\partial}_j$ are acting on the spatial argument of $\mathcal{G}_{\mathsf{E}}^{\epsilon_\alpha}$, whereas the "free" operators ∂_j are acting on the gauge field to which $\mathcal{L}^{\alpha}_{j\mu}$ is applied. For non–deformed surfaces as considered in the conventional Lifshitz theory, i.e., $\hat{\mathbf{n}} = (0, 0, \pm 1)$, only the last matrix is relevant.

1.2 General result for deformed surfaces

Now we are in the position to calculate the partition function defined by Eq. (B1.5) and by the operators in Eqs. (B1.11)–(B1.13). Similar to the approach of Refs. [72, 48], we introduce auxiliary fields to treat the delta function constraints. However, here we will use complex valued auxiliary fields since the arguments of the delta functions are complex in our problem. Moreover, the fields will not be defined on the original surfaces S_α itself but on the flat auxiliary surfaces R_α since these are the regions on which the "external" positions $\mathbf{x}$ of the boundary conditions are located, cf. Eq. (B1.5). Introducing on each of the two surfaces R_α at $x_3 = L_\alpha = (-1)^{\alpha-1}L$ with lateral coordinates $\mathbf{x}_\|$ the three fields $\psi_{\alpha j}(\zeta, \mathbf{x}_\|)$ for $j = 1, 2, 3$, the delta functions for fixed α and j can be written as

$$\begin{aligned} &\prod_{\zeta_n} \prod_{\mathbf{x}\in R_\alpha} \delta\left[\int_{\mathbf{x}'\in S_\alpha} \mathcal{L}^{\alpha}_{j\mu}(\zeta_n; \mathbf{x}, \mathbf{x}') A^\mu(\zeta_n, \mathbf{x}')\right] \\ &\quad = \int \mathscr{D}[\psi^*_{\alpha j}\psi_{\alpha j}]\, e^{i\sum_n \int_{\mathbf{x}_\|} \int_{\mathbf{x}'\in S_\alpha} \left\{\psi^*_{\alpha j}(\zeta_n, \mathbf{x}_\|)\mathcal{L}^{\alpha}_{j\mu}\left(\zeta_n; (\mathbf{x}_\|, L_\alpha), \mathbf{x}'\right) A^\mu(\zeta_n, \mathbf{x}') + \text{c.c.}\right\}}. \end{aligned} \quad \text{(B1.14)}$$

Inserting this representation into the partition function of Eq. (B1.5), the complex gauge field A^μ can be integrated out, using the free action $S_{\mathsf{E}}\{A^*, A\}$ of Eq. (B1.4). The partition function can then be expressed in terms of an effective quadratic action for the auxiliary fields,

$$\mathcal{Z}^2(H) = \int \prod_{\alpha j} \mathscr{D}\left[\psi^*_{\alpha j}\psi_{\alpha j}\right]\, e^{-S_{\mathsf{eff}}\{\psi^*_{\alpha j}, \psi_{\alpha j}\}} \quad \text{(B1.15)}$$

with

$$S_{\mathsf{eff}}\left\{\psi^*_{\alpha j}, \psi_{\alpha j}\right\} = \sum_{n,n'} \int_{\mathbf{x}_\parallel} \int_{\mathbf{x}'_\parallel} \psi^*_{\alpha j}\big(\zeta_n, \mathbf{x}_\parallel\big) \mathcal{M}^{\alpha\beta,jl}\big(\zeta_n, \mathbf{x}_\parallel; \zeta_{n'}, \mathbf{x}'_\parallel\big) \psi_{\beta l}\big(\zeta_{n'}, \mathbf{x}'_\parallel\big), \tag{B1.16}$$

where the standard summation convention applies to all indices. Since in Feynman gauge the propagator of A^μ is diagonal in μ, the resulting matrix kernel can be written as

$$\begin{aligned} \mathcal{M}^{\alpha\beta,jl}\big(\zeta, \mathbf{x}_\parallel; \zeta', \mathbf{x}'_\parallel\big) &= 2\pi\delta\big(\zeta - \zeta'\big) \\ \times \int_{\mathbf{y}\in S_\alpha} \int_{\mathbf{y}'\in S_\beta} & \mathcal{L}^\alpha_{j\mu}\big(\zeta; (\mathbf{x}_\parallel, L_\alpha), \mathbf{y}\big) \mathcal{L}^{\dagger\beta}_{\mu l}\big(\zeta'; (\mathbf{x}'_\parallel, L_\beta), \mathbf{y}'\big) \mathcal{G}_{\mathsf{E}}\big(\zeta; \mathbf{y} - \mathbf{y}'\big), \end{aligned} \tag{B1.17}$$

where a summation over μ is implicit and $\mathcal{G}_{\mathsf{E}}(\zeta, \mathbf{y})$ is the free Euclidean photon propagator with Fourier transform $\mathcal{G}_{\mathsf{E}}(\zeta; \mathbf{k}) = (\zeta^2 + \mathbf{k}^2)^{-1}$. This matrix kernel is defined on the surfaces R_α like the auxiliary fields $\psi_{\alpha j}$ are. To simplify this result and to prove the independence of the free energy on the choice of L, it is useful to rewrite Eq. (B1.17) in terms of the differential operators $\mathscr{L}^{k\alpha}$ by $\mathcal{L}^\alpha_{j\mu}(\zeta; \mathbf{x}, \mathbf{x}') = \hat{\mathbf{n}}^\alpha_k(\mathbf{x}') \mathscr{L}^{k\alpha}_{j\mu}(\zeta) \mathcal{G}^{\epsilon_\alpha}_{\mathsf{E}}(\zeta; \mathbf{x} - \mathbf{x}')$ in order to make explicit the dependence of the material Green functions. It is important to keep in mind that the differential operators act on the spatial arguments of $\mathcal{G}^{\epsilon_\alpha}_{\mathsf{E}}$ as well as on those of the free propagator $\mathcal{G}_{\mathsf{E}}$. Now the kernel in Eq. (B1.17) acquires the form

$$\begin{aligned} \mathcal{M}^{\alpha\beta,jl}\big(\zeta, \mathbf{x}_\parallel; \zeta', \mathbf{x}'_\parallel\big) \; &= \; 2\pi\delta\big(\zeta - \zeta'\big) \int_{\mathbf{y}\in S_\alpha} \int_{\mathbf{y}'\in S_\beta} \hat{\mathbf{n}}^\alpha_k \hat{\mathbf{n}}'^\beta_s \big[\mathscr{L}^{k\alpha} \cdot \mathscr{L}'^{\dagger s\beta}\big]_{jl} \\ &\times \; \mathcal{G}^{\epsilon_\alpha}_{\mathsf{E}}\big(\zeta; \mathbf{x} - \mathbf{y}\big) \,|_{x_3 = L_\alpha} \; \mathcal{G}^{*\epsilon_\beta}_{\mathsf{E}}\big(\zeta'; \mathbf{x}' - \mathbf{y}'\big) \Big|_{x'_3 = L_\beta} \; \mathcal{G}_{\mathsf{E}}\big(\zeta; \mathbf{y} - \mathbf{y}'\big), \end{aligned} \tag{B1.18}$$

where $\mathscr{L}'^{k\alpha}$ acts on the primed coordinates and a summation over k and s is implicit. In the following, we will skip the index at $\mathcal{G}_{\mathsf{E}}$ since we work completely in Euclidean space.

Note that the integral measure on the manifolds S_α contains the square root of the induced surface metric $g_\alpha = \det(g_{\alpha,ij})$ with the Riemannian metric tensor

$$g_{\alpha,ij} \;=\; \delta_{\mu\nu} \frac{\partial X^\mu_\alpha}{\partial x^i} \frac{\partial X^\nu_\alpha}{\partial x^j} \tag{B1.19}$$

with summation over the indices $\mu, \nu = 0, 1, 2, 3$. The vectors X_α parametrize the manifolds S_α in 4D Euclidean space–time by the 3D vectors $\mathbf{x}$. Using the parametrization in terms of (static) height profiles over a base plane in the geometry considered here, $X_\alpha(t, \mathbf{x}_\parallel) = \big(t, \mathbf{x}_\parallel, h_\alpha(\mathbf{x}_\parallel)\big)$ which leads to $g_\alpha = 1 + \big(\nabla_\parallel h_\alpha\big)^2$. The integrals in Eqs. (B1.17)–(B1.18) are thus given by $\int_{\mathbf{x}\in S_\alpha} = \int_{\mathbf{x}_\parallel} \sqrt{g_\alpha}$. The surface normal vectors $\hat{\mathbf{n}}_\alpha$ assume the form

$$\hat{\mathbf{n}}_\alpha = \frac{(-1)^\alpha}{\sqrt{g_\alpha}} \begin{pmatrix} h_{\alpha,1} \\ h_{\alpha,2} \\ -1 \end{pmatrix} \tag{B1.20}$$

with $h_{\alpha,j} = \partial_j h_\alpha$ and $g_\alpha = 1 + \left(\nabla_\| h_\alpha\right)^2$. Thus, the factor $\sqrt{g_\alpha}$ will cancel in Eqs. (B1.17)–(B1.18). This property will be used in explicit calculations for flat and for ideally conducting boundaries in the forthcoming sections.

In momentum space, using $\mathcal{G}^\epsilon(\zeta, \mathbf{k}) = (\epsilon(i\zeta)\zeta^2 + \mathbf{k}^2)^{-1}$, the partially Fourier transformed material Green function can be written as

$$\mathcal{G}^{\epsilon_\alpha}\big(\zeta; \mathbf{k}_\|, z\big) \;=\; \frac{e^{-p_\alpha(\zeta,\mathbf{k}_\|)|z|}}{2p_\alpha(\zeta, \mathbf{k}_\|)} \tag{B1.21}$$

with $p_\alpha(\zeta, \mathbf{k}_\|) = (\epsilon_\alpha(i\zeta)\zeta^2 + \mathbf{k}_\|^2)^{1/2}$. With this representation, the kernel becomes

$$\begin{aligned}\mathcal{M}^{\alpha\beta,jl}\big(\zeta, \mathbf{k}_\|; \zeta', \mathbf{k}'_\|\big) \;=\;& 2\pi\delta\big(\zeta-\zeta'\big)\int_{\mathbf{y}\in S_\alpha}\int_{\mathbf{y}'\in S_\beta} e^{-i\mathbf{k}_\|\cdot\mathbf{y}_\| + i\mathbf{k}'_\|\cdot\mathbf{y}'_\|}\\ &\times\; \frac{e^{-p_\alpha(\zeta,\mathbf{k}_\|)|L_\alpha - y_3|}}{2p_\alpha(\zeta,\mathbf{k}_\|)}\frac{e^{-p_\beta(\zeta',\mathbf{k}'_\|)|L_\beta - y'_3|}}{2p_\beta(\zeta',\mathbf{k}'_\|)}\\ &\times\; \hat{\mathbf{n}}^\alpha_k \hat{\mathbf{n}}'^\beta_s \big[\hat{\mathscr{L}}^{k\alpha}(\zeta,\mathbf{k}_\|)\cdot\hat{\mathscr{L}}'^{\dagger s\beta}(\zeta',\mathbf{k}'_\|)\big]_{jl}\,\mathcal{G}\big(\zeta; \mathbf{y}-\mathbf{y}'\big),\end{aligned} \tag{B1.22}$$

where the differential operators $\hat{\mathscr{L}}^{k\alpha}(\zeta, \mathbf{k}_\|)$ are obtained from the $\mathscr{L}^{k\alpha}$ of Eqs. (B1.11)–(B1.13) by substituting $\bar{\nabla}_\| \equiv (\bar{\partial}_1, \bar{\partial}_2) \to i\mathbf{k}_\|, \bar{\partial}_3 \to (-1)^\alpha p_\alpha$. Thus, the operators $\hat{\mathscr{L}}^{k\alpha}(\zeta, \mathbf{k}_\|)$ are acting via the remaining derivatives ∂_j only on the spatial coordinates of the vacuum Green function $\mathcal{G}(\zeta, \mathbf{k})$. At this stage, it will become obvious that the free energy or force is independent of the positions $x_3 = \pm L$ of the auxiliary surfaces R_α. Due to the construction of the surfaces R_α, we have $|L_\alpha - y_3| = (-1)^{\alpha-1}(L_\alpha - y_3)$. A consequence of this is the observation that the kernel can be factorized into

$$\mathcal{M}^{\alpha\beta,jl}\big(\zeta, \mathbf{k}_\|; \zeta', \mathbf{k}'_\|\big) = \eta_\alpha\big(\zeta, \mathbf{k}_\|\big)\tilde{\mathcal{M}}^{\alpha\beta,jl}\big(\zeta, \mathbf{k}_\|; \zeta', \mathbf{k}'_\|\big)\eta_\beta\big(\zeta', \mathbf{k}'_\|\big) \tag{B1.23}$$

with the functions $\eta_\alpha(\zeta, \mathbf{k}_\|) = \exp\big(-p_\alpha(\zeta, \mathbf{k}_\|)L\big)/2p_\alpha(\zeta, \mathbf{k}_\|)$ and the simplified L–independent kernel

$$\begin{aligned}\tilde{\mathcal{M}}^{\alpha\beta,jl}\big(\zeta, \mathbf{k}_\|; \zeta', \mathbf{k}'_\|\big) \;=\;& 2\pi\delta\big(\zeta-\zeta'\big)\int_{\mathbf{y}\in S_\alpha}\int_{\mathbf{y}'\in S_\beta} e^{-i\mathbf{k}_\|\cdot\mathbf{y}_\| + i\mathbf{k}'_\|\cdot\mathbf{y}'_\|}\\ &\times\; e^{-(-1)^\alpha p_\alpha(\zeta,\mathbf{k}_\|)y_3 - (-1)^\beta p_\beta(\zeta',\mathbf{k}'_\|)y'_3}\\ &\times\; \hat{\mathbf{n}}^\alpha_k \hat{\mathbf{n}}'^\beta_s \big[\hat{\mathscr{L}}^{k\alpha}(\zeta,\mathbf{k}_\|)\cdot\hat{\mathscr{L}}'^{\dagger s\beta}(\zeta',\mathbf{k}'_\|)\big]_{jl}\,\mathcal{G}\big(\zeta; \mathbf{y}-\mathbf{y}'\big).\end{aligned} \tag{B1.24}$$

From Eq. (B1.15) follows that the partition function is $\mathcal{Z}(H) = (\det\mathcal{M})^{-1/2}$ with the determinant taken with respect to both the continuous $(\zeta, \mathbf{k}_\|)$ and the discrete (α, j) arguments. Due to the structure of Eq. (B1.23) one has $\det\mathcal{M} \sim \det\tilde{\mathcal{M}}$. Since the functions $\eta_\alpha(\zeta, \mathbf{k}_\|)$ are independent of the mean surface distance H, the proportionality constant of the two determinants is independent of H, too. Therefore, this constant, as well as the dependence on L will drop out of the free energy of Eq. (B1.6), which can now be written as

$$\mathcal{E}(H) = \frac{1}{2\beta} \ln\det\left(\tilde{\mathcal{M}}\tilde{\mathcal{M}}_\infty^{-1}\right), \tag{B1.25}$$

where $\tilde{\mathcal{M}}_\infty$ denotes $\tilde{\mathcal{M}}$ in the limit of asymptotically large H. The normal force can then be directly obtained by $F = -\partial_H \mathcal{E}$ which yields per surface area

$$F/A = -\frac{1}{2A\beta} \mathrm{Tr}\left(\tilde{\mathcal{M}}^{-1}\partial_H\tilde{\mathcal{M}}\right). \tag{B1.26}$$

In Eq. (B1.26), there is no need to subtract the asymptotic expansion for large H. This is different from the study of lateral forces, as will be seen later. The trace has to be taken with respect to the Matsubara frequencies ζ_n, the lateral momenta $\mathbf{k}_\|$, and the discrete arguments given by the surface index α and the index j which enumerates the boundary condition at each surface. Eqs. (B1.24)–(B1.26) represent the main result of the general approach discussed here; these formulas will be applied later to specific model situations.

Before proceeding, some features of the above results will be discussed. During the derivation of the matrix kernel $\tilde{\mathcal{M}}$ we worked within the Feynman gauge. This is no loss of generality since the restricted partition function $\mathcal{Z}(H)$ can be considered as the expectation value of the boundary condition enforcing delta–functions with respect to the free action of the gauge field. The arguments of the delta functions are composed of the electromagnetic field components, and are thus manifestly gauge invariant, which assures also the gauge invariance of the kernel $\tilde{\mathcal{M}}$.

Firstly, we consider the case where the kernel $\tilde{\mathcal{M}}$ is diagonal in momentum space so that the force can be calculated exactly. This will be the case when the geometry has translational symmetry in the lateral directions, i.e., for flat surfaces for which the height functions vanish, $h_\alpha(\mathbf{x}_\|) = 0$. Then, the integrals in Eq. (B1.24) can be easily computed and the resulting kernel provides a concise account of Lifshitz' theory will be discussed in detail below. Even for deformed surfaces the kernel can be obtained explicitly if one considers the limit of ideal metals, i.e. a diverging dielectric function $\epsilon(i\zeta)$. In this particular limit, both p_α and the operators $\hat{\mathscr{L}}^{k\alpha}$ become independent of the lateral momentum $\mathbf{k}_\|$. Therefore, after parametrizing the surfaces in the way that y_3, y_3' are replaced by functions of the lateral coordinates $\mathbf{y}_\|, \mathbf{y}_\|'$, respectively, the integrals in Eq. (B1.24) correspond to Fourier transformations with respect to the lateral coordinates, and the kernel assumes a simple form in position space as we will demonstrate explicitly. However, any kind of deviation from flat surfaces, even for ideal metals, renders $\tilde{\mathcal{M}}$ non–diagonal and makes the evaluation of Eqs. (B1.25)–(B1.26) a difficult problem. There are basically two approaches to treat this problem. First, one can consider the amplitude of the surface deformations as small compared to both the mean surface distance H and other characteristic lateral length scales as, e.g., the roughness correlation lengths. Then, one can apply perturbation theory to obtain the force in powers of the deformation profiles $h_\alpha(\mathbf{x}_\|)$. This program has been carried out in detail for ideal metals in Refs. [35, 36]. Secondly, one can try to compute the force exactly by numerical algorithms. For periodically deformed (corrugated) surfaces of ideal metals, the corresponding kernel can be transformed into a form which is particularly suited for an efficient numerical evaluation of the force. This will discussed in detail in the next chapter, for a quick reference, see [34]. We expect that these techniques can be applied to the general case of deformed surfaces of dielectric media using the approach derived here of expressing the force in terms of a kernel (Eq. (B1.24)) which contains all information about material and geometrical properties of the surfaces. As for ideal metals, the kernel is proportional to the vacuum Green function which, however, is now dressed by the operators $\hat{\mathscr{L}}^{k\alpha}$ which contain the reflection and refraction properties of the material.

2 Flat surface limit and the Lifshitz theory

As a simple application of our approach, we consider in this chapter the case of flat surfaces of general dielectric media. In this particular limit, the force between the surfaces is well known from more conventional approaches. The corresponding result is known as the so called Lifshitz theory of molecular forces [73]. In the following, we will show that our path–integral approach provides a compact derivation of the Lifshitz result without the need to solve Maxwell's equations with a random source explicitly and to calculate the expectation value of the stress tensor. In the flat surface limit, the surfaces are parametrized by $(\mathbf{y}_\|, H_\alpha)$ with $H_\alpha = 0, H$ for $\alpha = 1, 2$, respectively. Due to the translational symmetry of the problem, it is convenient to work in momentum space. Using the representation

$$\mathcal{G}(\zeta, \mathbf{y}) = \int_{\mathbf{q}_\|} e^{i\mathbf{q}_\| \cdot \mathbf{y}_\|} \frac{e^{-p(\zeta, \mathbf{q}_\|)|y_3|}}{2p(\zeta, \mathbf{q}_\|)} \tag{B2.27}$$

of the vacuum Green function in Eq. (B1.24) with $p(\zeta, \mathbf{q}_\|) = (\zeta^2 + \mathbf{q}_\|^2)^{1/2}$ yields

$$\begin{aligned} \tilde{\mathcal{M}}^{\alpha\beta,jl}(\zeta, \mathbf{k}_\|; \zeta', \mathbf{k}'_\|) \;&=\; 2\pi\delta(\zeta - \zeta') \int_{\mathbf{q}_\|} \int_{\mathbf{y}_\|} \int_{\mathbf{y}'_\|} e^{-i\mathbf{k}_\| \cdot \mathbf{y}_\| + i\mathbf{k}'_\| \cdot \mathbf{y}'_\|} \\ &\times\; e^{-(-1)^\alpha p_\alpha(\zeta, \mathbf{k}_\|) H_\alpha - (-1)^\beta p_\beta(\zeta', \mathbf{k}'_\|) H_\beta} \\ &\times\; (-1)^{\alpha+\beta} \left[\hat{\mathscr{L}}^{3\alpha}(\zeta, \mathbf{k}_\|) \cdot \hat{\mathscr{L}}'^{\dagger 3\beta}(\zeta', \mathbf{k}'_\|)\right]_{jl} e^{i\mathbf{q}_\| \cdot (\mathbf{y}_\| - \mathbf{y}'_\|)} \frac{e^{-p(\zeta, \mathbf{q}_\|)|y_3 - y'_3|}}{2p(\zeta, \mathbf{q}_\|)}, \end{aligned} \tag{B2.28}$$

where we made use of the surface normal vectors $\hat{\mathbf{n}}^\alpha = (0, 0, (-1)^{\alpha-1})$ for flat surfaces. The differential operators $\hat{\mathscr{L}}^{3\alpha}$ and $\hat{\mathscr{L}}'^{\dagger 3\beta}$ can now be expressed in momentum space with the replacements $\nabla_\| \to i\mathbf{k}_\|$ and $\nabla'_\| \to i\mathbf{k}'_\|$ yielding

$$\begin{aligned} \tilde{\mathcal{M}}^{\alpha\beta,jl}\big(\zeta, \mathbf{k}_\|; \zeta', \mathbf{k}'_\|\big) \; &= \; (2\pi)^3 \delta\big(\zeta - \zeta'\big) \delta^{(2)}\big(\mathbf{k}_\| - \mathbf{k}'_\|\big) \\ \times \; \eta_{\alpha\beta} \left[\hat{\mathscr{L}}^{3\alpha}(\zeta, \mathbf{k}_\|) \cdot \hat{\mathscr{L}}'^{\dagger 3\beta}(\zeta', \mathbf{k}'_\|)\right]_{jl} & \frac{e^{-p(\zeta,\mathbf{k}_\|)|y_3 - y'_3|}}{2p(\zeta, \mathbf{k}_\|)} \Bigg|_{\substack{y_3 = H_\alpha \\ y'_3 = H_\beta}} , \end{aligned} \tag{B2.29}$$

where we separated the factor $\eta_{\alpha\beta} = (-1)^{\alpha+\beta} e^{-(-1)^\alpha p_\alpha(\zeta,\mathbf{k}_\|)H_\alpha - (-1)^\beta p_\beta(\zeta',\mathbf{k}'_\|)H_\beta}$ which will be discussed below. The differential operator $\hat{\mathscr{L}}^{3\alpha}$ acquires now the form

$$\hat{\mathscr{L}}^{3\alpha}(\zeta, \mathbf{k}_\|) \; = \; \begin{pmatrix} -k_2 & -\frac{k_1 k_2}{\zeta\epsilon_\alpha} & \zeta + \frac{1}{\zeta\epsilon_\alpha}[k_1^2 + (-1)^\alpha p_\alpha \partial_3] & -i\frac{(-1)^\alpha p_\alpha}{\zeta\epsilon_\alpha} k_2 \\ k_1 & -\zeta - \frac{1}{\zeta\epsilon_\alpha}[k_2^2 + (-1)^\alpha p_\alpha \partial_3] & \frac{k_1 k_2}{\zeta\epsilon_\alpha} & i\frac{(-1)^\alpha p_\alpha}{\zeta\epsilon_\alpha} k_1 \\ 0 & \frac{ik_2}{\zeta\epsilon_\alpha}[(-1)^\alpha p_\alpha + \partial_3] & -\frac{ik_1}{\zeta\epsilon_\alpha}[(-1)^\alpha p_\alpha + \partial_3] & 0 \end{pmatrix} \tag{B2.30}$$

and the primed adjoint operator acts via ∂_3 on y'_3. Before we calculate from this expression the free energy and force between the surfaces, it is instructive to examine the structure of the matrix in (B2.30). It is not difficult to see that the third row of the matrix–operator $\hat{\mathscr{L}}^{k\alpha}$ can be expressed in terms of the other rows via $(-1)^\alpha i p_\alpha \hat{\mathscr{L}}^{3\alpha}_{3\mu} = \sum_{j=1}^{2} k_j \hat{\mathscr{L}}^{3\alpha}_{j\mu}$. The physical reason for this lays in the fact that there exist only two independent boundary conditions for each surface. Since the surfaces are flat here, any field configuration can be considered as a superposition of transversal magnetic (TM) and transversal electric (TE) waves as in cavities or waveguides [57]. Each mode type is characterized by a scalar field which satisfies only one boundary condition at each surface. Later, the problem will be formulated from the outset in terms of two scalar fields representing TM and TE modes. However, for deformed surfaces, this separation is no longer expected to hold since the modes will mix under the scattering at deformations.

For flat surfaces we are thus led to introduce the reduced matrix–operator

$$\Omega^\alpha(\zeta, \mathbf{k}_\|; \partial_z) \; = \; \begin{pmatrix} -k_2 & -\frac{k_1 k_2}{\zeta\epsilon_\alpha} & \zeta + \frac{1}{\zeta\epsilon_\alpha}[k_1^2 + (-1)^\alpha p_\alpha \partial_z] & -i\frac{(-1)^\alpha p_\alpha k_2}{\zeta\epsilon_\alpha} \\ k_1 & -\zeta - \frac{1}{\zeta\epsilon_\alpha}[k_2^2 + (-1)^\alpha p_\alpha \partial_z] & \frac{k_1 k_2}{\zeta\epsilon_\alpha} & i\frac{(-1)^\alpha p_\alpha k_1}{\zeta\epsilon_\alpha} \end{pmatrix}, \tag{B2.31}$$

which consists of two linear independent rows only. Defining $\Omega^\alpha_\pm(\zeta, \mathbf{k}_\|) \equiv \Omega^\alpha(\zeta, \mathbf{k}_\|; \pm\partial_z)$, the kernel can be written as

$$\begin{aligned} \tilde{\mathcal{M}}^{\alpha\beta,jl}\big(\zeta, \mathbf{k}_\|; \zeta', \mathbf{k}'_\|\big) \; &= \; (2\pi)^3 \delta\big(\zeta - \zeta'\big) \delta^{(2)}\big(\mathbf{k}_\| - \mathbf{k}'_\|\big) \\ \times \; \eta_{\alpha\beta} & \left[\Big(\mathbf{\Omega}^\alpha_+(\zeta, \mathbf{k}_\|) \cdot \mathbf{\Omega}^{\dagger\beta}_-(\zeta', \mathbf{k}'_\|)\Big)_{jl} \frac{e^{-p(\zeta,\mathbf{k}_\|)|z|}}{2p(\zeta, \mathbf{k}_\|)}\right]_{z = H_\alpha - H_\beta} . \end{aligned} \tag{B2.32}$$

The entries of this diagonal matrix consist of the 4×4 matrices which are given by the expression in the square brackets. Inserting now Eq. (B2.31) into Eq. (B2.32), we obtain for the expression in the square brackets the 4×4 matrix

$$\tilde{\mathcal{M}}(\zeta, \mathbf{k}_\|) \;=\; \begin{pmatrix} A_1 & \frac{e^{-pH}}{\epsilon_1\epsilon_2\zeta^2}B \\ \frac{e^{-pH}}{\epsilon_1\epsilon_2\zeta^2}B & A_2 \end{pmatrix} \tag{B2.33}$$

in terms of the symmetric 2×2 matrices

$$A_\alpha \;=\; \begin{pmatrix} \frac{\epsilon_\alpha-1}{\epsilon_\alpha}\zeta^2 + \frac{\epsilon_\alpha-1}{\epsilon_\alpha^2}k_1^2 + \frac{\epsilon_\alpha^2-1}{\epsilon_\alpha^2}k_2^2 & -\frac{\epsilon_\alpha-1}{\epsilon_\alpha}k_1k_2 \\ -\frac{\epsilon_\alpha-1}{\epsilon_\alpha}k_1k_2 & \frac{\epsilon_\alpha-1}{\epsilon_\alpha}\zeta^2 + \frac{\epsilon_\alpha^2-1}{\epsilon_\alpha^2}k_1^2 + \frac{\epsilon_\alpha-1}{\epsilon_\alpha^2}k_2^2 \end{pmatrix}, \tag{B2.34}$$

$$B \;=\; \begin{pmatrix} b_1 & c \\ c & b_2 \end{pmatrix}, \tag{B2.35}$$

with

$$b_\alpha \;=\; \left(p_1^2 - k_{\pi\alpha}^2 - pp_1\right)\left(p_2^2 - k_{\pi\alpha}^2 - pp_2\right) + k_{\pi\alpha}^2\left(\epsilon_1\epsilon_2\zeta^2 + k_\alpha^2 - p_1p_2\right), \tag{B2.36}$$

$$c \;=\; k_1k_2\Big((\epsilon_1+\epsilon_2-\epsilon_1\epsilon_2)\zeta^2 + \mathbf{k}_\|^2 - p(p_1+p_2) + p_1p_2\Big)\,, \tag{B2.37}$$

with $\pi\alpha \equiv 3-\alpha$ and using $p_\alpha = (\epsilon_\alpha(i\zeta)\zeta^2 + \mathbf{k}_\|^2)^{1/2}$ and $p = (\zeta^2 + \mathbf{k}_\|^2)^{1/2}$. The Casimir free energy per unit area can now be obtained from Eq. (B1.25). In the limit $H \to \infty$ the off–diagonal elements of $\tilde{\mathcal{M}}$ in Eq. (B2.33) vanish, so that we have to compute the functional determinant of the matrix

$$\tilde{\mathcal{M}}(\zeta, \mathbf{k}_\|)\tilde{\mathcal{M}}_\infty^{-1}(\zeta, \mathbf{k}_\|) \;=\; \begin{pmatrix} I & \frac{e^{-pH}}{\epsilon_1\epsilon_2\zeta^2}BA_2^{-1} \\ \frac{e^{-pH}}{\epsilon_1\epsilon_2\zeta^2}BA_1^{-1} & I \end{pmatrix}, \tag{B2.38}$$

where I is the 2×2 identity matrix. In the above matrix we have neglected the factor $\eta_{\alpha\beta}$ appearing in Eqs. (B2.29), (B2.32). This factor will have no effect on the free energy as will be shown at the end of this section. The determinant of the matrix in Eq. (B2.38) can be calculated using the relation

$$\det(Y) \;=\; 1 - \mathrm{Tr}(X_1{\cdot}X_2) + \det(X_1{\cdot}X_2) \tag{B2.39}$$

for a general 4×4 matrix of the form

$$Y \;=\; \begin{pmatrix} I & X_1 \\ X_2 & I \end{pmatrix}. \tag{B2.40}$$

Thus, the free energy can be obtained by calculating the determinant of just a 2×2 matrix. Using Eq. (B1.25), the logarithm of the product of all the determinants for different ζ_n and

$\mathbf{k}_\|$ becomes a corresponding sum and integral. This yields for the free energy per surface area A the result

$$\mathcal{E}/A \;=\; \frac{1}{2\beta}\sum_{n=-\infty}^{\infty}\int_{\mathbf{k}_\|}\ln\det\left[\tilde{\mathcal{M}}(\zeta_n,\mathbf{k}_\|)\tilde{\mathcal{M}}_\infty^{-1}(\zeta_n,\mathbf{k}_\|)\right], \tag{B2.41}$$

where the determinant runs over the discrete 4×4 matrix at fixed ζ and $\mathbf{k}_\|$. Calculating explicitly this determinant with the aid of Eq. (B2.39), we obtain

$$\begin{aligned}\mathcal{E}/A \;=\; \frac{1}{\beta}\sum_{n=0}^{\infty}{}'\int_0^\infty\frac{k\,dk}{2\pi}\,\ln\Bigg(&\left[1-e^{-2p_nH}\frac{p_{n1}-p_n}{p_{n1}+p_n}\frac{p_{n2}-p_n}{p_{n2}+p_n}\right]\\ &\times\left[1-e^{-2p_nH}\frac{p_{n1}-\epsilon_1p_n}{p_{n1}+\epsilon_1p_n}\frac{p_{n2}-\epsilon_2p_n}{p_{n2}+\epsilon_2p_n}\right]\Bigg)\end{aligned} \tag{B2.42}$$

with $k=|\mathbf{k}_\||$. The corresponding force per unit area is given by

$$\begin{aligned}F/A \;=\; -\frac{1}{\beta}\sum_{n=0}^{\infty}{}'\int_0^\infty\frac{k\,dk}{\pi}\,p_n\Bigg(&\left[\frac{p_{n1}+p_n}{p_{n1}-p_n}\frac{p_{n2}+p_n}{p_{n2}-p_n}\,e^{2p_nH}-1\right]^{-1}\\ &+\left[\frac{p_{n1}+\epsilon_1p_n}{p_{n1}-\epsilon_1p_n}\frac{p_{n2}+\epsilon_2p_n}{p_{n2}-\epsilon_2p_n}\,e^{2p_nH}-1\right]^{-1}\Bigg),\end{aligned} \tag{B2.43}$$

where we defined $p_{n\alpha}=\sqrt{\epsilon_\alpha\zeta_n^2+k^2}$ and $p_n=\sqrt{\zeta_n^2+k^2}$. The prime at the summation sign indicates that the term for $n=0$ is to be multiplied by $1/2$. It is important to note that the dielectric function in the above expressions is evaluated along the imaginary axis only, since $\epsilon_\alpha\equiv\epsilon_\alpha(i\zeta)$ due to the initial Wick rotation to the Euclidean field theory. Since $\epsilon_\alpha(i\zeta)$ is completely determined by the imaginary part of the dielectric function for real frequencies ω, the force depends only on the dissipative properties of the media, as expected from the fluctuation–dissipation–theorem. The results in Eqs. (B2.42)–(B2.43) agree with the original results obtained by Lifshitz, see Refs. [73, 78].

The limit of zero temperature is obtained by performing the continuum limit for the Matsubara frequencies, i.e. $\zeta_n\to\zeta$, thus $\frac{1}{\beta}\sum_{n\geq 0}' f(\zeta_n)\to\int_0^\infty\frac{d\zeta}{2\pi}f(\zeta)$ for any function f. Changing the integration variable to $q=\sqrt{1+k^2/\zeta^2}$ and defining $s_\alpha\equiv\sqrt{q^2-1+\epsilon_\alpha(i\zeta)}$ yields

$$\begin{aligned}\mathcal{E}/A \;=\; \int_0^\infty\frac{\zeta^2d\zeta}{2\pi}\int_1^\infty\frac{q\,dq}{2\pi}\,\ln\Bigg(&\left[1-e^{-2|\zeta|qH}\frac{s_1-q}{s_1+q}\frac{s_2-q}{s_2+q}\right]\\ &\times\left[1-e^{-2|\zeta|qH}\frac{s_1-\epsilon_1q}{s_1+\epsilon_1q}\frac{s_2-\epsilon_2q}{s_2+\epsilon_2q}\right]\Bigg)\end{aligned} \tag{B2.44}$$

for the free energy, and

$$F/A = -\frac{1}{2\pi^2}\int_0^\infty \zeta^3 d\zeta \int_1^\infty q^2 dq \left(\left[\frac{s_1+q}{s_1-q}\frac{s_2+q}{s_2-q}\, e^{2|\zeta| qH} - 1 \right]^{-1} + \left[\frac{s_1+\epsilon_1 q}{s_1-\epsilon_1 q}\frac{s_2+\epsilon_2 q}{s_2-\epsilon_2 q}\, e^{2|\zeta| qH} - 1 \right]^{-1} \right) \tag{B2.45}$$

for the force, cf. Eq. (2.9) in Ref. [73].

Finally, we come back to the omitted factor $\eta_{\alpha\beta}$. The effect of taking into account this factor is that in the matrix kernel of Eq. (B2.33), A_2 is multiplied by e^{-2p_2H} and B is multiplied by $-e^{-p_2H}$ while A_1 remains unchanged. For the matrix in Eq. (B2.38) this means that the off–diagonal matrix $\sim A_2^{-1}$ gets multiplied by the factor $-e^{p_2H}$ while the matrix $\sim A_1^{-1}$ gets multiplied by the inverse factor $-e^{-p_2H}$. Due to Eq. (B2.39), the determinant depends only on the product of the two off–diagonal matrices so that the factors coming from the $\eta_{\alpha\beta}$ drop out in the determinant of $\tilde{\mathcal{M}}\tilde{\mathcal{M}}_\infty^{-1}$.

3 The limit of ideal metal boundaries

In the previous section, we saw that our general approach reproduces the Lifshitz theory for *flat* surfaces of dielectric media. In this section we will apply the path integral approach to deformed surfaces. As an example we consider ideal metals with infinite dielectric functions ϵ_α. This is a reasonable approximation for surface separations which are large compared to the plasma wavelength λ_p of the material. However, our general result for the kernel of Eq. (B1.24) contains all information which is necessary to treat deformed surfaces of non–ideal metals or general dielectric media as well. In the latter case the kernel $\mathcal{M}$ assumes in general no particular simple form and has to be computed numerically in order to obtain the force. For ideal metals the kernel can be calculated explicitly and the result provides another interesting limit which has not been studied previously. In previous works only special deformations of ideal metals have been studied by a path integral approach. If the surface deformations are translationally invariant in one direction as for, e.g., uni–axial corrugations, the electromagnetic field can be separated into TM and TE modes. This property has been used in [35, 36, 34] to describe the surface interaction by a scalar field theory. In contrast, here we will allow for general deformations so that no separation into TM and TE modes is possible anymore.

The starting point is the general result of the kernel $\tilde{\mathcal{M}}$ in Eq. (B1.24). For asymptotically large $\epsilon_\alpha \to \infty$, both $p_\alpha(\zeta, \mathbf{k}_\|)$ and the operators $\hat{\mathscr{L}}^{k\alpha}$ become independent of the lateral momentum $\mathbf{k}_{\|}$. The kernel can then be written as

$$\begin{aligned}\tilde{\mathcal{M}}^{\alpha\beta,jl}\big(\zeta,\mathbf{k}_{\|};\zeta',\mathbf{k}'_{\|}\big) \;&=\; 2\pi\delta\big(\zeta-\zeta'\big)\int_{\mathbf{y}\in S_\alpha}\int_{\mathbf{y}'\in S_\beta} e^{-i\mathbf{k}_{\|}\cdot\mathbf{y}_{\|}+i\mathbf{k}'_{\|}\cdot\mathbf{y}'_{\|}} \\ &\times\; e^{-(-1)^\alpha|\zeta|\sqrt{\epsilon_\alpha}y_3-(-1)^\beta|\zeta|\sqrt{\epsilon_\beta}y'_3} \\ &\times\; \hat{\mathbf{n}}^\alpha_k\hat{\mathbf{n}}'^\beta_s\big[\hat{\mathscr{L}}^{k\alpha}(\zeta)\cdot\hat{\mathscr{L}}'^{\dagger s\beta}(\zeta')\big]_{jl}\,\mathcal{G}\big(\zeta;\mathbf{y}-\mathbf{y}'\big),\end{aligned} \tag{B3.46}$$

with the differential operators

$$\begin{aligned}\hat{\mathscr{L}}^{1\alpha}(\zeta) \;&=\; \begin{pmatrix} 0 & 0 & 0 & 0 \\ i\partial_3 & 0 & 0 & \zeta \\ -i\partial_2 & 0 & -\zeta & 0\end{pmatrix}, \qquad \hat{\mathscr{L}}^{2\alpha}(\zeta) \;=\; \begin{pmatrix} -i\partial_3 & 0 & 0 & -\zeta \\ 0 & 0 & 0 & 0 \\ i\partial_1 & \zeta & 0 & 0\end{pmatrix}, \\ \hat{\mathscr{L}}^{3\alpha}(\zeta) \;&=\; \begin{pmatrix} i\partial_2 & 0 & \zeta & 0 \\ -i\partial_1 & -\zeta & 0 & 0 \\ 0 & 0 & 0 & 0\end{pmatrix}.\end{aligned} \tag{B3.47}$$

Due to the simple exponential dependence of the integrand of Eq. (B3.46) on $\mathbf{k}_{\|}$, it is more convenient to transform the kernel to position space. When we insert the height profile of the surfaces with $y_3 = H_\alpha + h_\alpha(\mathbf{y}_{\|}), y'_3 = H_\beta + h_\beta(\mathbf{y}'_{\|}), H_\alpha = 0, H$ for $\alpha = 1, 2$, the position space form of the kernel can be read off from Eq. (B3.46) to be

$$\begin{aligned}\mathcal{M}^{\alpha\beta,jl}\big(\zeta,\mathbf{y}_{\|};\zeta',\mathbf{y}'_{\|}\big) \;&=\; 2\pi\delta\big(\zeta-\zeta'\big) \\ &\times\; e^{-(-1)^\alpha|\zeta|\sqrt{\epsilon_\alpha}H_\alpha-(-1)^\beta|\zeta|\sqrt{\epsilon_\beta}H_\beta}\; e^{-(-1)^\alpha|\zeta|\sqrt{\epsilon_\alpha}h_\alpha(\mathbf{y}_{\|})-(-1)^\beta|\zeta|\sqrt{\epsilon_\beta}h_\beta(\mathbf{y}'_{\|})} \\ &\times\; \hat{\mathbf{n}}^\alpha_k\hat{\mathbf{n}}'^\beta_s\big[\hat{\mathscr{L}}^{k\alpha}(\zeta)\cdot\hat{\mathscr{L}}'^{\dagger s\beta}(\zeta')\big]_{jl}\,\mathcal{G}\big(\zeta;\mathbf{y}-\mathbf{y}'\big)\Big|_{\substack{y_3=H_\alpha+h_\alpha(\mathbf{y}_{\|})\\ y'_3=H_\beta+h_\beta(\mathbf{y}'_{\|})}}\;.\end{aligned} \tag{B3.48}$$

Before proceeding, it is useful to discuss the two exponential factors depending on $\sqrt{\epsilon_\alpha}$. The second factor depends on the height profiles h_α but is independent of the mean surface distance H. Defining $\eta_\alpha(\zeta,\mathbf{y}_{\|}) = e^{-(-1)^\alpha|\zeta|\sqrt{\epsilon_\alpha}h_\alpha(\mathbf{y}_{\|})}$, the matrix has the same structure as in Eq. (B1.23), but with $\mathbf{k}_{\|}$ replaced by $\mathbf{y}_{\|}$. Due to the arguments given below Eq. (B1.23), the factors $\eta_\alpha(\zeta,\mathbf{y}_{\|})$ drop out of the free energy and can thus be neglected in the following. For the first exponential factor in Eq. (B3.48), this argument does not apply since it depends on H. However, we can use that the factor does not depend on the lateral coordinates $\mathbf{y}_{\|}$. The effect of this exponential factor is that every 2×2 sub-matrix of $\tilde{\mathcal{M}}$ which results from keeping $(j,l),(\zeta,\mathbf{k}_{\|})$ and $(\zeta',\mathbf{k}'_{\|})$ fixed is multiplied by the same only ζ dependent factors. The two diagonal elements of each of these matrices are multiplied by 1 and $e^{-2|\zeta|\sqrt{\epsilon_2}H}$, respectively, while the off–diagonal elements are multiplied by $e^{-|\zeta|\sqrt{\epsilon_2}H}$. It can be verified that this leads to a the global factor $e^{-N|\zeta|\sqrt{\epsilon_2}H}$ for the determinant of $\tilde{\mathcal{M}}$ if N denotes the dimension of the matrix $\tilde{\mathcal{M}}$. Taking the determinant of the ratio $\tilde{\mathcal{M}}\tilde{\mathcal{M}}_\infty^{-1}$, the factor will drop out and can thus be omitted from the beginning.

Now the kernel assumes a simple form. Expressing the surface normal vectors in terms of the height profile, see Eq. (B1.20), the kernel can be written as a functional of the height profile. For the same reason as for the factors $\eta_\alpha(\zeta, \mathbf{y}_\|)$ could be omitted above, we can skip the normalization factor $(-1)^\alpha/\sqrt{g_\alpha}$ of the normal vector. Thus we obtain for the differential operators

$$\left(\hat{\mathbf{n}}_k^\alpha \hat{\mathscr{L}}^{k\alpha}\right)(\zeta, \mathbf{y}_\|) = \begin{pmatrix} ih_{\alpha,2}\partial_3 - i\partial_2 & 0 & -\zeta & -h_{\alpha,2}\zeta \\ ih_{\alpha,1}\partial_3 + i\partial_1 & \zeta & 0 & h_{\alpha,1}\zeta \\ -ih_{\alpha,1}\partial_2 + ih_{\alpha,2}\partial_1 & h_{\alpha,2}\zeta & -h_{\alpha,1}\zeta & 0 \end{pmatrix} \equiv \tilde{\mathbf{\Omega}}^\alpha. \quad \text{(B3.49)}$$

We observe that the third row of the matrix in Eq. (B3.49) is linearly dependent since $\tilde{\mathbf{\Omega}}_{3\mu}^\alpha = \sum_{j=1}^2 h_{\alpha,j}\tilde{\mathbf{\Omega}}_{j\mu}^\alpha$. Therefore, as in the Lifshitz theory limit discussed earlier, the matrix has to be reduced to its first two rows. The linear dependence of rows reflects the fact that for ideal metals there are only two independent boundary conditions for each surface. As mentioned earlier, for general deformations, a reduction to TM and TE modes as it occurs in the Lifshitz theory is not possible. However, for ideal metals the boundary condition can be simply written as

$$\left[\hat{\mathbf{n}}_\alpha(\mathbf{y}) \times \mathbf{E}(\zeta, \mathbf{y})\right]_{\mathbf{y}\in S_\alpha} = 0. \quad \text{(B3.50)}$$

This boundary condition requires the two tangential components of the electric field to vanish locally. Saying it differently, the limit of infinite conductivity converts the three originally non–local boundary conditions into two local conditions. The final result for the matrix kernels is now given by a 4×4 matrix with $j, l = 1, 2$,

$$\mathcal{M}^{\alpha\beta,jl}\left(\zeta, \mathbf{y}_\|; \zeta', \mathbf{y}'_\|\right) = 2\pi\delta\left(\zeta - \zeta'\right)\left[\tilde{\mathbf{\Omega}}^\alpha \cdot \tilde{\mathbf{\Omega}}'^{\dagger\beta}\right]_{jl} \mathcal{G}\left(\zeta; \mathbf{y} - \mathbf{y}'\right)\Bigg|_{\substack{y_3 = H_\alpha + h_\alpha(\mathbf{y}_\|) \\ y'_3 = H_\beta + h_\beta(\mathbf{y}'_\|)}} \quad \text{(B3.51)}$$

with the curvature dependent differential operator

$$\left[\tilde{\mathbf{\Omega}}^\alpha \cdot \tilde{\mathbf{\Omega}}'^{\dagger\beta}\right]_{jl} = (-1)^{j+l}\left\{\zeta^2\left(\delta_{jl} + h_{\alpha,\pi j}h'_{\beta,\pi l}\right) + \left(h_{\alpha,\pi j}\partial_3 + \partial_{\pi j}\right)\left(h'_{\beta,\pi l}\partial'_3 + \partial'_{\pi l}\right)\right\} \quad \text{(B3.52)}$$

acting on the vacuum Green function. The transpose permutation $\pi j \equiv 3 - j$ was defined, and analogously to the notation for the derivatives ∂, ∂', the prime on h' in Eq. (B3.52) indicates the dependence on the primed variable $\mathbf{y}'_\|$. Inserting the Green function

$$\mathcal{G}\left(\zeta; \mathbf{y} - \mathbf{y}'\right) = \int_{\mathbf{q}_\|} e^{i\mathbf{q}_\| \cdot (\mathbf{y}_\| - \mathbf{y}'_\|)} \frac{e^{-p(\zeta, \mathbf{q}_\|)\,|y_3 - y'_3|}}{p(\zeta, \mathbf{q}_\|)} \quad \text{(B3.53)}$$

into Eq. (B3.51) yields

$$\begin{aligned}\mathcal{M}^{\alpha\beta,jl}(\zeta,\mathbf{y}_\|;\zeta',\mathbf{y}'_\|) \;=\; & 2\pi\delta(\zeta-\zeta')\int_{\mathbf{q}_\|} e^{i\mathbf{q}_\|\cdot(\mathbf{y}_\|-\mathbf{y}'_\|)}\,\hat{\Omega}^{jl}(\nabla_\|,\nabla'_\|)\\ & \times\;\frac{1}{2p}\,e^{-p|h_\alpha(\mathbf{y}_\|)-h_\beta(\mathbf{y}'_\|)+H(\delta_{\alpha 2}-\delta_{\beta 2})|},\end{aligned} \tag{B3.54}$$

with $p=p(\zeta,\mathbf{q}_\|)$ and with the 2×2 operator $\hat{\Omega}$ given by

$$\hat{\Omega}^{jl}(\nabla_\|,\nabla'_\|) \;=\; \delta_{jl}\zeta^2+\left(1-\zeta^2/p^2\right)\partial_{\pi j}\partial'_{\pi l}+i\left(q_{\pi j}\partial'_{\pi l}-q_{\pi l}\partial_{\pi j}\right)+q_{\pi j}q_{\pi l}. \tag{B3.55}$$

For the Fourier transformed kernel $\tilde{\mathcal{M}}$ one obtains from Eq. (B3.54),

$$\begin{aligned}\tilde{\mathcal{M}}^{\alpha\beta,jl}(\zeta,\mathbf{k}_\|;\zeta',\mathbf{k}'_\|) \;=\; & 2\pi\delta(\zeta-\zeta')\int_{\mathbf{y}_\|}\int_{\mathbf{y}'_\|}\int_{\mathbf{q}_\|} e^{-i(\mathbf{k}_\|-\mathbf{q}_\|)\cdot\mathbf{y}_\|+i(\mathbf{k}'_\|-\mathbf{q}_\|)\cdot\mathbf{y}'_\|}\,\hat{\Omega}^{jl}(\nabla_\|,\nabla'_\|)\\ & \times\;\frac{1}{2p}\,e^{-p|h_\alpha(\mathbf{y}_\|)-h_\beta(\mathbf{y}'_\|)+H(\delta_{\alpha 2}-\delta_{\beta 2})|}.\end{aligned} \tag{B3.56}$$

Applying integration by parts in Eq. (B3.56), the differential operator $\hat{\Omega}^{jl}$ becomes algebraic in virtue of the replacements $\nabla_\| \to i(\mathbf{k}_\|-\mathbf{q}_\|), \nabla'_\| \to i(\mathbf{q}_\|-\mathbf{k}'_\|)$. Then, $\tilde{\mathcal{M}}$ together with the formula of Eq. (B1.25) yields the exact free energy of the interacting surfaces. We note that in Eq. (B3.55), we omitted the factor $(-1)^{j+l}$, cf. Eq. (B3.52), because this factor cancels if $\det\tilde{\mathcal{M}}$ is evaluated.

Generally, it is not possible to give a closed analytical expression for the determinant of $\tilde{\mathcal{M}}$. However, either perturbative [35, 36, 34] or numerical [34] techniques can be used to evaluate the free energy and force. This will be studied in the following chapters.

4 Scalar field approaches

In general, the scope of applicability of scalar field theories is more restricted than that of gauge field formalisms, however, their advantage is that calculations become simpler in many cases and there is no need for any gauge fixing. For these reasons, we study the path integral approach for scalar fields in further detail in order to describe geometries which allow for a scalar field approach in a more simple way from the beginning. This will be done for geometries of ideal metals in chapters C,D. However, an interesting example is also given by the case of flat surfaces of dielectric media. It will be shown that that the Lifshitz theory can be obtained directly from a scalar field path integral quantization choosing appropriate boundary conditions. As mentioned earlier, no gauge fixing is necessary any more, different from the treatment in the previous section.

In the analysis done above, cf. Eqs. (B2.30)–(B2.31), we argued that the field can be decomposed into transversal magnetic (TM) and transversal magnetic (TE) modes. Each of the mode types obeys one boundary condition on each surface, which leads to a reduced matrix kernel.

To decompose the electromagnetic field into both types of modes, one needs to specify a preferred spatial direction as a reference axis. We will choose without any restrictions the y_2–direction. Having defined such a reference axis, any field configuration in a geometry which is translationally invariant along that axis is decomposable into TM and TE modes, respectively, which allows for a scalar field path integral quantization. The procedure of mode decomposition has successfully been applied in the treatment of wave guide geometries [57]. The (real–valued) scalar fields are given by the electric and magnetic field components along the axis of translational symmetry,

$$\begin{aligned} E_2(X) = \Phi(X), \quad B_2(X) = 0, \qquad & \text{for TM modes,} \\ B_2(X) = \Phi(X), \quad E_2(X) = 0, \qquad & \text{for TE modes,} \end{aligned} \tag{B4.57}$$

for any X in 4D Minkowskian spacetime. If the plates are *ideally* conducting, the boundary conditions for TM– and TE modes are of Dirichlet– and of Neumann–type, respectively, i.e.,

$$\begin{aligned} \Phi\big|_{S_\alpha} &= 0 \qquad \text{for TM modes,} \\ \partial_{\hat{\mathbf{n}}_\alpha}\Phi\big|_{S_\alpha} &= 0 \qquad \text{for TE modes,} \end{aligned} \tag{B4.58}$$

with the normal derivative pointing into the vacuum between the surfaces, as before. After a Wick rotation to imaginary time, both types of modes are described by the Euclidean action

$$S_{\mathsf{E}}\{\Phi\} = \frac{1}{2}\int_X (\nabla\Phi)^2(X) \tag{B4.59}$$

with the 4D Euclidean nabla operator $\nabla \equiv (\partial_\mu)_{\mu=0}^{3}$ and with the partition function

$$\mathcal{Z}_0 = \int \mathscr{D}\Phi\, e^{-S_{\mathsf{E}}\{\Phi\}}. \tag{B4.60}$$

Recall that in 4D Euclidean space, the surface positions on the manifolds S_α are parametrized by $X_\alpha(\mathbf{y}) = (\mathbf{y}, h_\alpha(y_1) + H\delta_{\alpha 2})$ with $\mathbf{y} = (y_0, y_1, y_2) = (y_0, \mathbf{y}_\|)$, where the vector $\mathbf{y}_\|$ represents the base plane over which the surfaces are spanned. Since the mean distance of the surfaces is H, $\int_{y_1} h_\alpha(y_1) = 0$.

Following the procedure of section B.1, the boundary conditions are imposed by inserting delta functions on the surfaces in the functional integral. Doing this for the boundary conditions for ideal metals, cf. Eq. (B4.58), we obtain a separate partition function for each wave type. They are given by

$$\mathcal{Z}_{\mathsf{D}} = \mathcal{Z}_0^{-1} \int \mathscr{D}\Phi \prod_{\alpha=1}^{2} \prod_{X_\alpha} \delta\left[\Phi(X_\alpha)\right] \, e^{-S_{\mathsf{E}}\{\Phi\}}, \tag{B4.61}$$

$$\mathcal{Z}_{\mathsf{N}} = \mathcal{Z}_0^{-1} \int \mathscr{D}\Phi \prod_{\alpha=1}^{2} \prod_{X_\alpha} \delta\left[\partial_{\hat{\mathbf{n}}_\alpha}\Phi(X_\alpha)\right] \, e^{-S_{\mathsf{E}}\{\Phi\}}, \tag{B4.62}$$

for Dirichlet and Neumann boundary conditions, respectively. The forthcoming procedure is analogous to the approach in case of the gauge field. First, the delta functions will be represented by functional integrals over auxiliary fields which couple to the free fields according to the boundary conditions. Then, the Gaussian integration over Φ can be performed, yielding for any kind of boundary condition

$$\mathcal{Z} = \int \prod_{\alpha=1}^{2} \mathscr{D}\psi_\alpha \, e^{-S_{\mathsf{eff}}\{\psi_\alpha\}} \tag{B4.63}$$

with an effective action

$$S_{\mathsf{eff}}\{\psi_\alpha\} = \frac{1}{2} \int_{\mathbf{y}} \int_{\mathbf{y}'} \psi_\alpha(\mathbf{y}) \mathcal{M}^{\alpha\beta}(\mathbf{y}, \mathbf{y}') \psi_\beta(\mathbf{y}'). \tag{B4.64}$$

Summation convention is applied to repeated indices. After subtracting the divergent and H–independent terms, the energies can be written as $\mathcal{E} = \ln\det(\mathcal{M}\mathcal{M}_\infty^{-1})/(2L)$, with L being the Euclidean length in time direction. Since the Casimir energy is given by the sum of its contributions for TM and TE modes, the same applies to the force $F = -\partial_H \mathcal{E}$,

$$F_{\mathsf{TM}} = -\frac{1}{2L} \mathrm{Tr}\left(\mathcal{M}_{\mathsf{D}}^{-1} \partial_H \mathcal{M}_{\mathsf{D}}\right), \tag{B4.65}$$

$$F_{\mathsf{TE}} = -\frac{1}{2L} \mathrm{Tr}\left(\mathcal{M}_{\mathsf{N}}^{-1} \partial_H \mathcal{M}_{\mathsf{N}}\right), \tag{B4.66}$$

cf. Eq. (B1.26), where for finite temperatures, the Euclidean length in time direction is given by $L = \beta$. The right–hand side of these expressions is always finite, and no regularization of divergences by subtraction of the vacuum energy in the absence of boundaries is necessary. This will *not* be the case in the discussion of *lateral* forces, as will be discussed in chapter D. The Dirichlet and Neumann matrix kernels of the effective Gaussian action can be expressed in terms of the Euclidean scalar Green's function $\mathcal{G}(\mathbf{y}, y_3) = \left[4\pi(\mathbf{y}^2 + y_3^2)\right]^{-1}$, and are respectively given by

$$\mathcal{M}_{\mathsf{D}}^{\alpha\beta}(\mathbf{y}, \mathbf{y}') = g_\alpha(y_1)^{1/4} g_\beta(y_1')^{1/4} \mathcal{G}\left(X_\alpha(\mathbf{y}) - X_\beta(\mathbf{y}')\right), \tag{B4.67}$$

$$\mathcal{M}_{\mathsf{N}}^{\alpha\beta}(\mathbf{y}, \mathbf{y}') = g_\alpha(y_1)^{1/4} g_\beta(y_1')^{1/4} \partial_{\hat{\mathbf{n}}_\alpha(y_1)} \partial_{\hat{\mathbf{n}}_\beta(y_1')} \mathcal{G}\left(X_\alpha(\mathbf{y}) - X_\beta(\mathbf{y}')\right), \tag{B4.68}$$

with the metric coefficients given by $g_\alpha = 1 + (\nabla_\| h_\alpha)^2 = 1 + (\partial_1 h_\alpha)^2$. They arise from the integral measure on the curved manifold S_α. However, they are independent of H and they cancel in the product of $\mathcal{M}\mathcal{M}_\infty^{-1}$ and can therefore be ignored in the calculation of forces.

Applying the parametrization in terms of height profiles, the matrix kernels can now be written as

$$\begin{aligned}
\mathcal{M}_{\mathsf{D}}^{\alpha\beta}(\mathbf{y},\mathbf{y}') &= \mathcal{G}\left(\mathbf{y}-\mathbf{y}'; h_\alpha(y_1) - h_\beta(y_1') + H(\delta_{\alpha 2} - \delta_{\beta 2})\right), && \text{(B4.69)}\\
\mathcal{M}_{\mathsf{N}}^{\alpha\beta}(\mathbf{y},\mathbf{y}') &= (-1)^{\alpha+\beta}\{-\partial_3^2 + \left[h_\alpha'(y_1) + h_\beta'(y_1')\right]\partial_1\partial_3 - h_\alpha'(y_1)h_\beta'(y_1')\partial_1^2\} \\
&\qquad \times \mathcal{G}\left(\mathbf{y}-\mathbf{y}'; y_3 - y_3')\right)\Big|_{\substack{y_3=h_\alpha(y_1)+H\delta_{\alpha 2}\\ y_3'=h_\beta(y_1')+H\delta_{\beta 2}}}, && \text{(B4.70)}
\end{aligned}$$

with $\partial_j = \frac{\partial}{\partial y_j}$. Note that these results are valid for any kind of uniaxial deformation.

4.1 Derivation of the Lifshitz theory

We consider again the limit of flat surfaces with dielectric boundaries characterized by the dielectric functions $\epsilon_\alpha(\omega)$ for $\alpha = 1, 2$.

Instead of working in position space, it is convenient to calculate with a partially Fourier transformed representation in the following, so that after a Wick rotation to imaginary frequencies $\omega \to i\zeta$, the fields depend on the set of parameters $(\zeta, \mathbf{k}_\|, z)$. Here, $\mathbf{k}_\|$ is the in–plane lateral momentum vector, the last coordinate z was kept in position space which is especially suited to a geometry with flat surfaces.

Due to the rotational symmetry in the lateral plane of the flat surface geometry, it turns out that it is useful to adapt the choice of the direction to the lateral momentum $\mathbf{k}_\|$ of the field mode. Note that this can be done since the modes for different $\mathbf{k}_\|$ are *decoupled* for flat surfaces. Therefore, in the following we will choose for a given $\mathbf{k}_\|$ the lateral coordinates so that $k_2 = 0$, and y_2 defines the longitudinal direction. Following the parametrization of the TM and TE modes for waveguides [57], the longitudinal components of the electric (for TM modes) and magnetic (for TE modes) field define the ral–valued scalar field Φ according to Eqs. (B4.57), as before.

The transversal components $E_j \equiv E_j(\zeta, \mathbf{k}_\|; z)$ and $B_j \equiv B_j(\zeta, \mathbf{k}_\|; z)$ of the electromagnetic field are then given by

$$\begin{aligned}
E_1 &= \tfrac{k_1 k_2}{\zeta^2+k_2^2}\Phi, & B_1 &= \tfrac{\zeta}{\zeta^2+k_2^2}\partial_z\Phi, \\
E_3 &= \tfrac{-ik_2}{\zeta^2+k_2^2}\partial_z\Phi, & B_3 &= \tfrac{-i\zeta k_1}{\zeta^2+k_2^2}\Phi,
\end{aligned} \qquad \text{(B4.71)}$$

for TM modes, and

$$\begin{array}{rclrcl} E_1 & = & \frac{-\zeta}{\zeta^2+k_2^2}\partial_z\Phi, & B_1 & = & \frac{k_1k_2}{\zeta^2+k_2^2}\Phi, \\ E_3 & = & \frac{i\zeta k_1}{\zeta^2+k_2^2}\Phi, & B_3 & = & \frac{-ik_2}{\zeta^2+k_2^2}\partial_z\Phi, \end{array} \tag{B4.72}$$

for TE modes, where we performed already a Wick rotation to imaginary frequency, $\omega \to i\zeta$. Using the Maxwell equations it can be shown that the dynamics of the field Φ is governed by the usual wave equation, corresponding to the Euclidean action, see Eq. (B4.59).

In the following, we restrict the discussion to the case of zero temperature. Finite temperatures $T > 0$ can be treated in analogy to the gauge field approach by introducing Matsubara frequencies. The boundary condition for the scalar field Φ can be derived from the optical extinction theorem discussed at the beginning of section B.1. There, from Eq. (B1.10) we obtain, using the Fourier representation of the material Green function $\mathcal{G}^\epsilon$, in Euclidean space the conditions

$$-\zeta\epsilon_\alpha(i\zeta)E_2 - ik_1B_3 - (-1)^\alpha p_\alpha B_1 = 0, \tag{B4.73}$$

$$\zeta\epsilon_\alpha(i\zeta)E_1 - ik_2B_3 - (-1)^\alpha p_\alpha B_2 = 0, \tag{B4.74}$$

$$i\mathbf{k}_\| \cdot \mathbf{B}_\| - (-1)^\alpha p_\alpha B_3 = 0, \tag{B4.75}$$

for the flat surface S_α. Recall that $p_\alpha = (\epsilon_\alpha(i\zeta)\zeta^2 + \mathbf{k}_\|^2)^{1/2}$ and $p = (\zeta^2 + \mathbf{k}_\|^2)^{1/2}$. Now we make use of the fact that we can constrict the analysis to the case $k_2 = 0$ by a suitable choice of the lateral coordinates. After inserting the electromagnetic field components as given by Eqs. (B4.73)–(B4.75), the above conditions collapse to a single boundary condition for the scalar field Φ which can be formulated as

$$(1 - \Gamma_\alpha\partial_{\hat{\mathbf{n}}_\alpha})\,\Phi\,|_{z=H_\alpha} = 0, \tag{B4.76}$$

with $\Gamma_\alpha = \frac{1}{p_\alpha}$ for TM modes, and $\Gamma_\alpha = \frac{\epsilon_\alpha}{p_\alpha}$ for TE modes, where $\partial_{\hat{\mathbf{n}}_\alpha} = (-1)^{\alpha-1}\partial_z$ denotes the normal derivatives at the surfaces. Due to the dependence of $\mathbf{k}_\|$, the mixed–mode boundary condition Eq. (B4.76) is non–local in position space. In the limit of ideal metals with $\epsilon_\alpha \to \infty$, it reduces to the well known Dirichlet and Neumann boundary condition (depending on the choice of Γ_α) for TM and TE modes, respectively. Note that Γ_α is real, since the same is valid for ϵ_α along the imaginary frequency axis. Therefore, Φ can be considered to be real–valued.

The restricted partition function for the field Φ reads for both types of modes

$$\mathcal{Z} = \mathcal{Z}_0^{-1}\int \mathcal{D}\Phi\, e^{-S_{\mathsf{E}}\{\Phi\}} \prod_\alpha \prod_{\zeta,\mathbf{k}_\|} \delta\left[(1 - \Gamma_\alpha\partial_{\hat{\mathbf{n}}_\alpha})\,\Phi\,|_{z=H_\alpha}\right], \tag{B4.77}$$

where the boundary constraints were again implemented by delta functions. Note the similarity to Eqs. (B4.61)–(B4.62). Now we proceed in analogy to the treatment of the gauge field path integral performed in section B.1. Introducing two auxiliary fields ψ_α, one for each surface S_α, and performing the Gaussian integration for Φ, the partition function is given by Eq. (B4.63) with an effective action S_{eff} which is given now by

$$S_{\text{eff}}\{\psi_\alpha\} = \frac{1}{2}\int_\zeta\int_{\zeta'}\int_{\mathbf{k}_\parallel}\int_{\mathbf{k}'_\parallel}\psi_\alpha(\zeta,\mathbf{k}_\parallel)\,\mathcal{M}^{\alpha\beta}(\zeta,\mathbf{k}_\parallel;\zeta',\mathbf{k}'_\parallel)\,\psi_\beta(\zeta',\mathbf{k}'_\parallel), \tag{B4.78}$$

with summation over repeated indices and the 2×2 matrix kernel

$$\begin{aligned}\mathcal{M}^{\alpha\beta}(\zeta,\mathbf{k}_\parallel;\zeta',\mathbf{k}'_\parallel) &= (2\pi)^3\delta(\zeta+\zeta')\delta(\mathbf{k}_\parallel+\mathbf{k}'_\parallel)\\ \times\ \frac{1}{2p}&\begin{pmatrix} 1-p^2\Gamma_1^2 & (1-p\Gamma_1)(1-p\Gamma_2)\,e^{-pH}\\ (1-p\Gamma_1)(1-p\Gamma_2)\,e^{-pH} & 1-p^2\Gamma_2^2\end{pmatrix}.\end{aligned} \tag{B4.79}$$

From this kernel, using Eq. (B1.25) in the zero temperature limit, one gets for the Casimir energy per unit surface area A

$$\begin{aligned}\mathcal{E}/A &= \frac{1}{2}\int_\zeta\int_{\mathbf{k}_\parallel}\ln\det\left(\mathcal{M}\mathcal{M}_\infty^{-1}\right)\\ &= \int_0^\infty\frac{d\zeta}{2\pi}\int_0^\infty\frac{k\,dk}{2\pi}\ln\left(1-e^{-2pH}\frac{1-p\Gamma_1}{1+p\Gamma_1}\frac{1-p\Gamma_2}{1+p\Gamma_2}\right),\end{aligned} \tag{B4.80}$$

with the determinant of the 2×2 matrix (B4.79) at fixed ζ and $\mathbf{k}_\parallel$, and $k = |\mathbf{k}_\parallel|$. The matrix $\mathcal{M}_\infty$ is diagonal since for $H\to\infty$ the off–diagonal elements vanish. Therefore, the determinant of the matrix product can be easily obtained, yielding the last expression in Eq. (B4.80). Substituting Γ_α by $1/p_\alpha$ or by ϵ_α/p_α we obtain the contribution of the TM and TE modes, respectively, to the energy. Obviously, the sum of both contributions yields the result obtained earlier from the gauge field approach.

5 Summary

So far, we have derived an effective Gaussian action S_{eff} which describes material properties and geometric deformations.

The general case can only be described by the gauge field approach. Within the scalar field quantization approach, we formulated the effective action for the limiting case of ideal metals, as well as for flat surfaces of dielectric materials. Both limits were also discussed for the action obtained from the gauge field quantization. The latter limit reproduces the Lifshitz theory of molecular forces. The limit of ideal metals will be studied in further detail in the coming chapters for geometries which can be treated within the framework of the scalar field approach.

To calculate the force, one needs to specify the geometric profile and the dielectric function $\epsilon(\omega)$. In general, the calculation of the force can only be performed numerically. However, different asymptotic regimes can be specified, where simplifications are possible. One example is given by the different regimes for the surface distance: for large surface distances H, the influence of material properties decreases (cf. the Lifshitz formula Eq. (B4.80)), so that ϵ can be assumed to be constant. At smaller distances, the influence of the frequency becomes more important and makes the result for the force sensitive to the choice of $\epsilon(\omega)$. In the regimes for large and small $\epsilon(\omega)$, the action can be expanded as a functional of ϵ by an expansion of the general kernel $\tilde{\mathcal{M}}$ in Eq. (B1.24). We expect that in the first case, the strong geometry dependence and non–additivity of the Casimir force should dominate. In the opposite limit of rarified media where ϵ approaches 1, the effect of the non–additivity of Casimir force decreases, which gives the possibility to compare with approximation methods which are based on additive summation of forces as e.g. the PWS approach of Casimir–Polder–potentials, see chapter A.

Both the choice of the appropriate boundary condition and the choice of the dielectric function to describe real metals are object of recent dispute, see. e.g. Ref. [45], where other types of boundary conditions as the impedance boundary condition [12, 11] are proposed. However, the approach discussed here allows for any kind of (nonlocal) boundary condition, cf. Eq. (B1.5).

C Effect of geometry on the Casimir force

In this chapter, we confine ourselves to the study of the geometrical dependence of the Casimir force in geometries with *ideally* conducting surfaces.

In the first paragraph, an approach to the Helmholtz spectrum for arbitrarily deformed boundaries will be introduced. Via the path integral formalism which was outlined in chapter B, we establish a novel trace formula between the boundary induced change of the photon density of states and the Green function of the Helmholtz equation for scalar fields, which is related to the effective Gaussian action of the path integral quantization.

In the second part of this chapter, we develop an analytic approach for the exact calculation of the Casimir interaction for the special class of periodic geometries. First, this will be done for the case of geometries with uniaxial deformations, where the fluctuating electromagnetic field can be separated into TM and TE modes which can be described by scalar fields which satisfy Dirichlet and Neumann boundary conditions, respectively, see chapter B. Later, we extend the approach to biperiodic surfaces, i.e. surfaces which are periodic in two directions.

1 Geometries and the density of states

The quantization of the electromagnetic field in a given domain V leads to the zero point vacuum energy at zero temperature of

$$\mathcal{E}_0 = \frac{1}{2}\sum_{\mathbf{k}} \omega(\mathbf{k}), \tag{C1.1}$$

with the spectrum $\{\omega(\mathbf{k})\}$ of harmonic oscillator ground state eigenfrequencies which represents the ground state of the photon gas in that domain, see e.g. Ref. [78]. For photons, the eigenmodes are $\omega(\mathbf{k}) = c|\mathbf{k}| = k$ (note that unities were chosen such that $c = 1$ and $\hbar = 1$). The sum is running over all modes of the spectrum. The sum must be regularized, since it is formally divergent.

As it was already mentioned in the discussion of boundary conditions in the last chapter B, the division of the free vacuum space into separated volumes V_ν, see Fig. C.1, defines a spectral problem in each of the volumes. For any of these, the difficulty is to calculate the spectrum $\{\omega(\mathbf{k})\}$ analytically. The spectrum turns out to be highly sensitive to changes of the confining geometry, since it depends on the constraints which are imposed to the fluctuating electromagnetic field at the boundary surfaces of the given geometry. In a succession of works, Balian and Bloch analysed specific situations regarding the distribution of eigenfrequencies in confined geometries, for both the scalar field [2] and the electromagnetic field [3] using a multiple reflection expansion. Balian and Duplantier [8] applied the multiple reflection expansion to the Casimir problem.

The problem of determining the resonance spectrum for a given geometry is also known in the spectral theory quantum billiards, see Ref. [39]. It turns out that in general, an analytic evaluation of the spectrum is not possible.

Considering the density of states (DOS)

$$\rho(\omega) = \sum_{\mathbf{k}} \delta\big(\omega - \omega(\mathbf{k})\big), \tag{C1.2}$$

the zero point energy in Eq. (C1.1) can be transformed into

$$\mathcal{E}_0 \;=\; \frac{1}{2} \int_0^\infty d\omega\, \omega\, \rho(\omega). \tag{C1.3}$$

For the geometry depicted in Fig. C.1(a), the regularization of the energy is performed as in the previous chapter B by subtracting the part for asymptotically large surface distance H. We are interested in the regularized *change* of the DOS $\delta\rho$ for the whole vacuum space given by the sum of the DOS in each of the volumes into which the space is divided with the DOS for infinite surface separation subtracted,

$$\delta\rho(\omega) = \sum_{\nu} \rho_\nu(\omega) - \rho_\infty(\omega). \tag{C1.4}$$

ρ_ν is the DOS in the volume V_ν, $\nu = 1, 2, 3$, cf. Fig. C.1(a), and ρ_∞ is the DOS for infinite surface separation. The change of the DOS contains neither volume terms nor single surface contributions, it measures only *changes* in the geometry by moving the surfaces rigidly. The regularized ground state energy for the whole system is then given by Eq. (C1.3) with ρ substituted by $\delta\rho$ in the integrand.

For more complicated geometries as the one in Fig. C.1(b), the regularization procedure is more complicated as well. For a set of finitely extended and disconnected volumes V_ν, Balian and Duplantier [7, 9] introduce a cutoff $\chi(\omega)$ into the integral for the energy in Eq. (C1.3), which reflects the fact that realistic surfaces become transparent for frequencies beyond the plasma frequency of the material. Furthermore, the DOS ρ is regularized by defining the change of the DOS with respect to a large box Σ which encloses all volumes

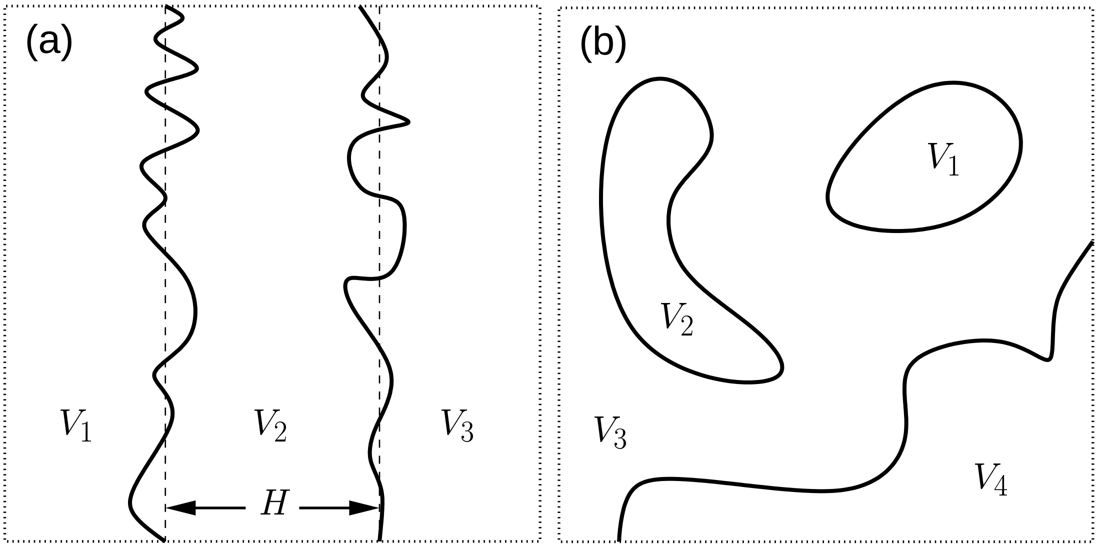

Figure C.1: Separated regions in free space by boundary surfaces. In (a), two infinitely extended surfaces S_1 and S_2 with mean distance H separate the space into 3 volumes. In (b), a more general configuration of disconnected objects of arbitrary shape is shown.

V_ν, $\delta\rho(\omega) = \sum_\nu \rho_\nu(\omega) - \rho_\Sigma(\omega)$. Then, they study the behaviour of the energy when the boundary volume Σ is inflated to infinity and when the boundary surfaces between the volumes V_ν become perfectly conducting with $\chi \to 1$.

In the following, the geometry depicted in Fig. C.1(a) will be taken into account. We consider the Helmholtz equation for scalar fields

$$\left(\nabla^2 + \omega^2\right) \Phi(\mathbf{x}) \;=\; 0, \tag{C1.5}$$

where the field Φ lives in one of the separated volumes and is assumed to satisfy Dirichlet or Neumann conditions at the boundary surface of the volume. For geometries which allow for a separation of the fluctuating electromagnetic field into TM and TE modes, as infinitely extended hollow waveguides [57], or uniaxially deformed surfaces, cf. chapter B, the scalar field with Dirichlet and Neumann conditions can be identified with TM and TE field modes, respectively. The Green function for Eq.(C1.5) satisfies

$$\left(\nabla'^2 + \omega^2\right) \mathcal{G}(\omega; \mathbf{x}, \mathbf{x}') \;=\; \delta^{(3)}(\mathbf{x} - \mathbf{x}') \tag{C1.6}$$

and the DOS in a given volume V is related to the Green function by

$$\rho(\omega) \;=\; \int_V d^3\mathbf{x}\; \rho(\omega, \mathbf{x}) \;=\; -\frac{2\omega}{\pi} \int_V d^3\mathbf{x}\; \mathrm{Im}\, \mathcal{G}(\omega; \mathbf{x}, \mathbf{x}), \tag{C1.7}$$

where $\rho(\omega, \mathbf{x})$ is the *local* DOS. Since the DOS is real and more regular along the imaginary axis, it is useful to perform a Wick rotation $\omega \longrightarrow iq_0$ to Euclidean space [1]. For the Euclidean DOS $\rho_{\mathsf{E}}(q_0) \equiv -\rho(iq_0)$, the total regularized ground state energy reads

$$\mathcal{E}_0 \;=\; \frac{1}{2}\int_0^\infty dq_0\, q_0\, \delta\rho_{\mathsf{E}}(q_0). \tag{C1.8}$$

From Eq. (C1.7), one gets then

$$\rho_{\mathsf{E}}(q_0) \;=\; -\frac{2q_0}{\pi}\int_V d^3\mathbf{x}\; \mathcal{G}_{\mathsf{E}}(q_0;\mathbf{x},\mathbf{x}) \tag{C1.9}$$

with the Euclidean Green function $\mathcal{G}_{\mathsf{E}}$, which is real along the imaginary axis[2]. In the following, we will skip the index at $\mathcal{G}_{\mathsf{E}}$ and ρ_{E} since we work completely in Euclidean space. The key result is that the *correction* of the Euclidean Green function $\mathcal{G}$ for the geometry to the *free* Euclidean Green function

$$\mathcal{G}_0\big(q_0;\mathbf{x},\mathbf{x}'\big) \;=\; \int\frac{d^3\mathbf{q}}{(2\pi)^3}\,\frac{e^{i\mathbf{q}(\mathbf{x}-\mathbf{x}')}}{q_0^2+\mathbf{q}^2} \;=\; \frac{e^{-|q_0||\mathbf{x}-\mathbf{x}'|}}{4\pi|\mathbf{x}-\mathbf{x}'|} \tag{C1.10}$$

for the vacuum space can be expressed by a *non–local* relation between the free Green functions evaluated at the surface of the geometry. This relation is given by

$$\begin{aligned}\tilde{\mathcal{G}}\big(q_0;\mathbf{x},\mathbf{x}'\big) &\equiv \mathcal{G}(q_0;\mathbf{x},\mathbf{x}') - \mathcal{G}_0(q_0;\mathbf{x},\mathbf{x}')\\ &= -\sum_{\alpha\beta}\int d\mathbf{u}\,d\mathbf{u}'\,\mathcal{G}_0\big(q_0;\mathbf{x},\mathbf{s}_\alpha(\mathbf{u})\big)\,\mathcal{M}^{-1}_{\mathsf{D},\alpha\beta}\big(q_0;\mathbf{u},\mathbf{u}'\big)\,\mathcal{G}_0\big(q_0;\mathbf{s}_\beta(\mathbf{u}'),\mathbf{x}'\big)\end{aligned} \tag{C1.11}$$

for Dirichlet boundary conditions, where $\mathbf{u},\mathbf{u}'$ are 2D coordinates of the surfaces S_α, and the corresponding space vectors $\mathbf{s}_\alpha(\mathbf{u}),\mathbf{s}_\beta(\mathbf{u}')$ parametrize the surfaces. Eq. (C1.11) is obtained by path integral quantization, details of the derivation are left to appendix F.1. For Neumann conditions, the $\mathcal{G}_0$ on the right hand side have to be replaced by their normal derivatives $\partial_{\hat{\mathbf{n}}_\alpha(\mathbf{u})}\mathcal{G}_0$ at the surface point $\mathbf{s}_\alpha(\mathbf{u})$, where $\hat{\mathbf{n}}_\alpha(\mathbf{u})$ is the normal vector pointing into the volume V where $\mathbf{x},\mathbf{x}'$ are located. $\mathcal{M}_{\mathsf{D}},\mathcal{M}_{\mathsf{N}}$ are the matrix kernels of the effective Gaussian action for Dirichlet or Neumann boundary conditions, respectively, cf. appendix F.1. Note that Eq. (C1.11) holds for every region, for Neumann conditions, the change of the direction of the normal derivative at the free Green function is compensated by the the change of the direction of the normal derivative which appears in the kernel $\mathcal{M}_{\mathsf{N}}$.

---

[1] In chapter B, the Wick rotation for the frequency was denoted as $\omega \longrightarrow i\zeta$. Hence follows $\zeta = q_0$.

[2] One has to perform the Wick rotation *first* for the local DOS for complex arguments $z \in \mathbb{C}$ given by $\rho(z,\mathbf{x}) \equiv -(2z/\pi)\mathcal{G}(z;\mathbf{x},\mathbf{x})$ and *then* take the imaginary part.

Integrating both sides of Eq. (C1.11), over the whole space, one obtains for any kind of boundary condition

$$\int d^3\mathbf{x}\, \tilde{\mathcal{G}}(q_0;\mathbf{x},\mathbf{x}) \;=\; \frac{1}{2q_0}\frac{\partial}{\partial q_0}\mathrm{Tr}\ln(\mathcal{M}). \tag{C1.12}$$

From Eq. (C1.9), we obtain for the change of the DOS

$$-\frac{\pi}{2q_0}\,\delta\rho(q_0) \;=\; \int d^3\mathbf{x}\, \mathcal{G}(q_0;\mathbf{x},\mathbf{x}) - \int d^3\mathbf{x}\, \mathcal{G}_\infty(q_0;\mathbf{x},\mathbf{x}). \tag{C1.13}$$

On the right hand side of Eq. (C1.13), the Green function $\mathcal{G}_\infty$ for $H \to \infty$ has to be subtracted to get the *change* of the DOS, $\delta\rho$. The Green functions $\mathcal{G}, \mathcal{G}_\infty$ can be replaced by their corrections to the free Green function, which are given by $\tilde{\mathcal{G}} = \mathcal{G} - \mathcal{G}_0$ and $\tilde{\mathcal{G}}_\infty = \mathcal{G}_\infty - \mathcal{G}_0$, respectively, since the free Green function will be cancelled in Eq. (C1.13). Subtracting the contribution for $H \to \infty$ also from the result in Eq. (C1.12) and comparing with Eq. (C1.13), we obtain the trace formula

$$\delta\rho(q_0) \;=\; -\frac{1}{\pi}\frac{\partial}{\partial q_0}\mathrm{Tr}\ln(\mathcal{M}\mathcal{M}_\infty^{-1}), \tag{C1.14}$$

where the trace is taken over the 2D parametrization vectors $\mathbf{u}, \mathbf{u}'$ and the discrete surface indices α, β of the matrix $\mathcal{M}$.

The trace formula Eq. (C1.14) relates the change of the DOS with the matrix kernel $\mathcal{M}$ of the effective Gaussian action. It has the advantage that all geometric informations about the system are implicitly contained in the kernel $\mathcal{M}$. No complicated integrations over finite space regions need to be performed. A formally similar expression has been derived by Balian and Duplantier [7] within the framework of a multiple reflection expansion for the Casimir effect, the operator to which the trace is applied contains information about multiple reflection paths of surface scatterings, see Eq. (7.20) of [7].

In quantum spectral theory, the so–called Krein–Friedel–Lloyd formula [64] has the same structure as the trace formula, but is applied to quantum scattering described by the S-matrix or the so–called Kohringa–Kohn–Rostoker (KKR) multiple scattering matrix [20, 63, 62], see also [50].

At finite temperatures, the photon field is no longer in the vacuum state. Then, the expression for the energy in Eq. (C1.8) has to be replaced by by an expression of the form

$$\mathcal{E}_0 \;=\; \int_0^\infty dq_0\, f(q_0)\,\delta\rho(q_0), \tag{C1.15}$$

see Ref. [9], with the temperature dependent weight

$$f(q_0) \;=\; \left\{ \begin{array}{ll} q_0/2 & \text{if} \quad T=0 \\ \pi T \sum_{n=0}^{\prime\infty} \Theta\left(q_0 - 2\pi n T\right) & \text{if} \quad T>0 \end{array} \right. . \tag{C1.16}$$

Recall that the prime at the summation sign indicates that the term for $n = 0$ is weighted by the factor $1/2$. In the limit of $T \to 0$, Eq. (C1.8) is restored from Eq. (C1.15). For $T > 0$, one obtains via partial integration

$$\mathcal{E} \,=\, T \sum_{n=0}^{\infty}{}' \, \mathrm{Tr} \ln \left[\mathcal{M}(q_0) \mathcal{M}_{\infty}^{-1}(q_0) \right] , \tag{C1.17}$$

which is identical to the result in Eq. (B2.41). Since the Casimir force is given by $F = -\partial_H \mathcal{E}$, the DOS is related to the Casimir force by

$$F \,=\, - \int_0^{\infty} dq_0 \, f(q_0) \, \partial_H \delta\rho(q_0). \tag{C1.18}$$

Thus, the contributions to the interaction at fixed frequency q_0 is determined by the geometric properties of the DOS, characterized by the term $\partial_H \delta\rho(q_0)$, which describes the variation of the change of the DOS with the distance H. In the following paragraphs, we consider specific model situations for the calculation of the Casimir interaction.

2 Periodically shaped boundaries

In this paragraph, periodically deformed geometries will be considered. These geometries have the advantage that they allow for a discrete decomposition of the kernel $\mathcal{M}$ in Fourier space, which can be attributed to the fact that the spectrum of surface deformations is bounded. For arbitrary surface deformations, as in the case of stochastic roughness, this is generally not the case and it may be of advantage to resort to a position space representation of the kernel $\mathcal{M}$.

This property of periodic profiles suggests to analyse the problem in Fourier space, which will be done in the present section. In the first paragraph, we constrict the analysis to the translationally invariant geometries which can be treated within the framework of a scalar field formalism. Numerical evaluations will be presented in the next chapter for special cases of periodic geometries. However, the formalism which will be discussed here can also be extended to the more general case of biperiodic surface deformations which have to be described by means of the gauge field theory. This will be pointed out in the second paragraph.

2.1 Uniaxial periodic corrugations

As before in the discussion of the scalar field approach, cf. chapter B, the system under consideration is given by two surfaces S_α of ideal conductivity, which are parametrized over the (time dependent) base plane spanned by $\mathbf{y} = (y_0, y_1, y_2)$ by the vector $X_\alpha(\mathbf{y}) = (\mathbf{y}, h_\alpha(y_1) + \delta_{\alpha 2}H))$, where h_α is periodic, $h_\alpha(y_1) = h_\alpha(y_1 + \lambda)$ with the corrugation wavelength λ, cf. Fig. D.1.

The path integral quantization of the scalar field which satisfies Dirichlet and Neumann boundary conditions yields the effective Gaussian action governed by the matrix kernels $\mathcal{M}_{\mathsf{D}}$ and $\mathcal{M}_{\mathsf{N}}$, cf. Eqs. (B4.69)–(B4.70),

$$\begin{aligned}
\mathcal{M}_{\mathsf{D}}^{\alpha\beta}(\mathbf{y},\mathbf{y}') &= \mathcal{G}\left(\mathbf{y}-\mathbf{y}'; h_\alpha(y_1) - h_\beta(y_1') + H(\delta_{\alpha 2} - \delta_{\beta 2})\right), && \text{(C2.19)}\\
\mathcal{M}_{\mathsf{N}}^{\alpha\beta}(\mathbf{y},\mathbf{y}') &= (-1)^{\alpha+\beta}\{-\partial_3^2 + \left[h_\alpha'(y_1) + h_\beta'(y_1')\right]\partial_1\partial_3 - h_\alpha'(y_1)h_\beta'(y_1')\partial_1^2\} \\
&\qquad \times \mathcal{G}\left(\mathbf{y}-\mathbf{y}'; y_3 - y_3')\right)\Big|_{\substack{y_3 = h_\alpha(y_1) + H\delta_{\alpha 2}\\ y_3' = h_\beta(y_1') + H\delta_{\beta 2}}}. && \text{(C2.20)}
\end{aligned}$$

From the matrix kernel the Casimir interaction is evaluated via $F = \mathrm{Tr}\left(\mathcal{M}^{-1}\partial_H\mathcal{M}\right)/(2L)$, cf. Eqs. (B4.65)–(B4.70) in chapter B. Due to the translational invariance of the geometry along the spatial direction y_2, and since the surfaces are static, i.e. the profiles h_α are independent of y_0, it is useful to define the vector $\mathbf{y}_\perp \equiv (y_0, y_2)$, which is perpendicular to the direction of modulation and which comprises the components of translational invariance. Inserting the Green function

$$\mathcal{G}(\mathbf{y}, z) = \int_{\mathbf{q}} e^{i\mathbf{q}\cdot\mathbf{y}}\,\frac{e^{-q|z|}}{2q} = \int \frac{d^3\mathbf{q}}{(2\pi)^3}\,e^{i\mathbf{q}\cdot\mathbf{y}}\,\frac{e^{-q|z|}}{2q} \tag{C2.21}$$

into the matrices $\mathcal{M}_{\mathrm{D}}, \mathcal{M}_{\mathrm{N}}$, and since, due to the periodicity of the modulation, the partially Fourier transformed Green function $e^{-q|z|}/(2q)$ for $z = h_\alpha(y_1) - h_\beta(y_1') + H(\delta_{\alpha 2} - \delta_{\beta 2})$ is a periodic function in (y_1, y_1'), it can be expanded into a Fourier series as

$$\frac{1}{2q}\,e^{-q|h_\alpha(y_1) - h_\beta(y_1') + H(\delta_{\alpha 2} - \delta_{\beta 2})|} = \sum_{m,n=-\infty}^{\infty} \varphi_{mn}^{\alpha\beta}(q)\,e^{2\pi i(my_1 + ny_1')/\lambda} \tag{C2.22}$$

with the Fourier coefficients

$$\varphi_{mn}^{\alpha\beta}(q) = \frac{1}{\lambda^2}\int_0^\lambda dy_1 \int_0^\lambda dy_1'\,e^{-2\pi i(my_1 + ny_1')/\lambda}\,\frac{1}{2q}\,e^{-q|h_\alpha(y_1) - h_\beta(y_1') + H(\delta_{\alpha 2} - \delta_{\beta 2})|} \tag{C2.23}$$

which depend on H and the modulation functions h_α, and $q = \sqrt{q_0^2 + q_1^2 + q_2^2}$. In general, they can only be computed numerically. Inserting Eq. (C2.22) into $\mathcal{M}_{\mathrm{D}}, \mathcal{M}_{\mathrm{N}}$, as it is performed in appendix F in detail for a rectangular corrugation, one obtains for the Fourier transform in general the expansion

$$\tilde{\mathcal{M}}\left(\mathbf{p}, \mathbf{q}\right) = (2\pi)^3\delta^{(2)}\left(\mathbf{p}_\perp + \mathbf{q}_\perp\right)\sum_{m=-\infty}^{\infty}\delta\left(p_1 + q_1 + 2\pi m/\lambda\right)\,N_m\left(q_\perp, q_1\right). \tag{C2.24}$$

Here and in the following, the indices D,N for Dirichlet– and Neumann–boundary conditions will be skipped if the given expression applies to both cases. The 2×2–matrices $N_m\left(q_\perp, q_1\right)$ depend on the length $q_\perp = \sqrt{q_0^2+q_2^2}$ of the perpendicular vector $\mathbf{q}_\perp$. Since the Fourier coefficients in Eq. (C2.23) enter via Eq. (C2.21) and Eq. (C2.22), into the matrix $\mathcal{M}$, the matrices N_m can only be calculated analytically if this applies also to the Fourier coefficients $\varphi_{mn}^{\alpha\beta}$, which is the case for the rectangular geometry discussed in chapter D, see also in the appendix F.

Note that the discrete Fourier expansion of the matrix kernel $\tilde{\mathcal{M}}$ in Eq. (C2.24) can be interpreted as a consequence of Blochs theorem, since the boundary conditions for the fluctuating field are imposed on a surface with periodic deformation.

The nonzero entries of $\tilde{\mathcal{M}}$ are arranged in the 2×2 blocks N_m along bands parallel to the diagonal where q_1 differs by an integer multiple of $2\pi/\lambda$ from p_1, see Fig. C.2. The matrix $\tilde{\mathcal{M}}$ can be transformed into block–diagonal form by row and column permutations. To do so, we discretize the momenta $p_1, q_1 \in \frac{2\pi}{W}\{0,\,\ldots\,,N\}$ with $N = W/\lambda - 1$ and W being the length of the system in the direction of modulation, which is considered to be a (large) integer multiple of λ. Taking this parametrization, the matrix $\tilde{\mathcal{M}}$ decomposes into the $2(N+1)\times 2(N+1)$–blocks $\mathcal{B}_{kl}$ for $k,l=-\infty,\ldots\infty$

$$\mathcal{B}_{kl}(q_\perp) \;=\; \mathrm{diag}\{B_{kl}\left(q_\perp, 2\pi j/W\right)|j=0,\,\ldots\,N\} \tag{C2.25}$$

with

$$B_{kl}\left(q_\perp, q_1\right) \;=\; N_{k-l}\left(q_\perp, q_1 + 2\pi l/\lambda\right), \tag{C2.26}$$

see the left part of Fig.C.2, where the matrix $\tilde{\mathcal{M}}$ is depicted for $k,l=-1,0,1$.

By subsequent row and column permutations, $\tilde{\mathcal{M}}$ transforms into the block diagonal matrix

$$\tilde{\mathcal{M}}\left(\mathbf{p}_\perp, \mathbf{q}_\perp\right) \;=\; \mathrm{diag}\{\tilde{\mathcal{M}}_j\left(\mathbf{p}_\perp, \mathbf{q}_\perp\right)|j=0,\,\ldots\,N\} \tag{C2.27}$$

with

$$\tilde{\mathcal{M}}_j\left(\mathbf{p}_\perp, \mathbf{q}_\perp\right) \;=\; (2\pi)^2\delta^{(2)}\left(\mathbf{p}_\perp+\mathbf{q}_\perp\right)\,\left\{B_{kl}\left(q_\perp, 2\pi j/W\right)\right\}_{k,l=-\infty}^{\infty}. \tag{C2.28}$$

As it is illustrated in Fig.C.2, the blocks $\tilde{\mathcal{M}}_j$ consist of the elements of all $\mathcal{B}_{kl}$, which are located at the same position in each matrix $\mathcal{B}_{kl}$ for any fixed k,l. Hence, each block $\tilde{\mathcal{M}}_j$ is composed of exactly those elements which correspond to the same discrete momentum $q_1 = 2\pi j/W$. Since $\dim(N_m)=2$, the number of permutations is even, so that the determinants of the matrix $\tilde{\mathcal{M}}$ are the same before and after having performed the permutations to transform it into block–diagonal form. Thus,

$$\mathrm{Tr}\ln\tilde{\mathcal{M}} \;=\; \ln\det\tilde{\mathcal{M}} \;=\; \ln\prod_{j=1}^{N}\det\tilde{\mathcal{M}}_j \;=\; \sum_{j=1}^{N}\mathrm{Tr}\ln\tilde{\mathcal{M}}_j \tag{C2.29}$$

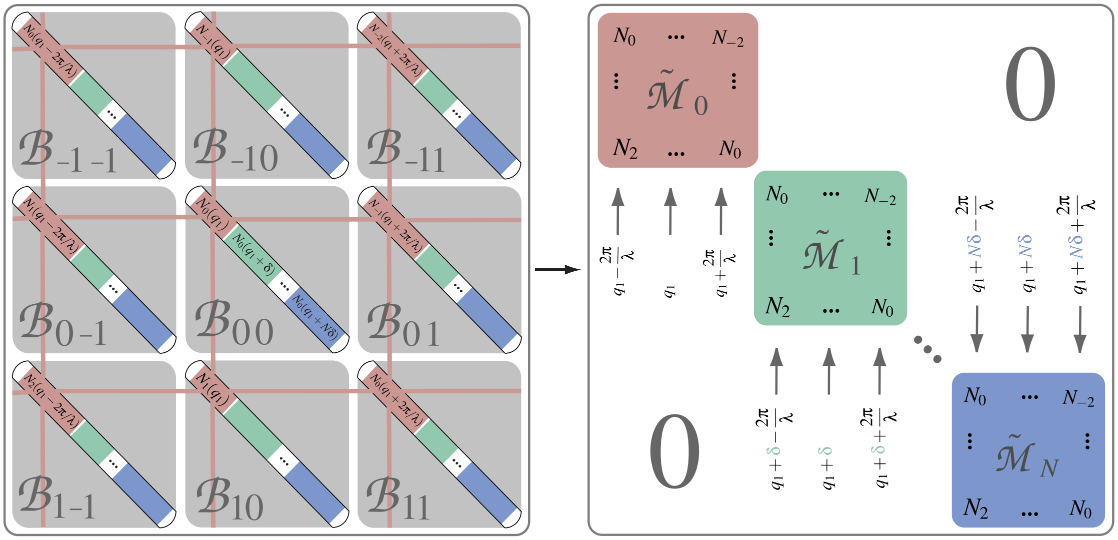

Figure C.2: Transformation of the matrix $\tilde{\mathcal{M}}$ to block–diagonal form. The figure shows a finite part of the matrix, corresponding to the blocks $\mathcal{B}_{kl}$ with $k, l = -1, 0, 1$, before and after the permutations of rows and columns. Before the transformation, $\tilde{\mathcal{M}}$ has a band structure with diagonal blocks $\mathcal{B}_{kl}$ consisting of 2×2–matrices N_m along the diagonal. First, the rows and columns which are formed by the first entry N_m in every block $\mathcal{B}_{kl}$, indicated as a grid, are permuted and compose the first block $\tilde{\mathcal{M}}_0$ of $\tilde{\mathcal{M}}$ (right box). This process is repeated N times until the $(N+1)$th entry of the $\mathcal{B}_{kl}$ to get $\tilde{\mathcal{M}}_{\mathrm{N}}$ (right box). The momenta q_1 within each block $\tilde{\mathcal{M}}_j$ are constant for every column and differ only by integer multiples of $2\pi/\lambda$ between columns of the same block, as indicated by the labels in the right box. The blocks differ in momentum by the shift $j\delta, \delta = 2\pi/W$, which is located in the unit cell $[0, 2\pi/\lambda[$ since $j = 0, \ldots, N = W/\lambda - 1$. The dependence on the lateral momentum $\mathbf{q}_\perp$ is not shown.

and then, the derivative with respect to the surface distance reads

$$\partial_H \operatorname{Tr} \ln \tilde{\mathcal{M}} = \sum_{j=1}^{N} \operatorname{Tr}\big(\tilde{\mathcal{M}}_j^{-1} \partial_H \tilde{\mathcal{M}}_j\big). \tag{C2.30}$$

Eqs. (C2.29)–(C2.30) reflect that free energy is *additive*, i.e. it can be calculated by taking the sum of their contributions to the decoupled subsystems described by the matrices $\tilde{\mathcal{M}}_j$. Each of these subsystems takes into account the scattering at the fixed momenta $q_j = 2\pi j/W + 2\pi l/\lambda$ which only differ by integer multiples of $2\pi/\lambda$.

The total trace over the matrix $\tilde{\mathcal{M}}_j$, which consists of contributions over all discrete and continuous degrees of freedom, can be performed using Eq.(C2.28) to yield

$$\mathrm{Tr}\big(\mathcal{M}_j^{-1}\partial_H\mathcal{M}_j\big) \;=\; \frac{LW}{(2\pi)^2}\int d^2\mathbf{q}_\perp \sum_{\substack{k,l=-\infty\\ \alpha,\beta=1,2}}^{\infty}\left[B^{-1}_{kl,\alpha\beta}\cdot\partial_H B_{lk,\beta\alpha}\right](q_\perp,2\pi j/W)\,. \qquad \text{(C2.31)}$$

The sum on the right hand side of Eq.(C2.31) comprises the contribution of the discrete arguments to the trace which we denote by tr in the following. The indices α,β on B enumerate the matrix elements of the 2×2–matrices N_m, cf. Eq.(C2.26). Recall that L is the system size in time direction, cf. Eqs. (B4.69)–(B4.70). We define the function

$$g(\mathbf{q}) \;\equiv\; \mathrm{tr}\left\{B^{-1}(q_\perp,q_1)\cdot\partial_H B(q_\perp,q_1) - B^{-1}_\infty(q_\perp,q_1)\cdot\partial_H B_\infty(q_\perp,q_1)\right\}. \qquad \text{(C2.32)}$$

The index ∞ in Eq. (C2.32) assigns the asymptotic expressions for $H\to\infty$. Note that the term containing the asymptotic expressions vanishes, since the limit is taken *before* performing the derivative.

The continuum limit for q_1 is performed by taking both N and W to infinity such that $\lambda = W/(N+1)$ remains constant. Then the sum over $j=0,\ldots,N$ in Eq.(C2.30) forms an integral, and one obtains

$$\partial_H \mathrm{Tr}\ln\big(\tilde{\mathcal{M}}\tilde{\mathcal{M}}_\infty^{-1}\big) \;=\; LW^2\int_{-\infty}^{\infty}\frac{dq_0}{2\pi}\int_{-\infty}^{\infty}\frac{dq_2}{2\pi}\int_0^{2\pi/\lambda}\frac{dq_1}{2\pi}\,g(q_0,q_1,q_2). \qquad \text{(C2.33)}$$

Due to the definition of g, the left hand side of Eq.(C2.33) is already regularized. The change of the DOS for the system is related to the function g by

$$\frac{1}{A}\,\partial_H\delta\rho(q_0) \;=\; -\frac{1}{\pi}\int_0^{2\pi/\lambda}\frac{dq_1}{2\pi}\int_{-\infty}^{\infty}\frac{dq_2}{2\pi}\,\partial_{q_0}g(q_0,q_1,q_2), \qquad \text{(C2.34)}$$

where $A=W^2$ is the surface area of the system. As explained at the end of the previous paragraph after Eq. (C1.18), the term on the left hand side of Eq. (C2.34) determines the contribution to the Casimir force at fixed frequency q_0.

The function g has the following symmetries: at first, a shift in the momentum $q_1\to q_1+2\pi/\lambda$ leads to renumbering of the matrix elements B_{kl}, since the matrix $\tilde{\mathcal{M}}$ has infinite dimension. Thus, $g(q_\perp,q_1) = g(q_\perp,q_1+2\pi/\lambda)$. Secondly, if the surface profiles have reflection symmetry, i.e. $h_\alpha(-y_1)=h_\alpha(y_1)$, this symmetry translates to the function g as $g(q_\perp,-q_1)=g(q_\perp,q_1)$, since $N_m(q_\perp,-q_1)=N_{-m}(q_\perp,q_1)$.

The normal Casimir force $F/A = -1/(2LW^2)\mathrm{Tr}(\tilde{\mathcal{M}}^{-1}\partial_H\tilde{\mathcal{M}})$ per surface area $A=W^2$, cf. Eqs. (B4.65), (B4.66) can now be expressed as

$$F/A \;=\; -\frac{1}{8\pi^2}\int_0^{\infty}q_\perp dq_\perp\int_0^{2\pi/\lambda}dq_1\,g\left(q_\perp,q_1\right). \qquad \text{(C2.35)}$$

Note that from the symmetry relation $g(q_\perp, -q_1) = g(q_\perp, q_1)$, the integration over q_1 in Eq. (C2.35) can be restricted to the interval $[0, \pi/\lambda)$, which gives an additional factor 2 on the right hand side of this equation. However, in the general case where $h_\alpha(-y_1) \neq h_\alpha(y_1)$, one has to resort to Eq. (C2.35), which represents the key result of this section.

In the next chapter, this result will be used for a numerical computation of the normal and lateral Casimir force in a geometry with rectangular gratings, see Fig. D.1. As it was pointed out above, this geometry allows for an analytic evaluation of the Fourier coefficients in Eq.(C2.23) and thus for the matrices N_m. For general periodic modulations the input of the numerical computation are (numerically) evaluated matrices N_m from the Fourier expansion in Eq.(C2.24).

In any case, it is necessary to resort to a numerical algorithm to compute the function g from the input matrices N_m, since the inversion of the matrix B which enters into Eq. (C2.32) is not practicable analytically. Then, all following operations as the computation of the trace and the integration in Eq. (C2.35) to get the force have also to be performed numerically. Before implementing the numerical algorithm to calculate the Casimir force, one needs a cutoff for the dimension of $\tilde{\mathcal{M}}$. Since $\tilde{\mathcal{M}}$ is composed of the blocks $\mathcal{B}_{kl}$, see Fig.C.2 and Eq.(C2.25), a cutoff M is defined by a restriction of the discrete indices $k, l \in \{-M, \ldots, M\}$. Then, $\dim(\tilde{\mathcal{M}}) = 2(2M+1)(N+1)$. Fig.C.2 displays the restricted matrix for $M = 1$. For the correspondingly defined function g_M, the discrete trace tr in Eq.(C2.32) is restricted to the summation over $k, l = -M, \ldots, M$ as well. Inserting g_M into Eq.(C2.35) defines the result F_M which converges to F for $M \to \infty$. To examine the convergence, the case of two *flat* plates at distance H will be considered. Then, $\tilde{\mathcal{M}}$ is diagonal and $N_m \sim \delta_{m0}$. Thus, the matrix B is also diagonal with $B_{kl}\,(q_\perp, q_1) \;=\; \delta_{kl}\, N_0\,(q_\perp, q_1 + 2\pi l/\lambda)$. Note that now, the corrugation wavelength λ is a "dummy" parameter since there is no corrugation any more. The result for g_M is

$$g_M\,(q_\perp, q_1) \;=\; \sum_{l=-M}^{M} \frac{2\tilde{q}_l}{e^{2\tilde{q}_l H} - 1} \tag{C2.36}$$

with $\tilde{q}_l \;\equiv\; \sqrt{q_0^2 + q_2^2 + (q_1 + 2\pi l/\lambda)^2}$. The Mth order approximation F_M to the force is obtained by integration over q_1 and yields

$$\begin{aligned} F_M/A &= -\frac{1}{8\pi^2}\int_0^\infty q_\perp dq_\perp \int_0^{2\pi/\lambda} dq_1\, g_M\,(q_\perp, q_1) \\ &= -\frac{1}{4\pi^2\lambda^2}\int_0^\infty q_\perp dq_\perp \int_{-2\pi M}^{2\pi(M+1)} du\, \frac{\tilde{u}}{e^{2\tilde{u}H/\lambda} - 1}. \end{aligned} \tag{C2.37}$$

In the last row of Eq. (C2.37), the dimensionless variable $\tilde{u} = (\lambda^2 q_\perp^2 + u^2)^{1/2}$ was introduced. For $M \to \infty$, the right hand side of Eq. (C2.37) yields $F/A = -\frac{\pi^2}{480 H^4}$, which is the well known result for the Casimir force per surface between flat plates. The correction to the finite order result is determined by the dimensionless ratio H/λ and decays exponentially fast to zero as $F - F_M \sim e^{-4\pi MH/\lambda}$ for large M. Thus, a numerical approach should give accurate results for large M. In general, we expect that the convergence becomes faster for increasing values of H/λ.

2.2 Biperiodic boundary surfaces

The analysis in the previous section applies to geometries with a translational symmetry where the field modes separate into contributions of TM and TE modes, which can be treated within the framework of scalar field quantization. However, if this translational symmetry does no longer exist, as in the case of biperiodic surface modulations, the modes will mix under the scattering at deformations and thus, a representation of the modes by scalar fields is no longer expected to hold. In this case, one has to resort to the gauge field formalism outlined in chapter B. Biperiodic profile functions satisfy $h_\alpha(\mathbf{y}_\parallel) = h_\alpha(y_1, y_2) = h_\alpha(y_1+\lambda_1, y_2+\lambda_2)$ with corrugation wavelengths λ_1 and λ_2. No numerical computations were made to calculate the Casimir forces between biperiodic profiles. However, it is interesting to study how the previously discussed matrix transformation translates to the more general case of biperiodic surface deformations.

Analogously to the former case treated within the scalar field approach, the response kernel $\tilde{\mathcal{M}}$ of the effective Gaussian action from the gauge field path–integral quantization contains the partially Fourier transformed Green function $e^{-q|z|}/(2q)$ with $z = h_\alpha(\mathbf{y}_\parallel) - h_\beta(\mathbf{y}'_\parallel) + H(\delta_{\alpha 2} - \delta_{\beta 2})$, cf. Eq. (B3.54) and Eq. (B3.56), which is now a periodic function in (y_1, y'_1, y_2, y'_2) and which can be expanded as

$$\frac{1}{2q}\, e^{-q|h_\alpha(\mathbf{y}_\parallel)-h_\beta(\mathbf{y}'_\parallel)+H(\delta_{\alpha 2}-\delta_{\beta 2})|} = \sum_{\substack{m_j,n_j=-\infty \\ (j=1,2)}}^{\infty} \varphi^{\alpha\beta}_{m_1 m_2, n_1 n_2}(q)\, e^{\frac{2\pi i}{\lambda_1}(m_1 y_1 + n_1 y'_1)} e^{\frac{2\pi i}{\lambda_2}(m_2 y_2 + n_2 y'_2)} \tag{C2.38}$$

with the Fourier coefficients

$$\varphi^{\alpha\beta}_{m_1 m_2, n_1 n_2}(q) = \frac{1}{\lambda_1^2 \lambda_2^2} \int_0^{\lambda_1} dy_1 \int_0^{\lambda_1} dy'_1\, e^{-\frac{2\pi i}{\lambda_1}(m_1 y_1 + n_1 y'_1)} \int_0^{\lambda_2} dy_2 \int_0^{\lambda_2} dy'_2\, e^{-\frac{2\pi i}{\lambda_2}(m_2 y_2 + n_2 y'_2)} \times \frac{1}{2q}\, e^{-q|h_\alpha(\mathbf{y}_\parallel)-h_\beta(\mathbf{y}'_\parallel)+H(\delta_{\alpha 2}-\delta_{\beta 2})|}. \tag{C2.39}$$

In general, the Fourier coefficients $\varphi^{\alpha\beta}_{mn,ks}$ have to be calculated numerically. By inserting Eq. (C2.38) into Eq. (B3.54), in analogy to the one dimensional case, $\tilde{\mathcal{M}}$ can be transformed

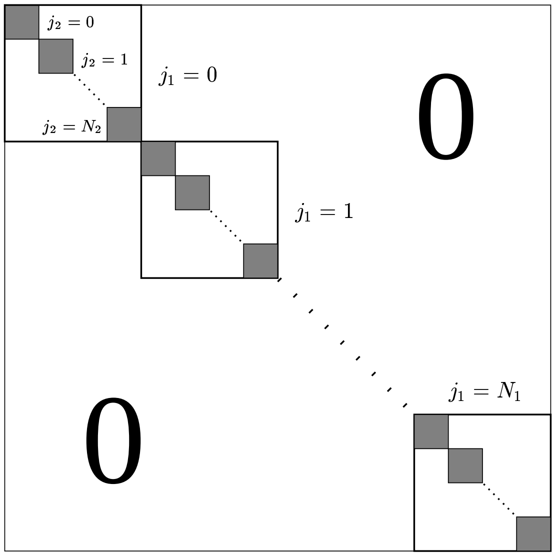

Figure C.3: Nested structure of the discretized matrix $\tilde{\mathcal{M}}$ after having performed the permutation algorithm to convert it to block diagonal form. The only regions with nonzero entries are the grey shaded infinite block matrices $\mathcal{M}_{j_1 j_2}$ at fixed j_1, j_2 along the diagonal.

into

$$\begin{aligned} \tilde{\mathcal{M}}^{\alpha\beta,jl}(\mathbf{p},\mathbf{q}) &= (2\pi)^3\delta(p_0+q_0) \\ &\times \sum_{m=-\infty}^{\infty}\sum_{n=-\infty}^{\infty}\delta\left(p_1+q_1+2\pi m/\lambda_1\right)\delta\left(p_2+q_2+2\pi n/\lambda_2\right)\, N_{m,n}^{\alpha\beta,jl}(\mathbf{q})\,, \end{aligned} \tag{C2.40}$$

where $N_{m,n}(\mathbf{q})$ are now 4×4 matrices, which can only be obtained analytically if the Fourier coefficients $\varphi^{\alpha\beta}_{m_1 m_2, n_1 n_2}(q)$ are known analytically as well.

The transformation of $\tilde{\mathcal{M}}$ to block–diagonal form is now achieved by discretizing the momenta $p_j, q_j \in \frac{2\pi}{W}\{0,\ldots,N_j\}$ with integers $N_j = W/\lambda_j - 1$ for $j = 1,2$ where W is the system length in the y_j directions. Then the permutation process outlined above will be used *twice*, which gives finally the nested block diagonal form

$$\tilde{\mathcal{M}}\left(p_0, q_0;\, N_1, N_2\right) = (2\pi)^3\delta\left(p_0+q_0\right)\,\mathrm{diag}\left\{\mathrm{diag}\left\{\mathcal{M}_{j_1 j_2}\left(q_0\right)\right\}_{j_2=0}^{N_2}\right\}_{j_1=0}^{N_1}, \tag{C2.41}$$

see Fig. C.3, with the block matrices $\tilde{\mathcal{M}}_{j_1 j_2}(q_0) = B\left(q_0; \frac{2\pi j_1}{W_1}, \frac{2\pi j_2}{W_2}\right)$, and the matrix B is defined as

$$B^{\alpha\beta,rs}_{k_1 l_1, k_2 l_2}(q_0, q_1, q_2) = N^{\alpha\beta,rs}_{k_1-l_1, k_2-l_2}\left(q_0, q_1 + 2\pi\tfrac{l_1}{\lambda_1}, q_2 + 2\pi\tfrac{l_2}{\lambda_2}\right). \tag{C2.42}$$

The discretized matrix $\tilde{\mathcal{M}}$ now depends on the integers N_1, N_2 which was noted in (C2.41). Later, these integers together with W will be taken to infinity such that the corrugation wavelengths $\lambda_j = W/(N_j + 1)$ remain constant. Furthermore, the k_j, l_j are running over all integers, such that every block B has infinite dimension. For the numerical calculations, it will be necessary to introduce a cutoff M_j such that $k_j, l_j = -M_j, \ldots, M_j$. Thus, the blocks B will become finite dimensional with the dimension $4(2M_1 + 1)(2M_2 + 1)$. The determinant of the matrix $\tilde{\mathcal{M}}$ in (C2.41) will then be given by

$$\det \tilde{\mathcal{M}} \;=\; \prod_{q_0} \prod_{j_1,j_2=0}^{N_1,N_2} \det \mathcal{M}_{j_1 j_2}(q_0). \tag{C2.43}$$

By using $\ln \det \tilde{\mathcal{M}} = \mathrm{Tr} \ln \tilde{\mathcal{M}}$, the derivative of (C2.43) with respect to the mean surface distance H leads to

$$\partial_H \ln \det \tilde{\mathcal{M}} \;=\; L \int_{-\infty}^{\infty} \frac{dq_0}{2\pi} \sum_{j_1,j_2=0}^{N_1,N_2} \mathrm{tr} \left\{ \mathcal{M}^{-1}_{j_1 j_2}(q_0) \cdot \partial_H \mathcal{M}_{j_1 j_2}(q_0) \right\}, \tag{C2.44}$$

where the trace tr on the right hand side of Eq. (C2.44) is running over all discrete arguments at fixed j_1, j_2. Analogously to the discussion of the one dimensional case, we define the function

$$\begin{aligned} g(\mathbf{q}) \;&\equiv\; \mathrm{tr} \left\{ B^{-1}(\mathbf{q}) \cdot \partial_H B(\mathbf{q}) - B^{-1}_{\infty}(\mathbf{q}) \cdot \partial_H B_{\infty}(\mathbf{q}) \right\} \\ &= \sum_{k_1,l_1=-\infty}^{\infty} \sum_{k_2,l_2=-\infty}^{\infty} \sum_{\alpha,\beta,r,s=1}^{2} \Big\{ (B^{-1})^{\alpha\beta,rs}_{k_1 l_1, k_2 l_2} \cdot (\partial_H B)^{\beta\alpha,sr}_{l_1 k_1, l_2 k_2} \\ &\qquad\qquad - (B^{-1}_{\infty})^{\alpha\beta,rs}_{k_1 l_1, k_2 l_2} \cdot (\partial_H B_{\infty})^{\beta\alpha,sr}_{l_1 k_1, l_2 k_2} \Big\} (q_0; q_1, q_2). \end{aligned} \tag{C2.45}$$

Then, Eq. (C2.44) is recovered by

$$\begin{aligned} \partial_H \ln \det \left(\tilde{\mathcal{M}} \tilde{\mathcal{M}}^{-1}_{\infty} \right) \;&=\; L \int_{-\infty}^{\infty} \frac{dq_0}{2\pi} \sum_{j_1,j_2=0}^{N_1,N_2} g\left(q_0; \tfrac{2\pi j_1}{W_1}, \tfrac{2\pi j_2}{W_2} \right) \\ &\to LW^2 \int_{-\infty}^{\infty} \frac{dq_0}{2\pi} \int_0^{\frac{2\pi}{\lambda_1}} \frac{dq_1}{2\pi} \int_0^{\frac{2\pi}{\lambda_2}} \frac{dq_2}{2\pi}\, g(q_0; q_1, q_2). \end{aligned} \tag{C2.46}$$

In the last row of Eq. (C2.46), the continuum limit was performed. We note that g has the symmetry $g(q_0, q_1, q_2) = g(q_0, q_1 + 2\pi/\lambda_1, q_2 + 2\pi/\lambda_2)$, since B is of infinite dimension and therefore, a shift of the argument q_i by an integer multiple of $2\pi/\lambda_i$ will be absorbed.

3 Summary

In this chapter, we deduced a trace formula for the change of the Helmholtz spectrum by conducting surfaces of general shape. The derivation is based on a path integral quantization of the scalar field. While the discussion was focussed on the geometry composed of two plates S_α for $\alpha = 1, 2$, which is related to the Casimir problem, we note that the trace formula is sufficiently general to describe more general geometries including closed and disconnected objects, as depicted in Fig. C.1(b), see also the derivation in appendix F.1. For complicated geometries, an adapted regularization procedure has to be considered [9]. The formalism can also be extended to any space dimension, which might be interesting for applications to chaotic systems as classical or quantum billiards.

Focusing on the Casimir interaction, a non–approximative method to compute interactions in geometries with periodic structure and ideally conducting surfaces was developed in the second part of this chapter. The effective Gaussian action obtained from the path integral quantization was transformed to a representation which is adapted to periodic geometries. It was shown that the method can easily be extended to periodic geometries which can not be treated within the framework of a scalar field theory.

Path integral quantization in the presence of boundaries has been previously applied to perturbative calculations of Casimir interactions between static and dynamic deformed manifolds in the context of both thermal [71, 72] and quantum fluctuations [48, 49] of the confined field. However, these discussions were restricted to surfaces with small local curvature.

An efficient numerical computation of the force between macroscopic objects with *strong* periodic deformations can be performed based on the results obtained in this chapter. This will be done in the following chapter D, where special periodic geometries are taken into account, for which the matrix B in Eq. C2.26 can be obtained analytically.

D Casimir forces in periodic geometries

The Casimir interaction is strongly dependent on geometry. To date, the functional dependence of the interaction on changes of the geometry has been tried to be understood mainly by means of approximative methods. However, there is little knowledge about this dependence in geometries beyond some simple cases which are similar to the system of two flat plates, as e. g. plate and sphere. Not only inevitable surface roughness, but also and above all microstructures with artificial surface design require a treatment which goes further than the conventional approximative methods, which are restricted if the surface curvature becomes large or assume pair–wise additivity of intermolecular forces on microscopic scale.

This chapter is devoted to the study of the Casimir force in geometries which have periodically deformed surface structures. Specific geometries will be analysed, following up the general features which were outlined in chapters B, C, using the path integral technique. Periodic geometries were proposed to reveal more about the nature of the Casimir interaction [48, 35]. In Refs. [35, 36], sinusoidally corrugated surfaces are studied by means of perturbation theory to second order with respect to the deformation amplitude. This approximative method is reasonable as long as the deformation is smooth with low curvature, i. e. the deformation amplitude is the smallest length scale in the system. Otherwise, if the profile exhibits singularities as edges, perturbation theory to finite order yields divergent contributions to the interaction. This could only be repaired by smoothing out any sharp edge over a finite length scale, then sum up *all* orders of perturbation theory and *then* performing the limit to the profile with sharp edges again. This is evidently not practicable. Even for smooth profiles, a low order perturbation expansion will be insufficient if the curvature becomes large. Then, an expansion to higher orders is necessary to obtain reliable results. Thus we conclude that for arbitrary geometries, nonperturbative techniques become important.

In the first part of the chapter, we confine ourselves to the study of the normal Casimir force between a flat plate and a plate with periodic corrugation. We choose a uniaxial rectangular grating with edges for the corrugated mirror, see Fig. D.1. This profile is especially interesting because in fact it *demands* a nonperturbative analysis, because a perturbative analysis is *a priori* not applicable, due to the edges. The calculation of the Casimir interaction is an application of the general approach for uniaxial periodic geometries based on the scalar field quantization for ideal metals outlined in chapter B. Within this approach, the transversal magnetic (TM) and transversal electric (TE) waves of the electromagnetic field could be treated separately, and for the specific geometry considered here, they reveal a qualitatively distinct behaviour. We also compare the numerically obtained results to the proximity force approximation (PFA), which is equivalent to the renormalized pair–wise summation of Casimir–Polder potentials (PWS) if one of the plates is flat. The PFA assumes small local curvature, which is fulfilled for the flat segments of the rectangular grating, but violated near the edges where the curvature becomes infinitely large. While the deviation of the nonperturbative results from the PFA and PWS reflects the non–additivity of the Casimir force, the data scale towards the results of the PFA for large deformation wavelengths, where the density of edges along the axis of corrugation becomes small. In the opposite limit of small deformation wavelength, a different scaling is found, which is a non–perturbative effect. Furthermore, our numerical results will be compared to the perturbative results for the *sinusoidally* corrugated surface which were calculated in [35] and [36]. It will be seen that the profile with edges modifies the force compared to a smooth profile even at large distances.

Later in the second part, we will extend our study to lateral Casimir forces between two plates with rectangular gratings, see Fig. F.1. No lateral forces can exist in a geometry where one of the plates is flat, since there is no length scale which defines any lateral shift between the plates. As done in the case of the normal force, the results will be discussed and compared to those of the approximation methods.

1 Normal Casimir forces between periodically corrugated surfaces

The considered rectangular profile has amplitude a and corrugation wavelength λ and is opposed to a flat plate at a mean distance H, see Fig.D.1. Choosing y_1 to be the direction of modulation, the height profile function reads

$$h_1(y_1) = \begin{cases} a & \text{for} \quad |y_1| < \lambda/4 \\ -a & \text{for} \quad \lambda/4 < |y_1| < \lambda/2 \end{cases} \tag{D1.1}$$

with periodic continuation $h_1(y_1 + \lambda) = h_1(y_1)$. Since the upper plate is flat, $h_2(y_1) = 0$. To apply the general result of Eq. (C2.35) to the Casimir force, the matrix $\tilde{\mathcal{M}}$ needs to be decomposed into the coefficient matrices N_m of the expansion in Eq. (C2.24). For an arbitrary periodic profile, one needs to resort to a numerical evaluation of the matrices N_m. The periodicity of the profile of the lower plate permits its representation as a discrete Fourier

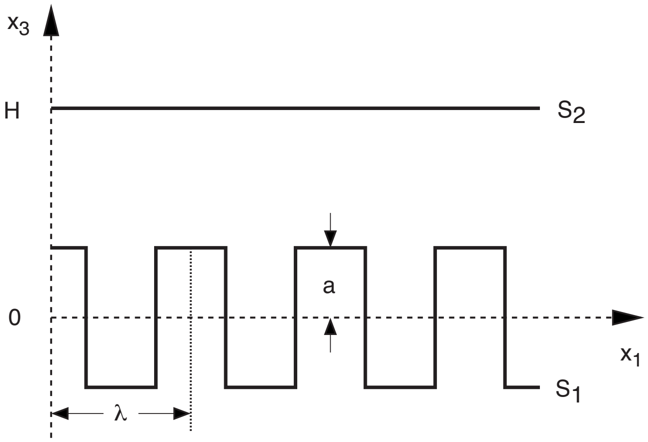

Figure D.1: Geometry consisting of a rectangularly corrugated plate and a flat plate. The surfaces are translationally invariant along the x_2–direction.

series,

$$h_1(y_1) \;=\; \frac{2a}{\pi} \sum_{n=-\infty}^{\infty} \frac{(-1)^{n-1}}{2n-1}\, e^{\frac{2\pi i}{\lambda}(2n-1)y_1}. \tag{D1.2}$$

Inserting this expansion (D1.2) into the matrix $\mathcal{M}$, cf. Eqs. (C2.19)–(C2.20), and calculating the Fourier transformed matrix $\tilde{\mathcal{M}}$ leads after some algebra to the matrices N_m. This calculation will be performed in appendix F in detail [1]. The results for Dirichlet boundary conditions are

$$N_{\mathsf{D},m}\left(q_\perp, q_1\right) \;=\; \begin{pmatrix} A^{\mathsf{D}}_m\left(q_\perp, q_1\right) & 0 \\ 0 & 0 \end{pmatrix} + \delta_{m0} \begin{pmatrix} \frac{1}{4q}(1+e^{-2aq}) & \frac{e^{-qH}}{2q}\cosh(aq) \\ \frac{e^{-qH}}{2q}\cosh(aq) & \frac{1}{2q} \end{pmatrix} \tag{D1.3}$$

if m is even, and

$$N_{\mathsf{D},m}\left(q_\perp, q_1\right) \;=\; \begin{pmatrix} 0 & \frac{(-1)^{\frac{m-1}{2}}}{m\pi}\frac{e^{-qH}}{q}\sinh(aq) \\ \frac{(-1)^{\frac{m-1}{2}}}{m\pi}\frac{e^{-\tilde{q}_m H}}{\tilde{q}_m}\sinh(a\tilde{q}_m) & 0 \end{pmatrix} \tag{D1.4}$$

if m is odd.

---

[1] In the appendix, *both* plates are corrugated and described by the function in Eq. (D1.2). From the resulting matrices, the matrices for the geometry in Fig. D.1 will be recovered by setting the amplitude of the second plate to zero.

Analogously, for Neumann boundary conditions, the results are

$$N_{\mathsf{N},m}\left(q_\perp,q_1\right) \;=\; \begin{pmatrix} A^{\mathsf{N}}_m\left(q_\perp,q_1\right) & 0 \\ 0 & 0 \end{pmatrix} + \delta_{m0} \begin{pmatrix} -\frac{q}{4}(1+e^{-2aq}) & \frac{q}{2}e^{-qH}\cosh(aq) \\ \frac{q}{2}e^{-qH}\cosh(aq) & -\frac{q}{2} \end{pmatrix} \tag{D1.5}$$

if m even, and

$$N_{\mathsf{N},m}\left(q_\perp,q_1\right) = \begin{pmatrix} 0 & \frac{(-1)^{\frac{m-1}{2}}}{m\pi}e^{-qH}\Big[q+\frac{2\pi m}{\lambda}\frac{q_1}{q}\Big]\sinh(aq) \\ \frac{(-1)^{\frac{m-1}{2}}}{m\pi}e^{-\tilde{q}_m H}\Big[\tilde{q}_m-\frac{2\pi m}{\lambda}\frac{q_1+2\pi m/\lambda}{\tilde{q}_m}\Big]\sinh(a\tilde{q}_m) & 0 \end{pmatrix} \tag{D1.6}$$

if m odd. The functions A^{D}_m and A^{N}_m are defined as follows:

$$A^{\mathsf{D}}_m\left(q_\perp,q_1\right) \;=\; \frac{1}{\pi^2}\sum_{k=-\infty}^{\infty}\frac{(-1)^{\frac{m}{2}}}{(2k-1)(m-2k+1)}\,\frac{e^{-2a\tilde{q}_{2k-1}}-1}{\tilde{q}_{2k-1}} \tag{D1.7}$$

and

$$A^{\mathsf{N}}_m\left(q_\perp,q_1\right) \;=\; \frac{1}{\pi^2}\sum_{k=-\infty}^{\infty}\frac{(-1)^{\frac{m}{2}}}{(2k-1)(m-2k+1)}\,\frac{1-e^{-2a\tilde{q}_{2k-1}}}{\tilde{q}^3_{2k-1}}\,\times \\ \times\,\Big[q_1\big(q_1+2\pi m/\lambda\big)\big(q_1+2\pi(2k-1)/\lambda\big)^2+2q_\perp^2\big(q_1+\pi m/\lambda\big)\big(q_1+2\pi(2k-1)/\lambda\big)+q_\perp^4\Big] \tag{D1.8}$$

respectively, with $\tilde{q}_n=(q_\perp^2+(q_1+2\pi n/\lambda)^2)^{1/2}$, which implies $q=\tilde{q}_0$. With these results, the Casimir force will be calculated by first constructing the matrix B_{kl} at finite truncation order M, cf. Eq. (C2.26). From this, the function $g_M(q_\perp,q_1)$ will be computed by inverting the matrix B numerically and multiplying with $\partial_H B$, cf. Eq. (C2.32). Finally, the integration will be performed, see Eq. (C2.35). This yields the force approximation F_M which converges to F for $M\to\infty$. For a sequence of fixed truncation orders M, we obtain a sequence F_M, which will be extrapolated to the force F.

In the limit of small corrugation wavelength, $\lambda\to 0$, it turns out that a closed form for the function $g(q_\perp,q_1)$ can be calculated, which allows to compute the Casimir force exactly.

1.1 Small corrugation wavelength

In the following, the case will be considered where the corrugation wavelength sets the smallest length scale in the system. In the limit of small corrugation wavelength $\lambda\to 0$, one would expect that the photon field modes of the zero point fluctuating field which mainly contribute to the interaction between the plates, which are those which have a wavelength of the order of the distance H, no longer enter into the narrow valleys of the corrugated plate. If λ is kept at a small but fixed value, this picture should be still a good, though approximate description, since it still affects the wavelengths of order H. Consequently, one expects that the plates interact with a force which is equal to a force between two *flat* plates at the *reduced* distance $H - a$. The question remains to what extent this approximation is applicable, how large is the correction if λ becomes larger, e. g. of order a. To verify the expectation of this "reduced distance argument" and to clarify the latter question, the previously developed approach will be applied to the case of $\lambda \to 0$. In this limit, the matrices $N_m(q_\perp, q_1)$ assume a particularly simple form for both TM and TE modes. Their explicit form is given in appendix F. From this result, the function $g_M(q_\perp, q_1)$ which was introduced earlier in chapter C before Eq. (C2.36), will be calculated analytically.

As pointed out previously, the infinite–dimensional matrix B_{kl} is truncated for the calculation at order M with $k, l = -M, \ldots, M$ so that the leading matrix entries are taken into account. From the exponential convergence behaviour of the result for flat plates given below Eq. (C2.37), one can expect that in the limit $\lambda \to 0$, the series $g_M(q_\perp, q_1)$ converges rapidly to $g(q_\perp, q_1)$. Our explicit calculation of $g_M(q_\perp, q_1)$ for low M confirms this expectation. From the truncated matrix B_{kl} of Eq. (C2.26) and the matrices in appendix F we get the result

$$g_M(q_\perp, q_1) \;=\; \begin{cases} -\frac{2q(1+e^{-2aq})}{1+e^{-2aq}-2e^{2(H-a)q}} & \text{for} \quad M=0 \\ q\left\{\coth\big(q(H-a)\big)-1\right\} & \text{for} \quad 1 \le M \le 3 \end{cases} \tag{D1.9}$$

for both TM and TE modes. From Eq. (D1.9) one sees that for orders $M \ge 1$ the function g_M remains invariant with increasing dimension M of the matrix B_{kl}. We have verified this *explicitly* for $M = 1, 2, 3$, it is plausible to assume the latter result to hold for all $M \ge 1$. The result has precisely the form which one gets for two flat plates at reduced distance $H - a$. Integrating the function g_M (for $M \ge 1$) according to Eq. (C2.35), one obtains the Casimir force per surface area for both types of modes

$$F_0/A \;=\; -\frac{\pi^2}{480}\frac{1}{(H-a)^4}. \tag{D1.10}$$

Thus, in the limit $\lambda \to 0$, TM and TE modes yield the same contribution F_0 to the total electrodynamic Casimir force $F = 2F_0$. The result of Eq. (D1.10) confirms the physical "reduced distance argument" introduced at the beginning of this paragraph. Note that this result is nonperturbative in a/H and exact in the limit $\lambda \to 0$. A perturbation expansion for smooth surface profiles yields always corrections of order a^2 [35, 36]. For small a/H, Eq. (D1.10) has the expansion

$$F_0/A \;=\; -\frac{\pi^2}{480}\frac{1}{H^4}\left[1 + 4a/H + \mathcal{O}(a^2/H^2)\right], \tag{D1.11}$$

where $a > 0$. In general, a has to be replaced by $|a|$. This shows that Eq. (D1.10) is non–analytic at $a \to 0$ and perturbation theory is not applicable for small $\lambda \ll |a|$.

Below in the numerical analysis it will be seen that F_0 is the upper limit of the Casimir force for both TM and TE modes for fixed H/a, i. e. with increasing λ the force decreases, starting from F_0. We expect the reduced distance argument to be valid for corrugations of arbitrary shape, if λ is identified with the characteristic length of surface deformations.

1.2 Large corrugation wavelength

In the opposite limit of very large λ, the corrugated surface is composed of large flat segments with a low density of edges. The main contribution to the force results from photon modes with wavelengths of the order of the distance H. Thus, at sufficiently small surface separation $H \ll \lambda$, diffraction can be neglected in the dominant range of modes, and the proximity force approximation (PFA) should be applicable.

The PFA assumes that the total force can be calculated as the sum of local forces between flat and parallel infinitesimally small surface elements at their local distance $H - h(y_1)$. It neglects diffraction which is strictly justified for smooth surfaces with small local curvature only. In the case discussed here, h_1 should be smooth with $a \ll \lambda$. While the latter condition is satisfied, the influence of the corners of the rectangular surface profile should decrease for $\lambda \to \infty$, such that the comparison of the exact result for the force with the result obtained by the PFA should be reasonable.

The pair–wise summation of renormalized Casimir–Polder potentials (PWS) and the PFA are identical for the case that one of the plates is flat, see Ref. [36]. The renormalization of the potential is performed such that the PWS for flat plates yields the exact result.

The PFA is applied in the limit $\lambda \to \infty$ by considering the flat segments of the surface profile h_1 as flat plates at the distances $H + a, H - a$ which are weighted each by one half across the entire surface area leading to for both TM or TE modes to the result

$$F_\infty/A = -\frac{\pi^2}{480}\frac{1}{2}\left[\frac{1}{(H-a)^4} + \frac{1}{(H+a)^4}\right]. \tag{D1.12}$$

In the next section, we will see that this result poses a lower limit to the Casimir force for both TM and TE modes. Expanding Eq. (D1.12) in orders of a/H, we get

$$F_\infty/A = -\frac{\pi^2}{480}\frac{1}{H^4}\left[1 + 10a^2/H^2 + \mathcal{O}(a^4/H^4)\right]. \tag{D1.13}$$

Since, due to the sum in the square brackets on the right hand side of Eq. (D1.12), the terms of odd powers cancel mutually in an expansion with respect to a/H, the correction for small a/H in the limit of large wavelength λ is of order $(a/H)^2$, contrary to the limit of small λ.

1.3 Exact results

In this section, the nonperturbative approach for periodic geometries outlined in chapter C will be implemented for the geometry depicted in Fig. D.1. This has to be done numerically, since the function g_M can not be computed analytically from the input matrices N_m in Eqs. (D1.3)–(D1.6) at arbitrary corrugation wavelength λ.

The basis for the numerical approach was outlined in the general discussion for periodic geometries. Note that the analytic knowledge of the input matrices N_m allows for an analytic evaluation of B_{kl} and its derivative with respect to H. This circumvents the risk of getting inaccurate results from numerical differentiation. Once the function g_M at finite truncation order is known, the integration in Eq. (C2.35) will be performed, which is straightforward due to the exponential decay of g_M. Thus, the force F_M is obtained, which converges to F in the limit $M \to \infty$.

From our analysis of the flat plate geometry in chapter C, see Eq. (C2.37), we expect an exponentially fast convergence of the finite size correction $F_M - F \sim e^{-\gamma M}$ with a coefficient γ, which depends on geometrical lengths. This will appear to be consistent with the numerical data, as discussed in more detail in the next section. It allows for an extrapolation of F from the F_M for $M \leq M_{\mathsf{max}}$. We chose M_{max} between 10 for the smallest $\lambda/a = 0.1$ and 97 at the largest value $\lambda/a = 300$.

The separate contributions F_{TM} and F_{TE} from TM and TE modes to the Casimir force were calculated in units of the corresponding forces $F_{\mathsf{T,flat}}$ for flat surfaces at the same (mean) distance H, where $\mathsf{T} = \mathsf{TM,TE}$. For flat plates, both forces are equal. We varied the mean surface distance H and the corrugation length λ both measured in units of the corrugation amplitude a. The results of the extrapolation of the data for F_M are displayed in Fig.D.2 as a function of H/a at different corrugation lengths λ/a ranging between 0.1 and 300. Additionally, in Fig.D.3, we show the results for the full force $F = F_{\mathsf{TM}} + F_{\mathsf{TE}}$ in an experimentally relevant range of small plate separations of up to $H/a = 16$. In the experiment of Chen and Mohideen [25], the ratio H/a is of this order. At any fixed distance, both types of modes are bounded from above by the result for the force F_0 at reduced distance, cf. Eq. (D1.10), and are bounded from below by F_∞, the result from the proximity force approximation, cf. Eq. (D1.12). For small λ/a the numerical data increase and approach F_0. For large λ/a, the data converge from above to the lower bound F_∞. Since the convergence towards F_∞ becomes slower for increasing H/a, there are two distinct scaling regimes for the force at fixed corrugation length λ/a.

At small H/a, the relative change of the force compared to the force between two flat plates $F_{\mathsf{T}}/F_{\mathsf{T,flat}} - 1$, decays as $(H/a)^{-2}$. After a crossover regime the relative change of the force

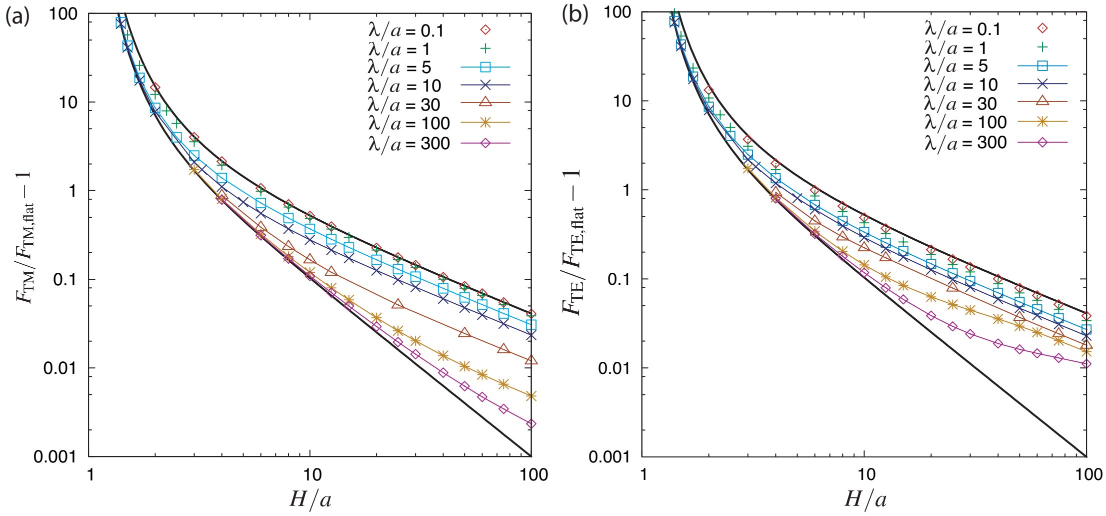

Figure D.2: Normal Casimir force for TM modes (a) and TE modes (b) as a function of H/a for various corrugation lengths λ. The (dimensionless) relative change compared to the force for flat plates $F_{\mathsf{TM,flat}} = F_{\mathsf{TE,flat}} = -\pi^2/(480H^4)$ is shown. The two bold curves which enclose the numerical data are the analytic results F_0 for $\lambda \to 0$ (upper curve) and F_∞ for $\lambda \to \infty$ (lower curve).

decays at larger $H \gg \lambda$ like $(H/a)^{-1}$, following the behaviour of the exact result F_0 for $\lambda \to 0$. The so far described qualitative behaviour of the force is common to both types of modes. However, there is a clear distinction between TM and TE modes, especially at large λ/a, as can be seen from Fig. D.2. The force from TE modes has much more pronounced deviation from the proximity approximation result F_∞ as the TM modes. In particular at large corrugation lengths ($\lambda/a = 300$) this can be seen clearly from our numerical data. The same behaviour is observed for the deviations from F_0 at small λ/a. Thus, the force F_{TE} appears at intermediate values of λ/a more strongly separated from the lower and upper bound, cf. Fig. D.2(b). We will return to this point later in the section when we discuss the scaling of the force with λ/a close to the bounds.

The differences between TM and TE modes seen above call for a quantitative study of the ratio of the two wave types. To set an example, it shall be mentioned that in some geometries such as a sphere or a cube, the Casimir energy for the full electromagnetic field leads to a *repulsive* force (which tends to extend the volumina), whereas the force obtained from a scalar field calculation with Dirichlet boundary conditions remains *attractive* [18, 90].

Since in uniaxial geometries such as the geometry we are looking at, the electromagnetic gauge field and the scalar field with Dirichlet boundary conditions differ in the presence of a

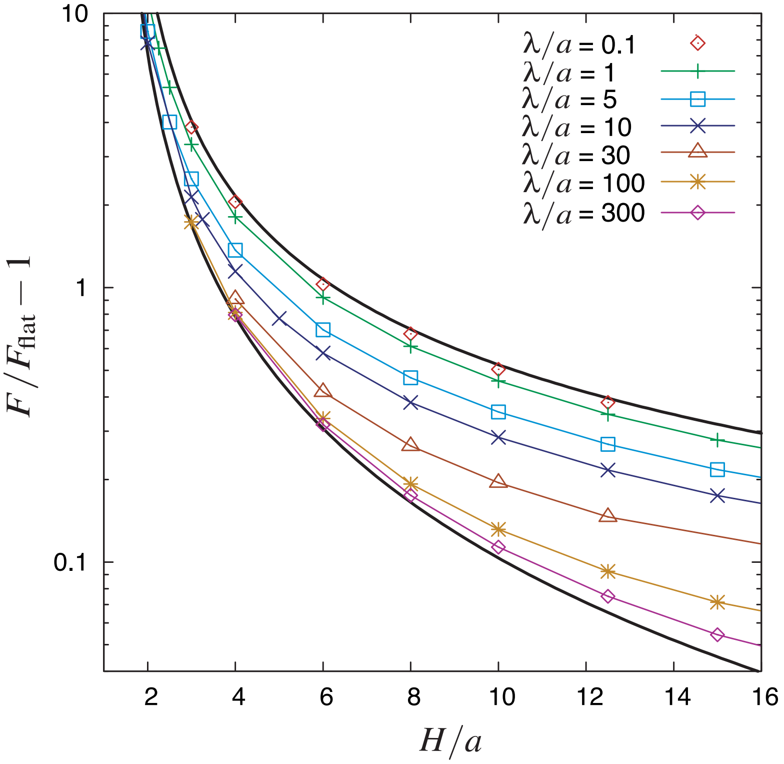

Figure D.3: Total Casimir force $F = F_{\text{TM}} + F_{\text{TE}}$ in the short distance regime. The relative change $\delta F = (F - F_{\text{flat}})/F_{\text{flat}}$ of the force compared to force for flat plates $F_{\text{flat}} = -\pi^2/(240H^4)$ is depicted. The enclosing curves have the same meaning as in Fig.D.2, but are now given by $2F_0$ and by $2F_\infty$ since both TM and TE modes have the same contribution in these limits.

scalar field with Neumann boundary conditions, i.e. TE waves, it is interesting to analyse the difference of the two wave types in more detail. This can be done by looking at the functional dependence of the ratio $F_{\text{TM}}/F_{\text{TE}}$ on the length scales of the geometry. Fig. D.4 shows this ratio as a function of the distance H/a. One observes that at fixed λ/a, in the limit of large surface distance, the ratio converges to 1, which is consistent with the fact that the geometry approaches that of two flat plates. Equally, in the limit of small $H/a \to 1$, the ratio $F_{\text{TM}}/F_{\text{TE}}$ approaches 1, which is in accordance with the proximity force approximation which does not distinguish between the two wave types. $F_{\text{TM}}/F_{\text{TE}}$ shows a peak for a characteristic H/a which depends on λ/a. For the entire range of studied corrugation lengths the ratio converges to one for large H/a according to $|F_{\text{TM}}/F_{\text{TE}} - 1| \sim (H/a)^{-1}$, see Fig. D.4(b). However, this asymptotic behaviour sets in only beyond a crossover separation H which increases with λ. At intermediate λ/a the ratio varies approximately between 0.95 and 1.15

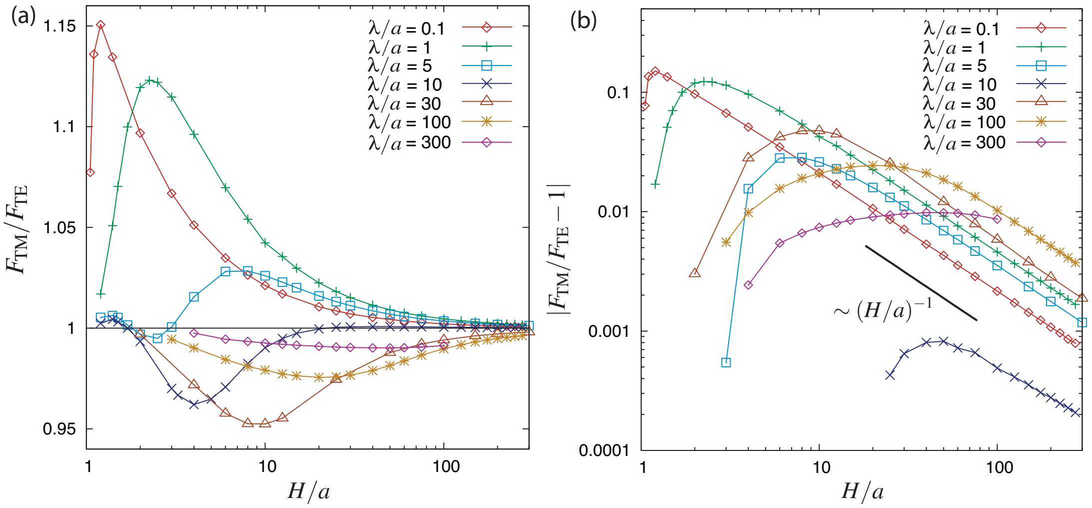

Figure D.4: (a) Ratio of the normal force for TM and TE modes as a function of the distance H for various corrugation wavelengths λ. (b) Log–log–plot of the deviation of the ratio from 1 at large surface distance H.

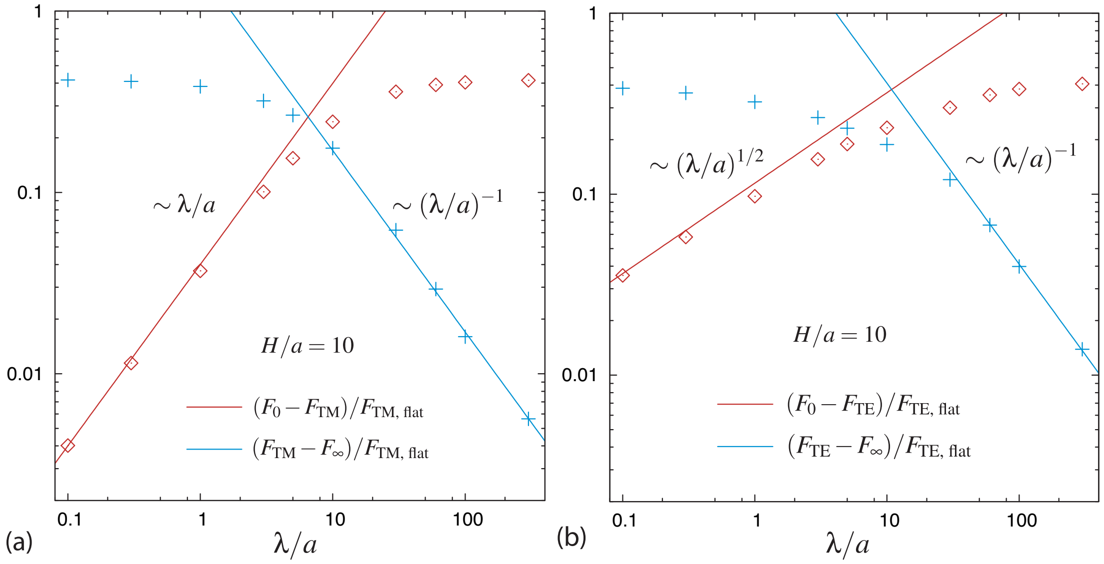

Figure D.5: Scaling behaviour of the force for TM modes (a) and TE modes (b) as a function of λ/a for fixed distance $H = 10a$ close to the lower bound (PFA) F_∞ for $\lambda \to \infty$ and to the upper bound F_0 for $\lambda \to 0$.

in the studied range of λ/a. TM modes dominate at $\lambda/a \lesssim 10$ and at small H/a for all λ/a. The contribution from TE waves is larger for $\lambda/a \gtrsim 10$ and $H/a \gtrsim 2$. It is instructive to

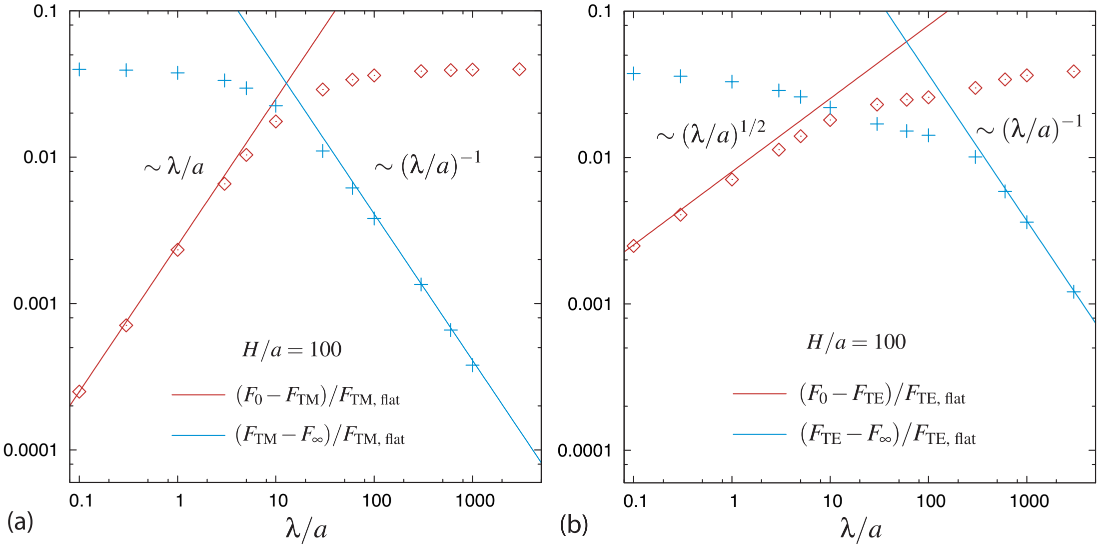

Figure D.6: This is the same plot as Fig. D.5 but for the surface distance $H = 100a$.

compare this behaviour to perturbative results of Ref. [35, 36] for the geometry consisting of a *smooth* sinusoidally corrugated and a flat plate. As will be explained in more detail in the next section, the perturbative result for the later geometry yields $F_{\text{TM}}/F_{\text{TE}} > 1$ for all $\lambda/a \gg 1$ and $H/a \gg 1$, in contrast to our results for the rectangular corrugation. This observation suggests that the corners of the rectangular corrugation in fact cause the slight amplification of TE waves compared to TM waves at $\lambda/a \gtrsim 10$. One can argue that imposing for TE modes a vanishing normal derivative on the field at the concave corners inside the valleys of the corrugation provides a stronger constraint on field fluctuations as compared to Dirichlet conditions for TM modes. If the width of the valleys is decreased with λ the two opposite corners can no longer be considered separately and the Dirichlet condition might provide a stronger restriction. For very small H/a the main contribution to the force comes from rather short wavelengths which should be only very weakly affected by the Neumann conditions at the concave corners. Finally, we consider the scaling of the force from TM and TE modes close to lower and upper bounds F_∞ and F_0, respectively. Figures D.5 and D.6 show a logarithmic plot of force form TM and TE modes at fixed $H = 10a$ and $H = 100a$, measured relative to F_∞ for large λ/a and relative to F_0 for small λ/a. At small λ we found an interesting qualitative difference between both types of modes for the scaling towards the exact result F_0 for $\lambda \to 0$,

$$\frac{F_0 - F_{\text{TM}}}{F_{\text{TM,flat}}} \sim \frac{\lambda}{a}, \qquad \frac{F_0 - F_{\text{TE}}}{F_{\text{TE,flat}}} \sim \left(\frac{\lambda}{a}\right)^{\frac{1}{2}}. \tag{D1.14}$$

For the difference of the exponents, we cannot present a satisfying simple argument.

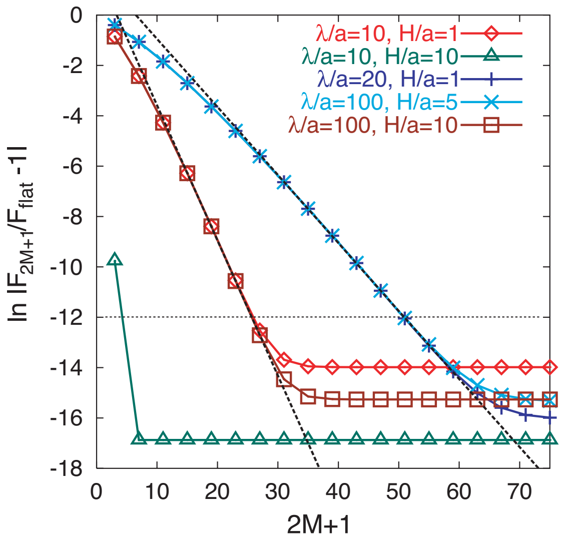

Figure D.7: Finite size scaling for flat plates. Displayed are $\ln|F_{2M+1}/F_{\text{flat}} - 1|$ as as function of $2M+1$ with the cutoff order M. The exponential decay does not set in immediately, it depends on the ratio H/λ and saturates due to the limited and previously defined precision of the algorithm. Note that λ has no physical meaning here, since the plates are flat. The same applies to the amplitude a relative in units of which the surface distance H is measured.

In the limit of large λ/a, the PFA result is approached linearly for both TM and TE modes.

$$\frac{F_{\text{TM}} - F_{\infty}}{F_{\text{TM,flat}}} \sim \frac{a}{\lambda}, \qquad \frac{F_{\text{TE}} - F_{\infty}}{F_{\text{TE,flat}}} \sim \frac{a}{\lambda}, \tag{D1.15}$$

which can be understood within the framework of classical ray optics [58] as we will discuss in section 1.5 of this chapter.

1.4 Numerical algorithm and finite size scaling

In this paragraph, the algorithm for the numerical computation of the Casimir force will be discussed in detail.

For the numerical calculation of the function g_M at finite cutoff order M, we used the so–called LU–decomposition and LU–backsubstitution, see [40], which is an efficient algorithm based on the Gaussian diagonalization procedure to determine the matrix $B^{-1}\partial_H B$ and then its trace from the (analytically calculated) matrices B and $\partial_H B$.

To obtain the force per surface area F_M/A according to Eq. (C2.35), the numeric integration of the obtained function g_M was performed for $q_1 \in [0, \pi/\lambda)$ and $q_\perp \in [0, \Lambda)$ with a cutoff

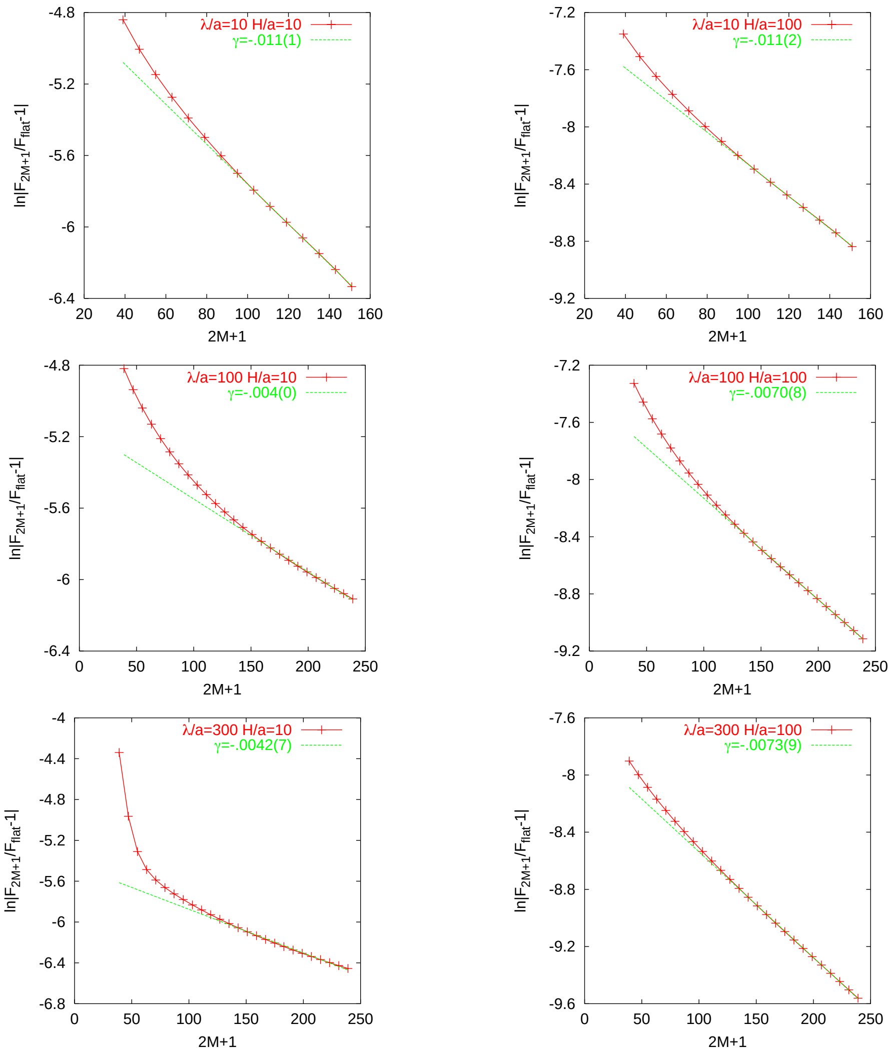

Figure D.8: Finite size scaling plots for TM modes for fixed values of the corrugation length λ and the distance H. Displayed are the logarithmic finite size corrections $\ln|1 - F_{2M+1}/F_{\text{flat}}|$ as a function of the cutoff order $2M+1$. The convergence is slower than for flat plates.

Λ, which is allowed due to the exponential decay of g_M in $q_\perp$. The matrices $N_m(q_\perp, q_1)$ depend exponentially on $q_\perp$, cf. Eqs. (D1.3)–(D1.6), and this exponential decay in $q_\perp$ translates to the function g_M. Note that this is consistent with the result for flat plates, cf. Eq. (C2.36). Moreover, the decay is *independent* of the cutoff order M. This can be compared to Eq. (C2.37) for the flat plate result, where M only enters in the integral over q_1. The cutoff Λ has to be chosen as large as to reach the saturating regime for F_M under a further increase of Λ. Since Λ does not depend on M, the cutoff Λ could be found by

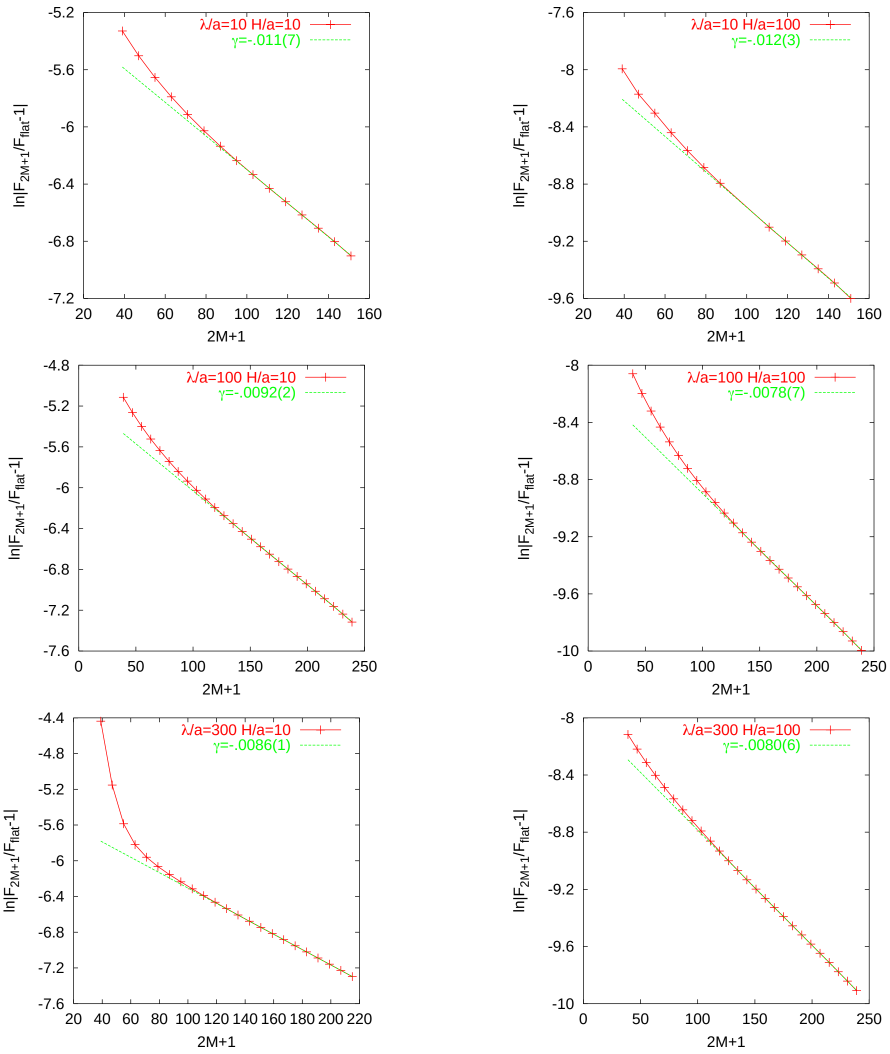

Figure D.9: The same plots as in D.8 for TE modes.

testing the function g_M at small orders of M.

The sampling points $(q_\perp, q_1) \in [0, \Lambda) \times [0, \pi/\lambda)$ were chosen dynamically by the integration routine DCUHRE [1] to satisfy the relative accuracy $\Delta F_M / F_M$ of the force which was set to 10^{-5}.

The calculations were performed with $\Lambda \geq 100/H$, which assures that the results for F_M after performing the integration are within the noise given by ΔF_M. Therefore, the limiting factor of precision is posed by the numerical integration, since the calculation of the function g_M via the LU–decomposition–backsubstitution procedure is a deterministic process with a precision which is only limited by double precision format of the data.

Finally, we discuss the extrapolation of F_M to F. As long as M is not large enough to reach the saturation regime, where for a fixed value F for the force $|F - F_M| \approx \Delta F_M$ for all $M \geq M_0$, the final result for the force has to be extrapolated.

Since the convergence is expected to be exponential, F is determined by the scaling assumption $F - F_M \sim e^{-\gamma M}$ with a coefficient γ which depends on geometrical lengths. We show the results as a function of $2M+1$. This modified cutoff counts the number of the 2×2 submatrices N_m in each row or column of B, which is always odd.

First, we test the exponential convergence for the case of flat plates. Fig. D.7 shows the logarithmic correction to the force $\ln |F_{2M+1}/F_{\mathsf{flat}} - 1|$ as a function of $2M+1$ with the finite cutoff order M for different values of λ and H. After a linear decay determined by γ, which depends only on the ratio of H/λ, the saturation regime is reached due to the limited precision of the integration routine. The precision is given by the point where the data deviate from the linear decay, which is $1 - F_{2M+1}/F_{\mathsf{flat}} \approx e^{-12} \approx 10^{-5}$.

In Figs. D.8–D.9, the exponential decay of the finite size corrections to the force for the corrugated plates for selected values $\lambda/a = 10, 100, 300$ of the wavelength and $H/a = 10, 100$ of the surface distance are shown. Note that the convergence for corrugated plates is much slower as in the case for flat plates, so that it can in general not be expected to reach the regime of saturation. We observe that for the corrugated plates, the decay exponent has no longer a simple dependence on the ratio H/λ, as in the case of flat plates. The data show an exponential decay as from a critical value of $2M+1$ between 80 and 120. The extrapolated value for the force F is obtained by a fit of the data F_M such that the exponential decay with the exponent γ is obeyed with a minimal error $\Delta\gamma$. The uncertainty of the extrapolated result is governed by the exponent $e^{-\Delta\gamma M_{\mathsf{max}}}$. We could estimate the force within a range of $\pm 5\%$ percent of accuracy, depending on the maximum value for the cutoff order M_{max}.

1.5 Comparison to approximative methods

In this section, we compare the numerical results for the square wave profile with the perturbatively obtained results for a sinusoidally shaped profile, see Ref. [36]. At the beginning of the present chapter, it was noted that the perturbation theory with respect to the deformation amplitude can generally not be performed for non–smooth surface deformations. We will see that perturbation theory yields divergences in the presence of sharp surface deformations as edges. For this reason, we compare the results of the numerical approach for the square wave profile with the perturbatively obtained results of a sinusoidally shaped profile discussed in Ref. [36]. We show that discrepancies in the results from the two approaches can be qualitatively understood in terms of classical ray optics, a concept which was used in Ref. [58] for the computation of Casimir interactions in non–trivial geometries.

Recall that the renormalized free Casimir energy is given by $\mathcal{E} = -(1/L)\ln\left(\mathcal{Z}\mathcal{Z}_\infty^{-1}\right)$, with the partition function $\mathcal{Z}$ and the Euclidean length L in time direction, cf. Eq. (B1.6) [2]. The logarithm of the partition function is additive, $\ln\mathcal{Z} = \ln\mathcal{Z}_{\mathsf{D}} + \ln\mathcal{Z}_{\mathsf{N}}$ with $\ln\mathcal{Z}_{\mathsf{D}}$ and $\ln\mathcal{Z}_{\mathsf{N}}$ the partition functions of TM modes (which satisfy Dirichlet boundary conditions) and TE modes (which satisfy Neumann boundary conditions), respectively, cf. Eqs. (B4.61)–(B4.62).

In Ref. [36], the logarithm of the partition function $\ln\mathcal{Z}$ is expanded in powers of the surface profiles h_α. From the fact that the surface profiles describe the deviation from the mean surface distance, one obtains that the *lowest* order correction to the energy of two flat plates $\mathcal{E}_0 = -\pi^2 A/720H^3$ is of *second* order in the height profile. The first order correction vanishes assuming that the spatial average of the height profiles is zero, $\int_{y_1} h_\alpha(y_1) = 0$. The second order correction can be expressed as $\mathcal{E}_2 = \mathcal{E}_{\mathsf{cf},1} + \mathcal{E}_{\mathsf{cf},2} + \mathcal{E}_{\mathsf{cc}}$. The term $\mathcal{E}_{\mathsf{cf},\alpha}$ contains the second order correction to the energy which results from the deformation function h_α while the other plate is kept flat. Correlations of the surface deformations are captured by the other term $\mathcal{E}_{\mathsf{cc}}$. Following Ref. [36], the terms are given by

$$\begin{aligned}
\mathcal{E}_{\mathsf{cf},\alpha} &= -\frac{\pi^2}{120LH^5}\sum_\alpha \int d^3y\, h_\alpha(y_1)^2 \\
&\quad + \frac{1}{4L}\sum_\alpha \int d^3y \int d^3y'\, K\left(\mathbf{y}-\mathbf{y}'\right)\left(h_\alpha(y_1) - h_\alpha(y_1')\right)^2, \qquad \text{(D1.16)} \\
\mathcal{E}_{\mathsf{cc}} &= \frac{1}{2L}\sum_{\alpha\neq\beta} \int d^3y \int d^3y'\, Q\left(\mathbf{y}-\mathbf{y}'\right)\; h_\alpha(y_1)h_\beta(y_1'). \qquad \text{(D1.17)}
\end{aligned}$$

The integrations are taken over the three dimensional space defined by $\mathbf{y} = (y_0, y_1, y_2)$. The K and Q are response kernels which contain separate contributions from TM and TE modes. Note that $\mathcal{E}_2$ contains further formally infinite contributions, which, however, are singled out by regularizing the energy, which is done by subtracting the contributions for $H \to \infty$.

The second plate is flat in the geometry considered here, i.e. $h_2 = 0$, see Fig. D.1. Thus, the total energy to second order in perturbation theory reduces to $\mathcal{E} = \mathcal{E}_0 + \mathcal{E}_{\mathsf{cf},1}$. Inserting now the Fourier series Eq. (D1.2) for the rectangular height profile h_1 into Eq. (D1.16), the energy per surface area can be transformed into

$$\frac{\mathcal{E}}{A} = \frac{\mathcal{E}_0}{A} - \frac{a^2\pi^2}{120H^5} + 2\pi a^2 \int_0^\infty dy\, y^2 K_{\mathsf{D}}\left(y\right) + 2\pi a^2 \int_0^\infty dy_0 \int_0^\infty dy_\parallel\, y_\parallel K_{\mathsf{N}}\left(y_0, y_\parallel\right). \qquad \text{(D1.18)}$$

The kernel for the Dirichlet boundary condition depends only on $y = |\mathbf{y}|$ and is explicitly

---

[2] In Eq. (B1.6), the Euclidean length in time direction L is given by the inverse temperature β (for $T > 0$).

given by

$$K_{\mathsf{D}}\,(y) \;=\; -\frac{1}{2\pi^4 y^8}+\frac{\pi^2}{128 H^6 y^2}\,\frac{\cosh^2(s)}{\sinh^6(s)}, \tag{D1.19}$$

with $s=\frac{\pi y}{2H}$. The kernel K_{N} for the Neumann boundary condition assumes a more complicated form because the normal derivative breaks the equivalence of space and time directions. Therefore, it depends on y_0 and on $y_{\|}=|\mathbf{y}_{\|}|$ separately, see Ref. [36]. The integrals in Eq. (D1.18) diverge at $y\to 0$. However, for any *smooth* profile, one obtains to lowest order $[h_1(y_1)-h_1(y_1+y_1')]^2\sim y_1'^2$, and the second term on the left hand side of Eq. (D1.16) becomes regular.

We consider a sinusoidal profile with amplitude a_0 and corrugation wavelength λ given by $h_1(y_1)=a_0\cos(2\pi y_1/\lambda)$, see Fig. D.10(a), to compare with the rectangular geometry with amplitude a. For the sinusoidal profile, Eq. (D1.16) yields for the sum of TM and TE modes together with zero order term $\mathcal{E}_0$ the perturbative correction to the force

$$F/F_{\mathsf{flat}} \;=\; 1+\widetilde{G}\left(\frac{H}{\lambda}\right)\left(\frac{a_0}{H}\right)^2 \;+\;\mathcal{O}\left(a_0^3\right), \tag{D1.20}$$

with the function parameter free $\widetilde{G}(x)\equiv(480/\pi^2)\big(G(x)-u\,G'(x)\big)$, where $G=G_{\mathsf{TM}}+G_{\mathsf{TE}}$ is the sum of its contributions from TM and TE modes, the explicit forms of which are calculated in Ref. [36] and given by

$$\begin{aligned} G_{\mathsf{TM}}(x) \;=\;& \frac{\pi^3 x}{480}-\frac{\pi^2 x^4}{30}\ln(1-e^{-4\pi x})+\frac{\pi}{1920x}\mathrm{Li}_2\left(1-e^{-4\pi x}\right)+\frac{\pi x^3}{24}\mathrm{Li}_2\left(e^{-4\pi x}\right)\\ &+\frac{x^2}{24}\mathrm{Li}_3\left(e^{-4\pi x}\right)+\frac{x}{32\pi}\mathrm{Li}_4\left(e^{-4\pi x}\right)+\frac{1}{64\pi^2}\mathrm{Li}_5\left(e^{-4\pi x}\right)\\ &+\frac{1}{256\pi^3 x}\left[\mathrm{Li}_6\left(e^{-4\pi x}\right)-\frac{\pi^6}{945}\right], \end{aligned} \tag{D1.21}$$

$$\begin{aligned} G_{\mathsf{TE}}(x) \;=\;& \frac{\pi^3 x}{1440}-\frac{\pi^2 x^4}{30}\ln(1-e^{-4\pi x})+\frac{\pi}{1920x}\mathrm{Li}_2\left(1-e^{-4\pi x}\right)\\ &-\frac{\pi x}{48}\left(1+2x^2\right)\mathrm{Li}_2\left(e^{-4\pi x}\right)+\left[\frac{x^2}{48}-\frac{1}{64}\right]\mathrm{Li}_3\left(e^{-4\pi x}\right)\\ &+\frac{5x}{64\pi}\mathrm{Li}_4\left(e^{-4\pi x}\right)+\frac{7}{128\pi^2}\mathrm{Li}_5\left(e^{-4\pi x}\right)\\ &+\frac{1}{256\pi^3 x}\left[\frac{7}{2}\mathrm{Li}_6\left(e^{-4\pi x}\right)-\pi^2\mathrm{Li}_4\left(e^{-4\pi x}\right)+\frac{\pi^6}{135}\right], \end{aligned} \tag{D1.22}$$

with the polylogarithmic function $\mathrm{Li}_n(z)=\sum_{k=1}^{\infty} z^k/k^n$ [37].

Here, for the purpose of comparison, we are interested in the asymptotic limits of large and

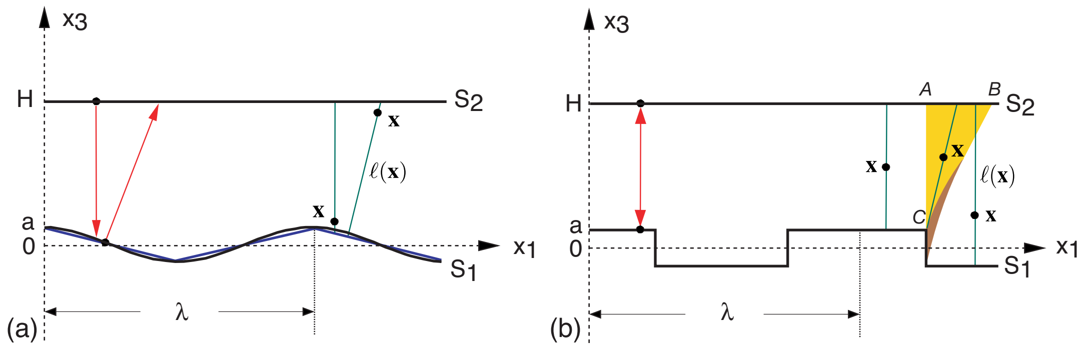

Figure D.10: Paths of the proximity force approximation (PFA) and the geometric optics approach for both sinusoidal (a) and rectangular corrugation (b) with $a \ll \lambda$. The arrows denote the paths of the PFA, which are measured normal to one of the surfaces. The lines without arrows represent the shortest path of length $\ell(\mathbf{x})$ through a given point $\mathbf{x}$ in the vacuum gap between the plates.

small H/λ. Expanding $\widetilde{G}$ for these limits yields for Eq. (D1.20)

$$\frac{F}{F_{\text{flat}}} - 1 = \begin{cases} \dfrac{8\pi}{3}\dfrac{a_0}{H}\dfrac{a_0}{\lambda} & \text{for} \quad \lambda \ll H \\ 5\left(\dfrac{a_0}{H}\right)^2 + \left(\dfrac{4\pi^2}{3} - 20\right)\left(\dfrac{a_0}{\lambda}\right)^2 & \text{for} \quad \lambda \gg H \end{cases} . \tag{D1.23}$$

In both limits the results are valid only if $a_0 \ll \lambda$. In the limit of small λ/a_0 there is a divergence $\sim a_0/\lambda$ in the perturbative result which reflects the above mentioned divergence in Eq. (D1.18) for rectangular corrugations with vertical segments. This singularity does not appear in our numerical results of the previous section; it is a characteristic feature of perturbation theory. In the following comparison we consider only the case $\lambda \gg a_0$. Eq. (D1.23) suggests for large plate separations $H \gg \lambda$ a decay of the excess force from the corrugation $\sim a_0/H$ and for small H/λ a decay $\sim (a_0/H)^2$. The scaling behaviour is in agreement with our observations for the rectangular corrugation as demonstrated by Fig. D.2. However, the latter Figure also shows that for smaller $\lambda/a \lesssim 10$ the scaling regime with a decay $\sim (a/H)^2$ does not exist.

Next, the perturbative result in Eq. (D1.23) will be compared with the numerical results for the derivation of the actual Casimir force from the proximity–force approximation (PFA), $(F - F_{\text{PFA}})/F_{\text{flat}}$. Since the PFA does not distinguish between TM and TE modes, $F_{\text{PFA}} = 2F_\infty$ where F_∞ is given by Eq. (D1.12). In general, The PFA is not uniquely definable and thus can lead to ambiguous results. Since in the PFA, the plates are assumed to be locally flat, and the distance between the surfaces is measured perpendicular to the surface elements, the measured distances will depend on the choice of the surface relative to which the distance is measured. This is indicated by the arrows in Fig. D.10(a). Note that this ambiguity does not arise for the square wave geometry, see Fig. D.10(b). For smooth surfaces with finite curvature as the sinusoidally shaped corrugation, the results of the PFA thus depend on the reference plate. If the reference plate is flat,the Casimir energy of the PFA is

$$\mathcal{E}_{\mathsf{PFA}} = \frac{1}{A}\int_{S_2} dS\, \mathcal{E}_0\big(H - h_1(x_1)\big), \tag{D1.24}$$

with $\mathcal{E}_0(H)$ being the energy for flat plates at distance H. Taking the corrugated plate as the reference plate, the result, however, is

$$\mathcal{E}_{\mathsf{PFA}} = \frac{1}{A}\int_{S_1} dS\, \mathcal{E}_0\left[\big(H - h_1(x_1)\big)\left(1 + [h_1'(x_1)]^2\right)^{1/2}\right]. \tag{D1.25}$$

For a smooth corrugation, the integrals in the expressions (D1.24), (D1.25) can be expanded in powers of the amplitude a_0. This yields for large corrugation wavelengths λ the difference between the force F from perturbation theory, Eq.(D1.23), and F_{PFA}, based on the flat and the corrugated plate, respectively,

$$\frac{F_{\mathsf{pt}} - F_{\mathsf{PFA}}}{F_{\mathsf{flat}}} = \begin{cases} \left(\dfrac{4\pi^2}{3} - 20\right)\left(\dfrac{a_0}{\lambda}\right)^2 & \text{for the flat plate as reference plate} \\ \left(\dfrac{10\pi^2}{3} - 20\right)\left(\dfrac{a_0}{\lambda}\right)^2 & \text{for the corrugated plate as reference plate} \end{cases}. \tag{D1.26}$$

The key result is the decay $\sim (a_0/\lambda)^2$ for large λ, which has to be compared to the a/λ decay seen in the numerical results for the square wave profile, see Figs. D.5, D.6. Thus, the deviation from the PFA is stronger for the rectangular profile than for the sinusoidal profile, presumably due to the edges. Before giving a simple physical argument for the variation of the decay exponent, we discuss the different amplitudes in Eq. (D1.26). While the PFA based on the corrugated plate yields a positive amplitude, the amplitude of the flat plate based PFA is negative and thus, the force F_{PFA} is not a lower bound to the force at fixed H/a, contrary to the numerical results for the rectangular profile. The observation that the Casimir force is located between the results of the flat and the curved surface based PFA was also made for a plane–sphere geometry [46].

Recently, classical ray optics has been applied to improve upon the PFA for the calculation of Casimir forces [58]. This concept does not account for diffraction and thus works strictly only if the radii of curvature are large compared to the surface distance. However, it yields a simple picture for the distinct scaling behaviour for the sinusoidal and square wave geometry at large wavelengths λ. Thus, even in the presence of edges, geometric optics provides a better description than the PFA. Instead of considering all optical paths in the vacuum gap between the surfaces, the idea is to select for each point $\mathbf{x}$ the shortest ray between the surfaces through that point, the length of which is denoted by $\ell(\mathbf{x})$, see Fig. D.10. The Casimir energy from the optical approximation can be written as

$$\frac{\mathcal{E}_{\text{opt}}}{\mathcal{E}_{\text{flat}}} = \int d^2\mathbf{x}_\parallel \int_{h_1(x_1)}^{H} dx_3 \, \frac{H^3}{A\ell^4(\mathbf{x}_\parallel, x_3)}, \tag{D1.27}$$

where the integral runs over the vacuum gap between the surfaces.

First, we apply Eq. (D1.27) to the sinusoidal profile, cf. Fig. D.10(a). For small amplitudes $a_0 \ll \lambda$ as considered here, the sinusoidal profile can be replaced in good approximation by a piecewise linear profile. Then, for each point $\mathbf{x}$ between the plates, $\ell(\mathbf{x})$ is to be determined for this simpler profile. Since an exact determination of $\ell(\mathbf{x})$ is rather complicated, we consider the situation where the point $\mathbf{x}$ is close to one of the surfaces and then assume for arbitrary $\mathbf{x}$ a linear interpolation between the two situations, see right part of Fig. D.10(a). If $\mathbf{x}$ is close to the deformed surface S_1, the shortest path is perpendicular to the flat surface S_2, and vice versa. With the so obtained approximative lengths $\ell(\mathbf{x})$, one obtains from Eq. (D1.27) by expansion in a_0/H for the correction to the flat surface based PFA the scaling

$$\frac{F_{\text{opt}} - F_\infty}{F_{\text{flat}}} \sim \left(\frac{a_0}{\lambda}\right)^2 \tag{D1.28}$$

which reproduces the scaling of the corrections to the PFA at large λ, in agreement with the result (D1.23) from perturbation theory.

In order to examine the influence of edges on the deviations from the PFA, the optical approach will also be applied to the rectangular corrugation in Fig. D.10(b). Except for small domains with almost triangular cross section along the x_1–axis, the shortest paths for the positions $\mathbf{x}$ are perpendicular to both surfaces. Therefore, the deviations from the PFA can only result from paths through points in the shaded domains. These paths end either at the corner C for points in the larger (light shaded) domain, or at the vertical segment of the corrugated surface for those points which are located in the smaller (dark shaded) domain. If λ is sufficiently large, the domains belonging to adjacent edges of the corrugated plate do not overlap and can be treated independently. Moreover, since the ratio of the area of the cross section of the larger domain, represented by the triangle ABC, with the area of the cross section of the smaller domain scales like $\sim (H/a)^2$, it suffices to consider the larger domain for the evaluation of Eq. (D1.27) in the asymptotic limit $a \ll H$. The result is

$$\frac{F_{\text{opt}} - F_\infty}{F_{\text{flat}}} \sim \frac{a}{\lambda}\sqrt{\frac{a}{H}}, \tag{D1.29}$$

which is consistent with the observed scaling behaviour of the numerical data for the rectangular profile, cf. Figs. D.5,D.6 and Eq. (D1.15). We conclude that the analysis of the *shortest* optical paths explains the dependence of the Casimir force on the surface shape close to the proximity force limit for $\lambda \gg H$.

Furthermore, the ratio of the contributions from TM and TE modes to the force which is obtained from the perturbative expansion for the sinusoidal profile in Eq. (D1.20) will be discussed. To low order in a_0, the result is given by

$$\frac{F_{\text{TM}}}{F_{\text{TE}}} = 1 + \frac{8\pi}{3}\frac{a_0}{\lambda}\frac{a_0}{H}, \tag{D1.30}$$

which holds if $a_0 \ll \lambda \ll H$. Thus for sinusoidal corrugations the force has always larger contributions from TM modes at asymptotically large H, in contrast to our numerical results for rectangular corrugations, cf. Fig. D.4(a). We argued in the previous section that edges might cause the amplification of TE mode contributions. However, the convergence of the ratio to one for large H turns out be insensitive to the shape of the corrugations. Our numerical results agree perfectly over the full range of studied λ/a with perturbation theory in that the ratio decays like a/H to one, see Fig. D.4(b). For small $\lambda/a \to 0$ the amplitude in no longer given by Eq. (D1.30) but saturates at a finite value which decreases with λ since for $\lambda \to 0$ the reduced distance argument of section 1.1 implies equal contributions from both types of modes.

2 Lateral Casimir forces between periodically corrugated surfaces

Chen and Mohideen measured the lateral Casimir force between a sinusoidally corrugated plate and a sphere with large radius and with imprinted sinusoidal corrugation [25] at surface distances between 0.2μm and 0.3μm using an atomic force microscope. In correspondence

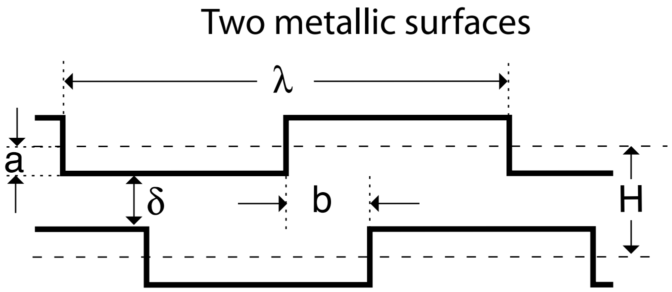

Figure D.11: Geometry with two corrugated plates. b is the lateral shift between the plates.

to that experiment, Emig and co–workers calculated the lateral force perturbatively between two sinusoidally corrugated surfaces [36]. The lateral Casimir force tends to align the plates such that the maxima of the surface profiles are opposed to each other [25]. From this we expect that for the periodic geometry depicted in Fig. D.11, the force has a stable equilibrium position at $b = \lambda/2$ and an unstable equilibrium position at $b = 0$. For a periodic profile, the force is necessarily periodic as well. If one plate is flat, as in the geometry we considered for the study of the normal Casimir force, there is no length scale which defines a lateral shift between the plates relative to each other and no lateral force exists.

We follow the development in Ref. [36] analogously and study the lateral force between two corrugated plates. Our aim is to test the non–perturbative algorithm for periodic surfaces developed in chapter C also for the lateral force, which is especially sensitive to changes of the geometry since it is determined by the interaction of the surface corrugations of both plates. On the other hand, it is interesting to analyse how the lateral force is modified due to the edges in the geometry, since it was seen that edges lead to non–perturbative effects of the *normal* Casimir force. The key results of this paragraph will be that the lateral force exhibits an universal behaviour in the large distance limit. Furthermore, perturbation theory provides a good approximation for small deformation amplitudes *independently* of the presence of edges, which is in striking contrast to the results for the normal force.

We consider the geometry of two periodically deformed plates with edges, cf. Fig. D.11. The corrugation of the plates is assumed to have equal amplitude a and the plates are laterally shifted to each other, which is expressed by the relation $h_2(y_1) = h_1(y_1 + b)$, with the height profile h_1 given by Eq. (D1.1). The length b is the parameter which describes the relative lateral shift between the plates. The lateral Casimir force is obtained by taking the derivative of the free energy with respect to this shift, $F_{\text{lat}} = -\partial_b \mathcal{E}$.

The height profiles h_α have the Fourier series expansion

$$\begin{aligned} h_\alpha(y_1) &= \frac{2a}{\pi} \sum_{n=-\infty}^{\infty} \frac{(-1)^{n-1}}{2n-1} \, e^{\frac{2\pi i}{\lambda}(2n-1)(y_1+\delta_{\alpha 2} b)} \\ &= \frac{4a}{\pi} \sum_{m=1}^{\infty} \frac{(-1)^{m-1}}{2m-1} \cos\left[2\pi(2m-1)(y_1 + \delta_{\alpha 2} b)/\lambda\right]. \end{aligned} \tag{D2.31}$$

The procedure is now similar to that for the normal force. Given the matrices N_m, which are calculated explicitly in appendix F yields the matrix B_{kl} at fixed truncation order M. This gives the function

$$g_M = \operatorname{tr}\left\{B^{-1}\partial_b B - B_\infty^{-1}\partial_b B_\infty\right\} \tag{D2.32}$$

cf. Eq. (C2.32), with the truncated trace tr over the discrete indices $\alpha, \beta = 1, 2$ and $k, l = -M, \ldots, M$. Note that, contrary to the case where the derivative is taken with respect to the surface distance H, the term $B_\infty^{-1}\partial_b B_\infty$ does not vanish automatically and must be subtracted *explicitly* to regularize the function g_M. Thus, the calculation of the lateral force is at the same time a critical test of our numerical algorithm, since the regularization must be implemented explicitly.

The function g_M must be real, since its integral yields the force. However, due to the parametrization of the h_α, the matrices N_m are complex, leading thus to a B with complex entries, too. In order to take the real part, we use

$$\mathrm{Re}\,(B^{-1}\partial_b B) = \mathrm{Re}\,(B^{-1})\,\partial_b \mathrm{Re}\,B - \mathrm{Im}\,(B^{-1})\,\partial_b \mathrm{Im}\,B. \tag{D2.33}$$

with the real and imaginary parts of the inverse

$$\begin{aligned} \mathrm{Re}\,(B^{-1}) &= [(\mathrm{Re}\,B) + (\mathrm{Im}\,B)(\mathrm{Re}\,B)^{-1}(\mathrm{Im}\,B)]^{-1}, && \text{(D2.34)} \\ \mathrm{Im}\,(B^{-1}) &= -(\mathrm{Re}\,B)^{-1}(\mathrm{Im}\,B)\mathrm{Re}\,(B^{-1}). && \text{(D2.35)} \end{aligned}$$

The same applies to the matrix B_∞. Taking these identities as an input to calculate g_M numerically, the lateral force is obtained by a numerical integration according to Eq. (C2.35).

At short corrugation wavelengths, the amplitude of the lateral force falls off to 0. This is consistent with the fact that in the limit $\lambda \to 0$, the geometry approaches two flat plates where no lateral force exists any longer. This can be interpreted as a "reduced distance argument" for the lateral force. However, contrary to the case for the geometry with one flat plate, the matrices N_m assume no particularly simple form in the limit $\lambda \to 0$ for arbitrary b, so that we have no independent analytical test for this limit and one has to resort to the numerical treatment. In the opposite limit, where the deformation wavelength becomes the largest length scale in the system, i. e. for $\lambda \to \infty$, for both height profiles h_1 and h_2, the density of edges along the y_1–axis tends to zero. Recall that in the prior discussion for the normal force, we used this fact to apply the proximity–approximation. Although this approximation is strictly applicable only if the surface curvature is finite and small, we found that this limit is well described by the PFA for flat plates at the two distances weighted each one half. For this reason, we expect that it is reasonable to apply the proximity force approximation also for the lateral force. For the geometry in Fig. D.11, there are three different distances, and the weight factors depend on the shift b. The proximity approximation to the force is given by

$$\begin{aligned} F_{\mathsf{PFA}} &= -\partial_b \mathcal{E}_{\mathsf{PFA}} = -\frac{1}{\lambda}\,\partial_b \int_0^\lambda dy_1\, \mathcal{E}_0\big(H + h_2(y_1) - h_1(y_1)\big) \\ &= \frac{1}{\lambda}\big(2\mathcal{E}_0(H) - \mathcal{E}_0(H-2a) - \mathcal{E}_0(H+2a)\big) \end{aligned} \tag{D2.36}$$

for $0 < b < \lambda/2$ with the Casimir energy $\mathcal{E}_0$ for flat plates. At $b = \lambda/2$, F_{PFA} changes sign, so that the profile of the force reproduces the profile of the surfaces within this approximation. The expansion of Eq. (D2.36) in the corrugation amplitude a for $a \ll H$ yields

$$F_{\mathsf{PFA}} = \frac{\pi^2}{15}\frac{a^2 A}{\lambda H^5} + \mathcal{O}(a^4). \tag{D2.37}$$

The higher order corrections $\mathcal{O}(a^4)$ in Eq. (D2.37) are $\simeq 5.1\%$ of the exact result in Eq. (D2.36) for $H/a = 10$ and below $5 \cdot 10^{-3}\%$ for $H/a = 100$. Note that at fixed distance H, F_{PFA} is linear as a function of H/λ for *both* Eq. (D2.36) and Eq. (D2.37).

The numerical computations will show that the PFA becomes exact in the limit $\lambda/H \gg 1$, as it is expected from the results obtained for the normal force. In contrast to the normal force, we will see that the PFA is an *upper* bound to the lateral Casimir force.

We also compare our findings to the PWS approximation, which is strictly justified only in the limit of dilute media due to its additivity assumption. The PWS accounts for non–additivity by renormalizing the Casimir–Polder potential so that the PWS yields the known result in the limit of flat plates, cf. [14]. For the conducing surfaces, the renormalized retarded pair potential is given by $U(r) = (\pi/24)\hbar c/r^7$, see also [36]. We can expect the PWS approximation to hold for $\lambda/H \gg 1$, which will be confirmed by the numerical results. However, there is little intuition about its results for intermediate values $\lambda \approx H$. Recall that the PWS is identical to the proximity–approximation if one plate is flat [36]. Here, this is no longer the case. The Casimir energy in the PWS approximation is given by

$$\mathcal{E}_{\mathsf{PWS}} = \int_{V_+} d^3\mathbf{y} \int_{V_-} d^3\mathbf{y}'\, U\big(|\mathbf{y}-\mathbf{y}'|\big)\,, \tag{D2.38}$$

where the volumes $V_\pm$ are the exterior regions beyond the plates which enclose the vacuum gap. In terms of the height profiles h_α, Eq. (D2.38) assumes the form

$$\mathcal{E}_{\mathsf{PWS}} = \int d^2\mathbf{y}_\parallel \int d^2\mathbf{y}'_\parallel \int_{H+h_2(y_1)}^{\infty} dz \int_{-\infty}^{h_1(y_1)} dz'\, U\left(\sqrt{(\mathbf{y}_\parallel - \mathbf{y}'_\parallel)^2 + (z-z')^2}\right). \tag{D2.39}$$

To calculate F_{PWS} from Eq. (D2.39), the derivative with respect to b is taken analytically and then, the remaining integrals are computed numerically.

2.1 Perturbation theory for the lateral force

In the previous discussion of the normal Casimir force for the geometry depicted in Fig. D.1, we concluded that the edges in the profile lead to non–perturbative effects. It was observed that the perturbation theory leads to divergent results due to the edges of the profile. The divergence could be attributed to the pole of the kernel $K(\mathbf{y})$ for $|\mathbf{y}| \to 0$, cf. Eq. (D1.16). Note that for the lateral interaction between two corrugated surfaces, the term

$$\mathcal{E}_{\mathsf{cc}} = \frac{1}{L} \int d^3y \int d^3y' \, Q\left(\mathbf{y} - \mathbf{y}'\right) \, h_1(y_1) h_2(y_1'), \tag{D2.40}$$

cf. Eq. (D1.17), contributes to the energy, since both $h_1, h_2 \neq 0$. Contrary to the response kernel K, the kernel Q is regular for $|\mathbf{y}| \to 0$. Therefore, the integral expression in Eq. (D2.40) has no divergences and is well defined. Furthermore, since $\mathcal{E}_{\mathsf{cc}}$ is the only term of the second order approximation to the energy which depends on the lateral shift b between the plates, the lateral force will be given by $F_{\mathsf{lat}} = -\partial_b \mathcal{E}_{\mathsf{cc}}$. Therefore, we expect that for small deformation amplitude a, the lateral Casimir force can be captured by perturbation theory, which is a qualitatively different behaviour compared to the normal force. Inserting the Fourier expansion Eq. (D2.31) into Eq. (D2.40) and using $h_2(y_1) = h_1(y_1 + b)$ gives

$$\mathcal{E}_{\mathsf{cc}} = \frac{4a^2 A}{\pi^2} \sum_{n=-\infty}^{\infty} \frac{e^{2\pi i(2n-1)b/\lambda}}{(2n-1)^2} \int d^3y \, Q\left(\mathbf{y}\right) \, e^{2\pi i(2n-1)y_1/\lambda}. \tag{D2.41}$$

Before proceeding, we consider the *sinusoidally* shaped surface profile $h_1(y_1) = a_0 \cos(2\pi y_1/\lambda)$. In Ref. [36], the perturbative expansion of this profile led to the result

$$\mathcal{E}_{\mathsf{cc}} = \frac{a_0^2 A}{H^5} \cos\left(\frac{2\pi b}{\lambda}\right) J\big(H/\lambda\big) + \mathcal{O}(a_0^3), \tag{D2.42}$$

with an amplitude function J, which has separate contributions from TM and TE modes, $J = J_{\mathsf{TM}} + J_{\mathsf{TE}}$. Those are given by

$$J_{\mathsf{TM}}(x) = \frac{\pi^2}{32} \int_0^\infty ds \, \frac{\sin(4xs)}{4xs} \frac{\sinh^2(s)}{\cosh^6(s)}, \tag{D2.43}$$

and $J_{\mathsf{TE}}(x) = j_1(x) - x^2 j_2(x) + x^4 j_3(x)$, with

$$j_1(x) = \frac{\pi^2}{32} \int_0^\infty ds \, \frac{\sin(4xs)}{4xs} \frac{\sinh^2(s)}{\cosh^6(s)} \left[\frac{5}{2} - \sinh^2(s)\right], \tag{D2.44}$$

$$j_2(x) = \frac{\pi^2}{4} \int_0^\infty ds \, \frac{\sin(4xs)}{4xs} \frac{\sinh^2(s)}{\cosh^4(s)}, \tag{D2.45}$$

$$j_3(x) = \frac{\pi^2}{2} \int_0^\infty ds \, \frac{\sin(4xs)}{4xs} \frac{\sinh^2(s)}{\cosh^2(s)}. \tag{D2.46}$$

Furthermore, an explicit calculation of the separate contributions from Dirichlet and Neumann boundary conditions to the kernel Q in Ref. [36] was made.

The Dirichlet kernel

$$Q_{\mathsf{D}}(y) = \frac{\pi^2}{128}\frac{1}{H^6 y^2}\frac{\sinh^2(s)}{\cosh^6(s)} \tag{D2.47}$$

depends only on $y = |\mathbf{y}|$, and $s = \pi y/(2H)$. The Neumann kernel has not the full rotational symmetry as the Dirichlet response kernel, since the normal derivative appears in the Neumann boundary condition. It assumes the form

$$Q_{\mathsf{N}}\left(|y_0|, |\mathbf{y}_\parallel|\right) = \left(\partial_z^2 g(y,H) + \mathcal{F}_6(y)\right)\mathcal{F}_4(y) + \mathcal{F}_2(y)^2 - \partial_1^2\left(\mathcal{F}_4 \cdot \mathcal{F}_2\right)(y) + \frac{1}{8}\,\partial_1^4\left(\mathcal{F}_4^2\right)(y), \tag{D2.48}$$

with the functions

$$\mathcal{F}_2(y) = -\frac{\pi}{16H^3 y}\frac{\sinh(s)}{\cosh^3(s)}, \tag{D2.49}$$

$$\mathcal{F}_4(y) = \frac{1}{4\pi H y}\frac{\sinh(s)}{\cosh(s)}, \tag{D2.50}$$

$$\mathcal{F}_6(y) = -\partial_z^2 g(y,H) + \frac{\pi^3}{16H^5 y}\frac{\sinh(s)}{\cosh^5(s)}\left[1 - \frac{1}{2}\sinh^2(s)\right], \tag{D2.51}$$

and with the second derivative of the Green function $g(p,z) \equiv \partial_z^2 \mathcal{G}(p,z) = \frac{p}{2}\,e^{-p|z|}$ which reads in position space

$$g(y,z) = \int \frac{d^3\mathbf{p}}{(2\pi)^3}\, e^{i\mathbf{p}\cdot\mathbf{y}}\, g(p,z). \tag{D2.52}$$

Considering the expressions above, we insert the Dirichlet and Neumann kernels $Q_{\mathsf{D}}, Q_{\mathsf{N}}$ into the integral on the right hand side of Eq. (D2.41). The Neumann kernel can be brought into rotational symmetric form by integration by parts. Then, we get

$$\int d^3y\, Q\left(\mathbf{y}\right)\, e^{2\pi i(2n-1)y_1/\lambda} = \frac{2}{H^5}\, J\big(|2n-1|H/\lambda\big). \tag{D2.53}$$

Thus, the energy assumes the form

$$\mathcal{E}_{\mathsf{cc}} = \frac{16a^2}{\pi^2}\frac{A}{H^5}\sum_{n=1}^{\infty}\frac{\cos\big(2\pi(2n-1)b/\lambda\big)}{(2n-1)^2}\, J\big((2n-1)H/\lambda\big). \tag{D2.54}$$

This expression for the energy constitutes the main result of this section. The function J can be calculated explicitly from the integral expressions Eqs. (D2.43)–(D2.46) by contour

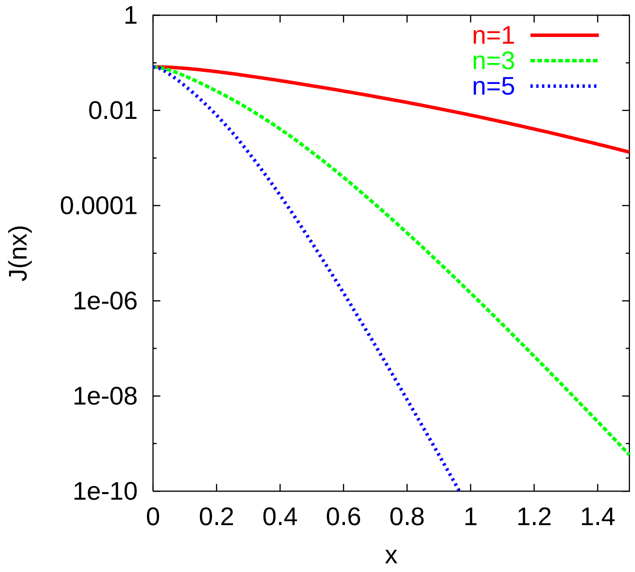

Figure D.12: Semilogarithmic plot of the function $J(nx)$ for odd $n = 1, 3, 5$. For large arguments, the function decays exponentially.

integration in the complex plane, which is performed in Ref. [36]. The result is given by

$$\begin{aligned} J_{\mathsf{TM}}(x) &= \frac{\pi^2}{120}(16x^4-1)\,\mathrm{artanh}(e^{-2\pi x}) + e^{-2\pi x}\left[\frac{\pi}{12}\left(x^3-\frac{1}{80x}\right)\Phi(e^{-4\pi x},2)\right. \\ &\quad + \frac{x^2}{12}\Phi(e^{-4\pi x},3) + \frac{x}{16\pi}\Phi(e^{-4\pi x},4) + \frac{1}{32\pi^2}\Phi(e^{-4\pi x},5) \\ &\quad \left. + \frac{1}{128\pi^3 x}\Phi(e^{-4\pi x},6)\right], \end{aligned} \tag{D2.55}$$

$$\begin{aligned} J_{\mathsf{TE}}(x) &= \frac{\pi^2}{120}(16x^4-1)\,\mathrm{artanh}(e^{-2\pi x}) + e^{-2\pi x}\left[-\frac{\pi}{12}\left(x^3+\frac{x}{2}+\frac{1}{80x}\right)\Phi(e^{-4\pi x},2)\right. \\ &\quad + \frac{1}{24}\left(x^2-\frac{3}{4}\right)\Phi(e^{-4\pi x},3) + \frac{5}{32\pi}\left(x-\frac{1}{20x}\right)\Phi(e^{-4\pi x},4) \\ &\quad \left. + \frac{7}{64\pi^2}\Phi(e^{-4\pi x},5) + \frac{7}{256\pi^3 x}\Phi(e^{-4\pi x},6)\right]. \end{aligned} \tag{D2.56}$$

In Eqs. (D2.55), (D2.56) the Lerch trancendent $\Phi(z,k) = \sum_{n=0}^{\infty} \frac{z^n}{(\frac{1}{2}+n)^k}$ is used, cf. Ref. [37]. Here, we are interested in the asymptotic behaviour of J for large and small arguments,

$$J(x) = \frac{4\pi^2}{15}\left\{x^4+\mathcal{O}(x^2)\right\}e^{-2\pi x} \qquad \text{for} \quad x \gg 1, \tag{D2.57}$$

$$J(x) = \frac{\pi^2}{120} + \mathcal{O}(x) \qquad \text{for} \quad x \ll 1. \tag{D2.58}$$

For large arguments, J will be dominated by its exponential decay. This can be seen in Fig. D.12, where the decay of $J(nx)$ as a function of x is shown for $n = 1, 3, 5$. Note that for $H \gtrsim \lambda$, Eq. (D2.54) is dominated by the term for $n = 1$,

$$\mathcal{E}_{\text{cc}} = \frac{16a^2}{\pi^2}\frac{A}{H^5}\cos\left(\frac{2\pi b}{\lambda}\right) J\big(H/\lambda\big) + \mathcal{O}\left(n > 1\right). \tag{D2.59}$$

Eq. (D2.59) is consistent with Eq. (D2.42) for $a_0 = 4a/\pi$. Since this a_0 is the amplitude of the first harmonic of the square wave profile, cf. Eq. (D2.31), the lateral force at large distance is governed by the large scale surface structure described by the first harmonic. Since this property is generic for periodic surfaces, we note that the regime $H \gg \lambda$ is *asymptotically universal* regarding changes of the short scale surface structure. Eq. (D2.59) yields the force

$$F_{\text{pt}} = \frac{32a^2}{\pi}\frac{A}{\lambda H^5}\sin\left(\frac{2\pi b}{\lambda}\right) J\big(H/\lambda\big) \overset{H\gg\lambda}{\rightarrow} \frac{128\pi}{15}\frac{a^2 A}{\lambda^5 H}\sin\left(\frac{2\pi b}{\lambda}\right) e^{-2\pi H/\lambda}. \tag{D2.60}$$

There are evidences that this universal behaviour of the lateral force is independent of the range of validity of perturbation theory, i.e. it holds also if the deformation amplitude a becomes large. We will come back to this point in the next section, where the exact results obtained from our numerical algorithm are discussed.

If the deformation wavelength λ becomes larger, the higher harmonics of the series in Eq. (D2.54) are no longer negligible. Then, the series can be cut off at $n \gtrsim \lambda/H$, where the argument of J is still at the order of 1, cf. Fig. D.12. In the extreme limit for $\lambda \to \infty$ at fixed distance H, all terms of the (convergent) series contribute, since J becomes constant, cf. Eq. (D2.58), and Eq. (D2.54) can be simplified to

$$\mathcal{E}_{\text{cc}} = \frac{16a^2}{\pi^2}\frac{A}{H^5} J\big(0\big)\sum_{n=1}^{\infty}\frac{\cos\left(2\pi(2n-1)b/\lambda\right)}{(2n-1)^2} = \frac{a^2 A\pi}{30H^5}\left(\frac{\pi}{2} - \frac{2\pi}{\lambda}|b|\right). \tag{D2.61}$$

The latter equality in Eq. (D2.61) holds for $|b| \leq \lambda/2$ with periodic continuation for integer multiples of λ. Hence, one gets for the lateral Casimir force for $0 < b < \lambda/2$,

$$F_{\text{lat}} = -\partial_b \mathcal{E}_{\text{cc}} = \frac{a^2\pi^2 A}{15\lambda H^5}. \tag{D2.62}$$

Note that the force changes sign at $b = \lambda/2$. Eq. (D2.62) is the second order expansion of F_{PFA}, cf. Eq. (D2.37). Thus, the validity of the PFA, which is expected from the results for the normal Casimir force for $H \ll \lambda$, is confirmed by perturbation theory, where $a \ll H$ is assumed.

For general values of H/λ, the lateral force is obtained from Eq. (D2.54) as

$$F_{\mathsf{lat}} = \frac{32a^2}{\pi}\frac{A}{\lambda H^5}\sum_{n=1}^{\infty}\frac{\sin\big(2\pi(2n-1)b/\lambda\big)}{2n-1}\,J\big((2n-1)H/\lambda\big). \qquad \text{(D2.63)}$$

From Eq. (D2.63) we observe that the perturbative approximation to the lateral force is periodic as a function of the lateral shift b, which confirms our expectations. Moreover, it is symmetric around $b = \lambda/4$ for $|b| < \lambda/2$. Especially, at $b = \lambda/4$, where the maximum for the force is expected, one gets, using $x = H/\lambda$,

$$F_{\mathsf{lat}} = \frac{32a^2}{\pi}\frac{A}{\lambda H^6}\,x\big\{J(x) - \frac{1}{3}J(3x) + \frac{1}{5}\,J(5x) \pm \ldots\big\}. \qquad \text{(D2.64)}$$

For large x, the force will be dominated by the exponential decay of the lowest order term $J(x)$, cf. Eq. (D2.57). For small $x \to 0$, the term in curly brackets will approach the value of $\pi^3/480$, and the force will become linear in x at fixed distance H, which is in accordance with the result for the proximity–force value.

2.2 Exact results

In this section, we implement the non–perturbative approach for periodic geometries outlined in chapter C for the geometry depicted in Fig. F.1. to calculate the lateral Casimir force.

This has to be done numerically, since the function g_M can not be computed analytically from the input matrices N_m which are listed in full generality in appendix F. The approach is analogous to that for the normal force with the distinction that the derivative is taken with respect to the shift b. Once the function g_M at finite truncation order is known, the integration in Eq. (C2.35) will be performed.

Thus, the force F_M is obtained, which converges exponentially to F in the limit $M \to \infty$, which appears to be consistent with the numerical data, as discussed in more detail in the next section. It allows for an extrapolation of F from the F_M for $M \leq M_{\mathsf{max}}$. For the calculation of the lateral force, the cutoff order M was chosen between 10 and 37. The numerical process is more complicated for the evaluation of the lateral force, since the real and imaginary parts of the matrix B have to be computed, cf. Eq. (D2.33), which requires the inversion of two matrices consecutively, cf. Eq. (D2.34). We calculated the force for TM modes and TE modes separately, but we constrict the discussion to the total Casimir force which is the sum of the separate contributions for both types of modes, $F = F_{\mathsf{TM}} + F_{\mathsf{TE}}$.

The numerical data reveal three different regimes, which are depicted in the diagram in Fig. D.13(a). It shows the approximate validity ranges of the PFA and the PWS approximation methods, which become reliable for small H/λ, when the surfaces are composed of large,

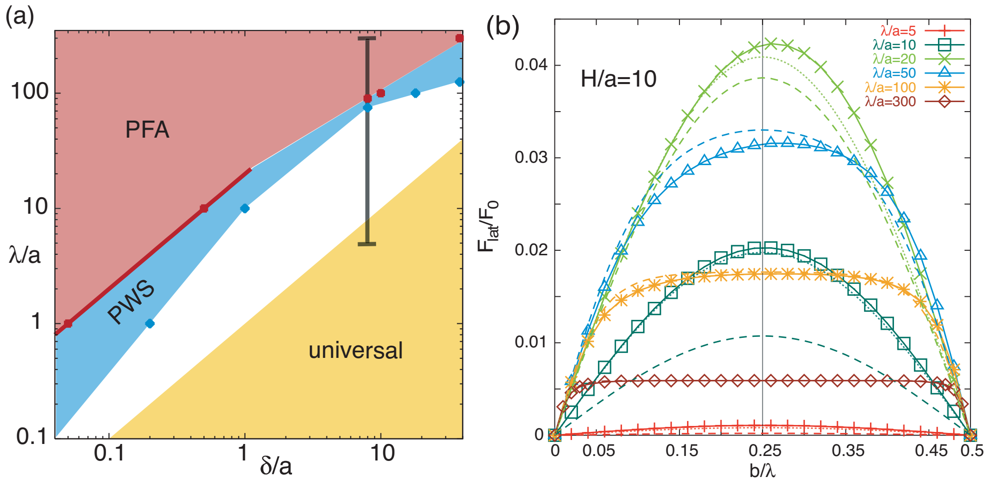

Figure D.13: (a) Approximate ranges of validity of the proximity force and PWS approximations and the sector of asymptotic universality for the lateral Casimir force as estimated from Fig. D.14. The vertical bar shows the range of corrugation wavelengths $5a \leq \lambda \leq 300a$ at fixed plate distance $H = 10a$, for which the shape dependence of the force with b was analysed, see (b).

flat segments and when the density of edges of the profile along the axis of corrugation is small. The PWS exhibits a slightly amplified validity range compared to the proximity–force approximation (PFA).

For larger $H \simeq \lambda$, both PFA and PWS become unreliable. In this regime, the lateral force can only be studied numerically or perturbatively if $a \ll \lambda, H$, as pointed out in section 2.1.

For large $H \gg \lambda$, we have seen from the results of perturbation theory that the lateral force decreases exponentially fast to zero and we observed that the force becomes asymptotically universal in the sense that it approaches the lateral force between *sinusoidally* shaped surface profiles with equal corrugation wavelength λ and amplitude $a_0 = 4a/\pi$. Since the latter profiles are the first harmonic of the Fourier expansion of the profile with edges, cf. Eq. (D2.31), we conclude that the short scale surface structure, which is described by higher harmonics of the height profile, see Eq. (D2.31), is irrelevant for the interaction at large distances. This asymptotically universal behaviour is consistent with the numerical data for the force which is indicated by the lower triangular region in Fig. D.13(a). The perturbative approximation to which the numerical data for the force are compared at large distances reads, cf. Eq. (D2.60) with $a_0 = 4a/\pi$,

$$F_{\text{pt}} = 2\pi \frac{a_0^2 A}{\lambda H^5} \sin\left(\frac{2\pi b}{\lambda}\right) J\left(H/\lambda\right). \tag{D2.65}$$

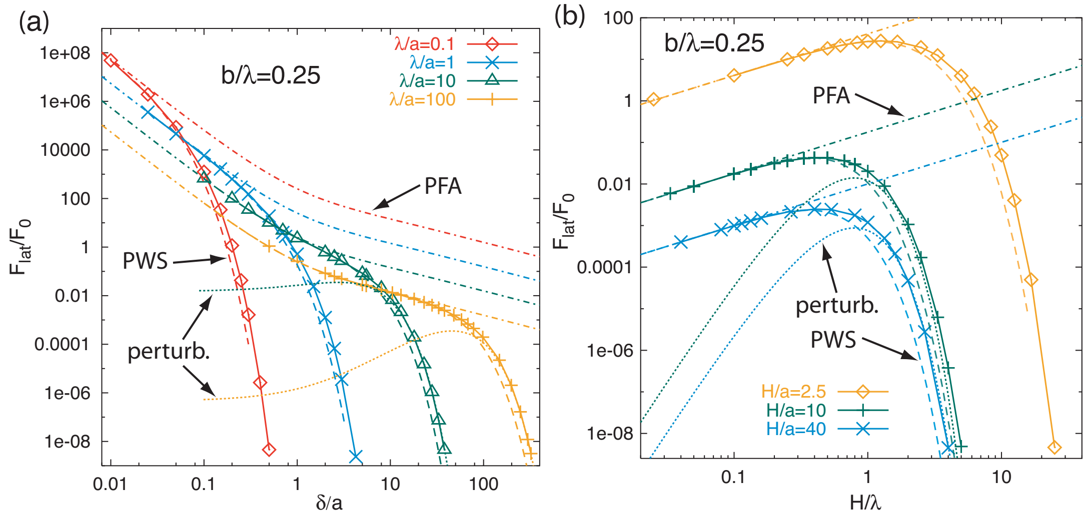

Figure D.14: (a) Lateral force F_{lat} at $b = \lambda/4$ for the geometry of Fig. D.11 depending on the reduced distance $\delta = H - 2a$ (solid curves). F_{lat} is measured in units of the normal force $F_0 = \pi^2/240H^4$. The proximity force (PFA, dashed-dotted lines) and pair-wise summation (PWS, dashed lines) and the perturbative result F_{pt} for sinusoidal profiles at large distance (dotted lines) are displayed. (b): Dependence of the lateral force on the ratio H/λ for fixed H (solid curved). Shown are also the results from PFA, PWS, and F_{lat}.

At fixed distance $H = 10a$, Fig. D.13(b) exhibits the dependence of the force on the lateral shift b in the interval between 0 and $\lambda/2$ for various values of λ, as indicated by the vertical bar in the diagram D.13(a). The data for the force are given in units of the normal force F_0 for flat plates at distance H. At first, we note that the force vanishes at $b = 0, \lambda/2$ and becomes maximal close to $b = \lambda/4$, which is consistent with our expectations. Varying λ in the range between $5a$ and $300a$, the transition between the three regimes displayed in Fig. D.13(a) can be observed. At large $\lambda \geq 100a$, the numerical data approach to the results from the PWS which are displayed as dashed curves. For $\lambda \geq 300a$, the data and the PWS result are in good agreement, and the force profile approaches the rectangular shape of the height profile and assumes a constant value, as expected from the PFA. This value scales with λ^{-1}, cf. Eq. (D2.36).

In the intermediate regime given by the data for $\lambda = 20a, 50a$, the force amplitude increases and the dependence on b becomes more peaked. Note that the force becomes asymmetric, since the maximum is assumed at $b_{\text{max}} = \lambda/4 + \Delta b$, where we observe the larger Δb around $\lambda/a = 50$. This asymmetry is neither reproduced by perturbation theory nor by the PWS.

Fig. D.13(b) shows that the maximal amplitude of force can be found in the range around $\lambda = 20a$.

For further decreasing λ, represented by the data curves for $\lambda = 5a$ and $\lambda = 10a$, the regime of universality is approached, the asymmetry in b decreases, and the force profile tends to a sinusoidal form. For $\lambda/a = 5, 10, 20$ we included the perturbative result of Eq. (D2.65) into Fig. D.13(b), represented by the dotted lines. The best agreement between the perturbative result and the data is obtained for $\lambda = 10a$. However, the numerical data show still a slight asymmetry of the exact result. For $\lambda = 5a$, the numerical data exhibit the best agreement with a sinusoidal function $\sim \sin(2\pi b/\lambda)$. However, the amplitude of the force shows a stronger deviation from the perturbative result than in the case for $\lambda = 10a$. This can be expected since the deformation amplitude a is already large compared to λ for the applicability of perturbation theory, which assumes $a \ll \lambda$. The sinusoidal shape of the exact result for the force indicates that the force at large distances is universal, it no longer depends on the short scale surface structure described by the higher harmonics of the height profile, independently of the ratio λ/a. However, a strict proof of this requires for a numerical computation of the lateral force for the sinusoidal profile at arbitrary λ/a.

Note that also the PWS result assumes a sinusoidal shape dependence, but the amplitude is about $1/2$ of the numerical result for $\lambda = 10a$ and even smaller for $\lambda = 5a$ which shows the failure of the pair–wise additivity assumption in strongly non–planar geometries.

As seen above, the maximum of the lateral force as a function of b is assumed close to $b = \lambda/4$. Therefore, Fig. D.14(a) displays the data for the force at $b = \lambda/4$ as a function of the reduced distance $\delta = H - 2a$ in units of the normal force F_0 for flat plates at distance H. The results from the PWS and the PFA are represented by dotted and dashed–dotted curves, respectively. For distances beyond $\delta \approx \lambda/20$, the PFA starts to fail, since it does not capture the exponential decay with increasing δ. In contrast, the PWS–approximation to the force reproduces the exponential decay. However, for increasing distances beyond $\delta \approx 2\lambda$, the deviation of the PWS from the numerical data is about *one* order of magnitude. The perturbative results of Eq. (D2.65) is represented by dotted curves for $\lambda = 10a$ and $\lambda = 100a$. In contrast to Fig. D.13(c), we used the asymptotic expression $J(x) = (4\pi^2/15)(H/\lambda)^4\, e^{-2\pi H/\lambda}$ for large H/λ, cf. Eq. (D2.57), for Fig. D.14. While the similarity of the perturbative results with the numerical data for the general J at $b = \lambda/4$ suggests a good coincidence in general (which is not the case if the dependence on b is taken into account, see Fig. D.13), the use of the asymptotic expression is a better indication in Fig. D.14 for the asymptotically universal regime, where the exact result for the force also assumes a sinusoidal shape as a function of the shift b.

We find a good agreement (within the precision of the numerical data) between the perturbative approximation to the force for the first harmonic of the rectangular profile with the numerical data for this profile for distances $\delta \geq \lambda$. This shows that the force becomes universal. However, in the regime $\lambda \leq a$ beyond the range of validity of perturbation theory, represented by the data for $\lambda = 0.1a$ and $\lambda = a$ in Fig. D.14, there is no independent (analytical) result to which the numerical data can be compared.

The dependence of the lateral force on H/λ at fixed distances $H/a = 2.5, 10, 40$ is represented in Fig. D.14(b). The force increases linearly for small H/λ in accordance with the PFA (dashed–dotted curve). For larger H/λ, it exhibits a maximum and then it decays exponentially, as the PWS. The PWS becomes unreliable beyond the maximum. Displayed are also the asymptotic results from perturbation theory for $H/a = 10, 40$. Note the agreement of the perturbative with the numerical results at large H/λ for $H = 40a$. For $H = 10a$, the perturbative result starts to fail at larger $H/\lambda \gtrsim 2.5$. The position of the maximum at $\lambda \approx 2.5H$ for $H/a = 10, 40$ is in agreement with the findings in Ref. [36]. For $H/a = 2.5$, the maximum is shifted towards smaller wavelengths.

2.3 Numerical algorithm

The algorithm for the computation of the lateral force is a modified version of the algorithm used before to calculate the normal force such that the arguments concerning the choice of the integral cutoff, the precision, and extrapolation apply here in the same form. The difference lays in the calculation of the function g_M for any finite cutoff order M. Here, the LU–decomposition–backsubstitution procedure to perform the matrix inversion is to be applied twice to perform the inversion of the complex valued matrix B, see Eq. (D2.34), to get the product $B^{-1}\partial_b B$. The same procedure is to be performed for the asymptotic matrices B_∞, because the regularization must be implemented explicitly. Otherwise, since $B^{-1}\partial_b B$ is not regularized, the trace over the latter product of matrix would diverge. Note that there is no analytical reference test for flat plates, since for that case, the lateral force vanishes. This also holds for the F_M by construction, since the function g_M for the lateral force already vanishes if one of the plates is flat.

In Figs. D.15–D.16, the finite size convergence of the F_M to the lateral force F is shown in units of the normal force for flat plates, for the selected values of $\lambda/a = 10, 100$ and $H/a = 5, 10, 100$ at $b = \lambda/4$ for TM and TE modes (apart from the plot for $H/a = 5$ and $\lambda/a = 100$).

We observe that the exponential convergence sets in for the ratios $H/\lambda = 1$ and $H/\lambda = 1/2$ for cutoffs between $M = 13$ and $M = 20$ or $30 \leq 2M + 1 \leq 40$, for both TM and TE modes, see figures. A distinction between the modes is observed for $H/\lambda = 0.1$, where a slower convergence is expected.

For TM modes, the exponential convergence sets in later than for TE modes; the critical cutoff orders are $M \approx 22$ for TM modes and $M \approx 17$ for TE modes, respectively.

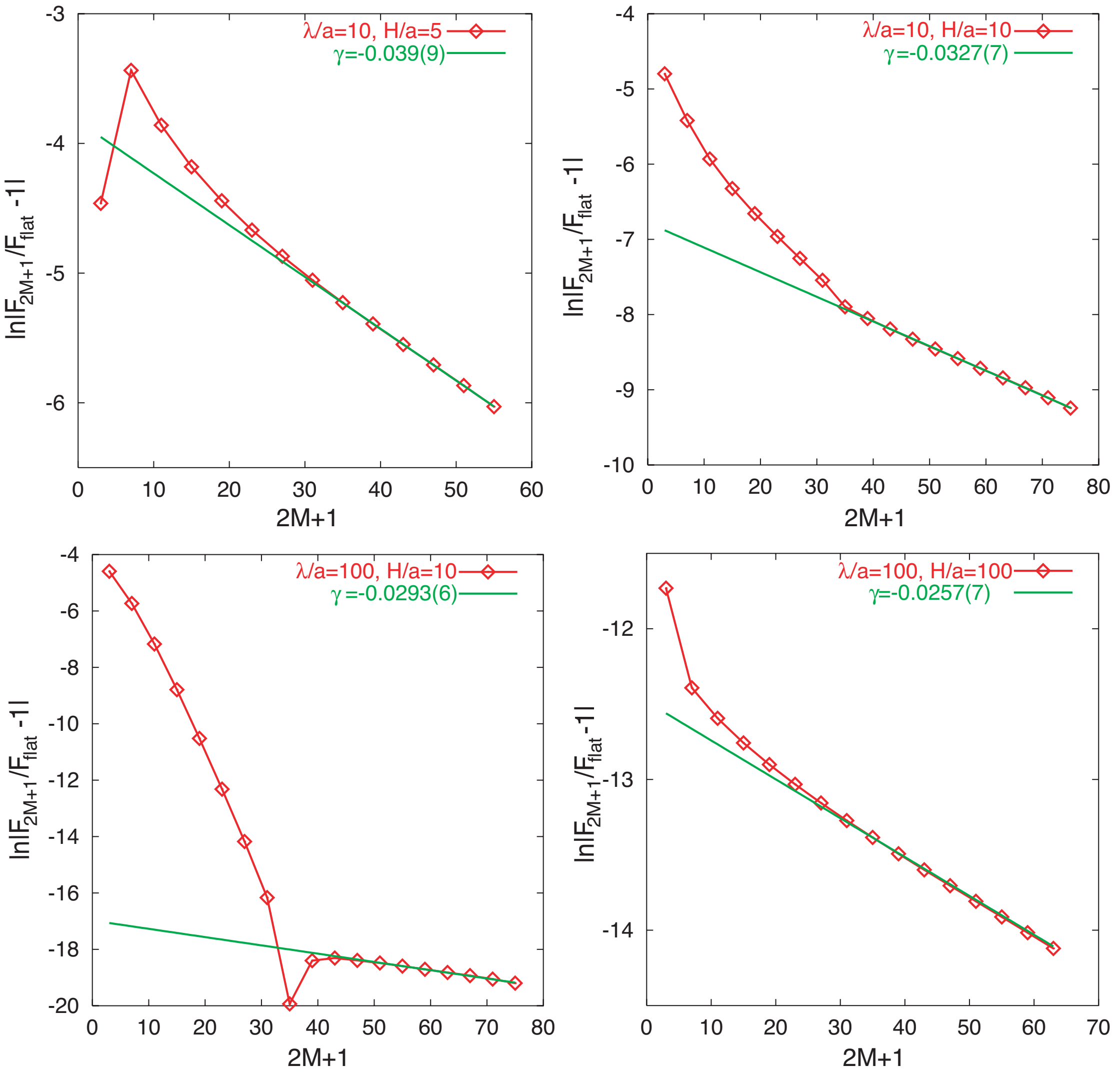

Figure D.15: Finite size scaling plots for the TM mode contributions for the lateral Casimir force at $b = \lambda/4$ and at fixed values of the corrugation length $\lambda/a = 10, 100$ and the distance $H/a = 5, 10, 100$. Displayed are the logarithmic finite size corrections $\ln|F_{2M+1}/F - 1|$ as a function of the modified cutoff order $2M + 1$ cf. Fig. D.8.

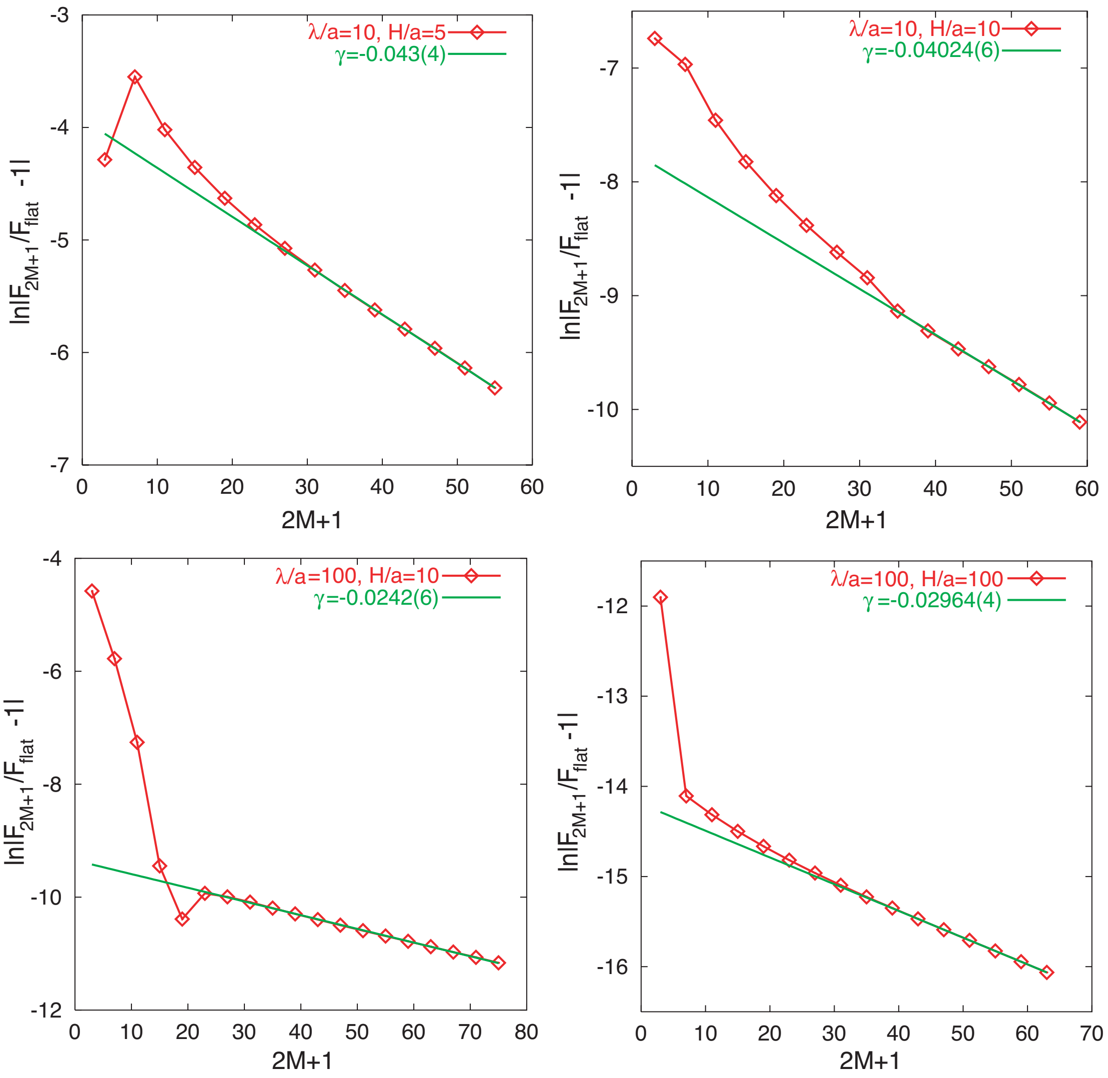

Figure D.16: Finite size scaling plots for the TE mode contributions for the lateral Casimir force at $b = \lambda/4$ and at fixed values of the corrugation length $\lambda/a = 10, 100$ and the distance $H/a = 5, 10, 100$; cf. the TM mode contributions in Fig. D.15.

3 Summary

This chapter was devoted to the study of the normal Casimir force between a flat plate and a plate with rectangular corrugation, and of the lateral Casimir force between two plates with rectangular corrugation, respectively.

The main purpose of this discussion is to obtain the Casimir interaction in those regimes where the approximation methods as the proximity approximation (PFA), pairwise summation of Casimir–Polder potentials (PWS) and perturbation theory are not feasible, as for plates with edges, including the case of large deformation amplitudes.

For the normal force, the perturbatively predicted existence of two different scaling regimes for the deformation induced part of the interaction as a function of the mean surface separation H could be confirmed. It was also found that for small corrugation lengths λ, only the large H scaling regime exists. For large λ and small H, the influence of diffraction at the edges decreases and the force approaches the results predicted by the PFA and by the PWS. This asymptotic behaviour could also be confirmed for the lateral force. By explicit calculations it was found that in the limit of very small corrugation lengths the force can be obtained as the interaction of two flat surfaces with a reduced distance. This limit is trivially fulfilled for the lateral force, which vanishes.

The scaling of the normal force close to the limits of small and large corrugation lengths were also computed. These limits provide an upper and lower bound, respectively, to the force. In both cases, a power law scaling with λ/a was found, rendering corrections to the PFA in general large. The exponents of these power laws depend on the type of modes for small corrugation length, whereas at large corrugation length we find an interesting dependence of the exponents on generic features of the corrugations.

By comparing with perturbation theory for a sinusoidal corrugation, it was found that edges induce a slower scaling towards the results of the PFA as compared to smooth profiles. This different scaling behaviour could be explained in terms of ray optics, a concept which was recently taken up by Jaffe and collaborators [58].

While for the normal Casimir force, effects beyond perturbation theory could be asserted, the lateral force appears to be well controllable by perturbation theory for arbitrary ratios of the distance H and the corrugation wavelength λ, as long as the deformation amplitude is the smallest length scale, which is generally assumed by perturbation theory. This is an unexpected result since edges pose no problem to the applicability of perturbation theory, contrary to the case of the normal force. This different qualitative behaviour between the normal and the lateral force was attributed to the fact that both forces are determined by different response kernels, with different analytic behaviour.

For distances H much larger than the corrugation wavelength, the lateral Casimir force becomes independent of the detailed surface structure, i.e. it becomes equal for *any* two uniaxially and periodically shaped surfaces of the same amplitude and deformation wavelength. This universal behaviour could be asserted by perturbation theory for small amplitudes, and there is evidence for this behaviour to be generic, only dependent on the ratio H/λ. The confirmation of these findings is left to future experiments, since in the experiment of Chen, Mohideen and co–workers [25], the lateral force was measured in a range of $H/\lambda < 1$, outside of the universal regime.

Since for periodic surfaces, the spectrum of deformations is bounded, this universal feature of the lateral force can not be expected for arbitrary surface deformations, as e.g. in the case of stochastic surface roughness.

E Density of states in periodic geometries

In this chapter, the trace formula Eq. (C1.14) of the density of states (DOS) which was introduced in chapter C.1 will be applied to the case of the periodic geometry with rectangular surface profiles which was considered for the discussion of the lateral Casimir force in chapter D.2.

The Casimir force is governed by the change of the DOS via Eq. (C1.18). (For the lateral force, the derivative with respect to the surface distance H in Eq. (C1.18) is to be replaced by the derivative with respect to the lateral shift b.) A calculation of the change of the DOS for a given geometry can be expected to be insightful regarding the relation between the change of the frequency spectrum and the interaction. Past a discussion of the normal and lateral Casimir forces in a given geometry, the question naturally arises which frequencies of the spectrum yield the dominant contributions to the interaction, and how the qualitative differences between the normal and the lateral force can be re–identified at the level of the DOS. In the previous chapter D, the distinct behaviour of the normal and of the lateral Casimir force was analysed numerically and perturbatively. While one can expect that a perturbative expansion of the change of the DOS for a general surface deformation should restore the results of the prior discussion, in the present chapter, we will confine ourselves to a numerical analysis.

In the first section, the change of the DOS will be calculated analytically for flat plates from the trace formula Eq. (C1.14). Then, it will be shown that the non–perturbative algorithm developed in chapter C.2 for the calculation of the Casimir force in periodic geometries can also be applied to calculate the change of the DOS, using the trace formula. The algorithm will be tested in the flat surface limit and the so obtained result is consistent with the analytic result.

In the second part of this chapter, for the geometry depicted in Fig. D.11, the DOS will be calculated numerically. This geometry has translational symmetry and can be subjected to a scalar field quantization. The obtained contributions to the DOS for TM and TE modes will be discussed qualitatively for different ratios of the surface deformation length and the surface separation. We also examine the convergence of the approximation to the DOS for finite cutoff order M for both contributions of TM and TE modes.

1 Analytic form of the density of states for flat plates

The starting point of our discussion is the trace formula in Eq. (C1.14),

$$\delta\rho(q_0) \;=\; -\frac{1}{\pi}\frac{\partial}{\partial q_0}\mathrm{Tr}\ln(\mathcal{M}\mathcal{M}_\infty^{-1}), \qquad \text{(E1.1)}$$

with the trace running over the 2D surface parametrization vector of the matrix kernel $\mathcal{M}$ and over the surface index. The frequency q_0 is excluded from the trace here. Inserting the momentum space representation $\tilde{\mathcal{M}}$ of the response kernel $\mathcal{M}$ for flat plates into Eq. (E1.1) yields for the change of the DOS per surface area A for each type of modes

$$\frac{\delta\rho(q_0)}{A} \;=\; -\frac{1}{\pi}\partial_{q_0}\int_{-\infty}^{\infty}\frac{dq_1}{2\pi}\int_{-\infty}^{\infty}\frac{dq_2}{2\pi}\,\ln\left(1-e^{-2qH}\right) \qquad \text{(E1.2)}$$

with $q=|\mathbf{q}|=\sqrt{q_0^2+q_1^2+q_2^2}$, since $\tilde{\mathcal{M}}$ is diagonal in momentum space. From Eq. (E1.2) one gets for the sum of both mode contributions

$$\frac{\delta\rho(q_0)}{A} \;=\; \frac{q_0}{\pi^2}\ln\left(1-e^{-2q_0H}\right). \qquad \text{(E1.3)}$$

Note that $\delta\rho(q_0)$ is non–analytic at for $q_0 \to 0$. For large $q_0H \gg 1$, using $\ln(1-z) = -\sum_{n=1}^{\infty} z^n/n$, the change of the DOS assumes the form

$$\frac{\delta\rho(q_0)}{A} \simeq -\frac{q_0}{\pi^2}\,e^{-2q_0H}. \qquad \text{(E1.4)}$$

For periodic geometries, the permutation algorithm introduced past Eq. (C2.24) can be applied. As a result, the kernel $\tilde{\mathcal{M}}$ in momentum space could be brought into block–diagonal form $\tilde{\mathcal{M}} = \mathrm{diag}\{\tilde{\mathcal{M}}_j\,|\,j=1,\ldots,N\}$ by discretizing the momentum q_1 which is parallel to the axis of corrugation. $\tilde{\mathcal{M}}_j$ are the sub–matrices at fixed momentum $q_1 = 2\pi j/W$ with $W=\lambda(N{+}1)$ being the system length along that axis. The trace over $\tilde{\mathcal{M}}$ is then obtained by summing the traces of the block–matrices $\tilde{\mathcal{M}}_j$, cf. Eq. (C2.29). We perform the derivative with respect to q_0 in Eq. (E1.1) and obtain

$$\partial_{q_0}\,\mathrm{Tr}\ln\tilde{\mathcal{M}} \;=\; \sum_{j=1}^{N}\mathrm{Tr}\big(\tilde{\mathcal{M}}_j^{-1}\partial_{q_0}\tilde{\mathcal{M}}_j\big). \qquad \text{(E1.5)}$$

Note the analogy to Eq. (C2.30), where the derivative is taken with respect to H for the calculation of the normal Casimir force. The traces in Eq. (E1.5) and in Eq. (C2.30) are different, since for the calculation of the force, the trace runs over *all* discrete and continuous arguments, including q_0.

With the matrix B defined in Eq. (C2.26), Eq. (E1.5) acquires the form cf. Eq. (C2.31),

$$\partial_{q_0} \operatorname{Tr} \ln \tilde{\mathcal{M}} \;=\; W \sum_{j=1}^{N} \sum_{\substack{k,l=-\infty \\ \alpha,\beta=1,2}}^{\infty} \int_{-\infty}^{\infty} \frac{dq_2}{2\pi} \left[B^{-1}_{kl,\alpha\beta} \cdot \partial_{q_0} B_{lk,\beta\alpha}\right]\left(q_0; q_1 = 2\pi j/W, q_2\right). \quad \text{(E1.6)}$$

The second sum in Eq. (E1.6) represents the trace tr over the discrete set of variables, and the sum over j will be substituted by the integral $(W/2\pi)\int_0^{2\pi/\lambda} dq_1$ in the continuum limit for q_1. In analogy to Eq. (C2.32), we define

$$\gamma(\mathbf{q}) \;\equiv\; \mathrm{tr}\left\{B^{-1}(\mathbf{q}) \cdot \partial_{q_0} B(\mathbf{q}) - B^{-1}_{\infty}(\mathbf{q}) \cdot \partial_{q_0} B_{\infty}(\mathbf{q})\right\}. \quad \text{(E1.7)}$$

For the numerical calculation, the trace tr will be cut off by restricting the summation over k, l to the set $-M, \ldots, M$, as before. Recall that the index ∞ in Eq. (E1.7) denotes that the limit of large surface distance $H \to \infty$ is performed. Then, one obtains the function γ_M which converges to γ as $M \to \infty$. Using the trace formula, one gets

$$\delta\rho(q_0) \;=\; -\frac{W^2}{\pi} \int_{-\infty}^{\infty} \frac{dq_2}{2\pi} \int_0^{2\pi/\lambda} \frac{dq_1}{2\pi}\, \gamma\left(q_0; q_1, q_2\right). \quad \text{(E1.8)}$$

Since $W^2 = A$ is the surface area, for the finite order approximation of the change of the DOS per surface area, one obtains

$$\frac{\delta\rho_M(q_0)}{A} \;=\; -\frac{1}{4\pi^3} \int_{-\infty}^{\infty} dq_2 \int_0^{2\pi/\lambda} dq_1\, \gamma_M\left(q_0; q_1, q_2\right). \quad \text{(E1.9)}$$

This expression is the basis for the numerical computation of the change of the DOS at fixed cutoff order M. To test the convergence, the limit of flat plates at distance H will be taken into account. Then, $B_{kl}\left(q_0; q_1, q_2\right) \;=\; \delta_{kl}\, N_0\left(q_0; q_1 + 2\pi l/\lambda, q_2\right)$, where for Dirichlet (TM) and Neumann (TE) boundary conditions N_0 is given by

$$N_{\mathsf{D},0}(\mathbf{q}) \;=\; \frac{1}{2q}\begin{pmatrix} 1 & e^{-qH} \\ e^{-qH} & 1 \end{pmatrix}, \qquad N_{\mathsf{N},0}(\mathbf{q}) \;=\; \frac{q}{2}\begin{pmatrix} -1 & e^{-qH} \\ e^{-qH} & -1 \end{pmatrix}, \quad \text{(E1.10)}$$

respectively, cf. Eq. (D1.3) and Eq. (D1.5) for $a = 0$. Using $\mathrm{tr}\ln = \ln\det$ for the trace over N_0 gives

$$\begin{aligned} \gamma_M(\mathbf{q}) \;&=\; \sum_{l=-M}^{M} \partial_{q_0} \ln \det\nolimits_{\alpha\beta}\left(N_0 N^{-1}_{0,\infty}\right)\left(q_0; q_1 + 2\pi l/\lambda, q_2\right) \\ &=\; \sum_{l=-M}^{M} \partial_{q_0} \ln\left(1 - e^{-2\tilde{q}_l H}\right) \;=\; 2Hq_0 \sum_{l=-M}^{M} \tilde{q}_l^{-1}\left(e^{2\tilde{q}_l H} - 1\right)^{-1}, \end{aligned} \quad \text{(E1.11)}$$

where we introduced $\tilde{q}_l = \sqrt{q_0^2 + (q_1 + 2\pi l/\lambda)^2 + q_2^2}$. Eq. (E1.11) holds for both TM and TE modes. A comparison with Eq. (C2.36) shows that $\gamma_M(\mathbf{q})$ decays even faster than g_M as a function of q_1. From Eq. (E1.9) one gets for the total change of the DOS per surface area A

$$\frac{\delta\rho_M(q_0)}{A} = -\frac{1}{2\pi^3}\int_{-\infty}^{\infty} dq_2 \int_{-2\pi M/\lambda}^{2\pi(M+1)/\lambda} dq_1\, \partial_{q_0} \ln\left(1 - e^{-2qH}\right). \tag{E1.12}$$

For $M \to \infty$, the boundaries of the integral over q_1 extend to infinity and Eq. (E1.12) yields

$$\frac{\delta\rho(q_0)}{A} = -\frac{q_0}{\pi^2}\int_{q_0}^{\infty} ds\, \partial_s \ln\left(1 - e^{-2sH}\right) = \frac{q_0}{\pi^2}\ln\left(1 - e^{-2q_0H}\right), \tag{E1.13}$$

which is the total change of the DOS per unit area for flat plates, cf. Eq. (E1.3). As it can be seen from Eq. (E1.12), the correction for finite order converges to zero exponentially fast as $\delta\rho - \delta\rho_M \sim e^{-4\pi MH/\lambda}$.

2 Numerical results

In Figs. E.1, E.2, the change of the DOS per surface area is shown in units of H as a function of Hq_0 for the cutoff orders $M = 1, 5, 9, 13$. Since $\delta\rho < 0$, the change of the DOS is also multiplied by (-1). The data for finite cutoff orders appear to be rapidly convergent for intermediate and small deformation wavelengths $\lambda = a$, $\lambda = 10a$ and $H \gtrsim \lambda$ at fixed distance $H = 10a$. In these cases, only the data curve for the lowest order $M = 1$ can be distinguished from the other curves, at best. For the larger value $\lambda = 100a$ at $H = 10a$, the data for $M = 1$ can still clearly be distinguished from the data of higher cutoff order, however, the data for $M \geq 5$ are saturating and can not be distinguished any more in the figures. For $\lambda = 10a$ and $H = 2.5a$, where the plates have a small reduced distance $\delta = 0.5a$, the convergence becomes slower, for $M \geq 9$, the data reach the saturation regime of convergence as well. Note that the curve for $M = 13$ is only a small correction to the curve for $M = 9$, compared to the differences between the data curves of lower order.

We also considered the change of the DOS for the ratios $b = 0$ and $b = \lambda/4$, represented by the red and by the green curves in Figs. E.1, E.2, respectively. While for $H \gtrsim \lambda$, the change of the DOS is almost indistinguishable for both values of b, for $\lambda = 100a$ and $H = 10a$, the change of the DOS is slightly larger for $b = \lambda/4$ than for $b = 0$ in the regime $Hq_0 \gtrsim 1$. A pronounced deviation is notable for $\lambda = 10a$ and $H = 2.5a$, where the change of the DOS for $b = \lambda/4$ is larger than for $b = 0$. The strongest deviation appears for $Hq_0 \gtrsim 2$. While for TM modes, the maximum of the change of the DOS is shifted to larger frequencies q_0, for TE modes, the position of the maximum is almost unchanged, and the change of the DOS

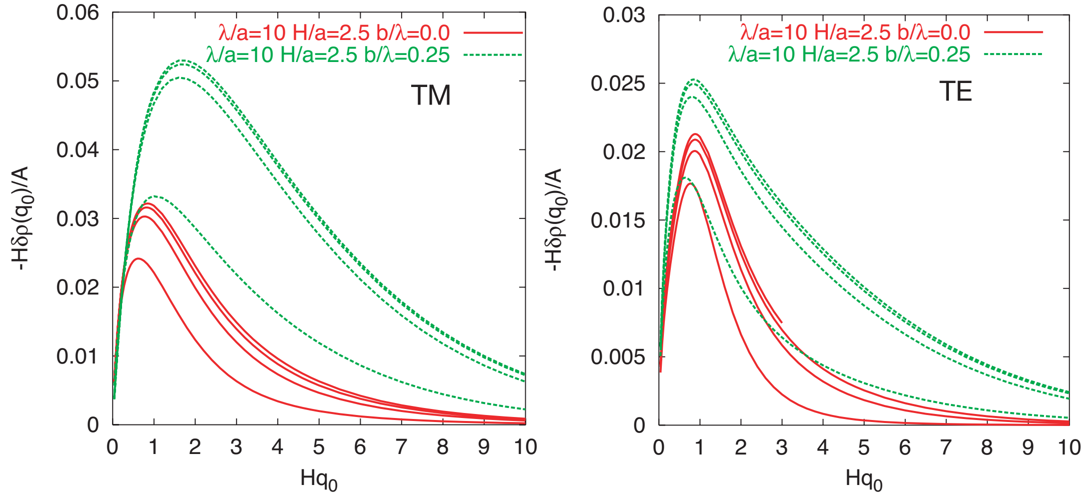

Figure E.1: change of the DOS for TM modes (left column) and TE modes (right column) for finite orders $M = 1, 5, 9, 13$ for $H/a = 2.5$ and $\lambda/a = 10$. Both $\delta/\lambda = 0.05$ and $\delta/a = 0.5$ are small, and there is a pronounced difference in the change of the DOS between $b/\lambda = 0$ and $b/\lambda = 0.25$.

is not so strongly amplified for frequencies around the maximum as for larger $q_0 \gtrsim 2/H$. Contrary to that, the amplification of the change of the DOS for TM modes is more uniform.

In the following, the discussion will be constricted to the data for finite cutoff order $M = 13$. Due to the fast convergence of the change of the DOS, this seems to be a reasonable assumption as long as the reduced distance δ is still of the order of the deformation amplitude a and as long as the corrugation length λ does not exceed the distance H by more than one order of magnitude, which is not the case for the considered range of length scales.

As a qualitative argument for the difference of the shape of the change of the DOS for $b = 0$ and $b = \lambda/4$ one can think of the following: the variation of the geometry as a whole is small if the corrugated plates are shifted relative to each other by $\lambda/4$ for a large ratio H/λ. Therefore, one can expect that the change of the DOS is not strongly affected by this shift. However, if H/λ and λ/a become small, which corresponds to a large curvature at small distances for *smooth* profiles, the geometry is strongly changed by a shift of $\lambda/4$ such that the spectral problems for both situations are widely different from each other. Therefore, a notable variation of the change of the DOS can be expected as well. While for $b = 0$, the plates in our geometry in Fig. D.11 are in an (unstable) equilibrium position and the segments of the surfaces have a local distance of H everywhere, for $b = \lambda/4$, the interaction is amplified. This can be understood as follows: On the one hand, in the previous discussion in chapter D.2 it was shown that the lateral Casimir force assumes its maximum close to

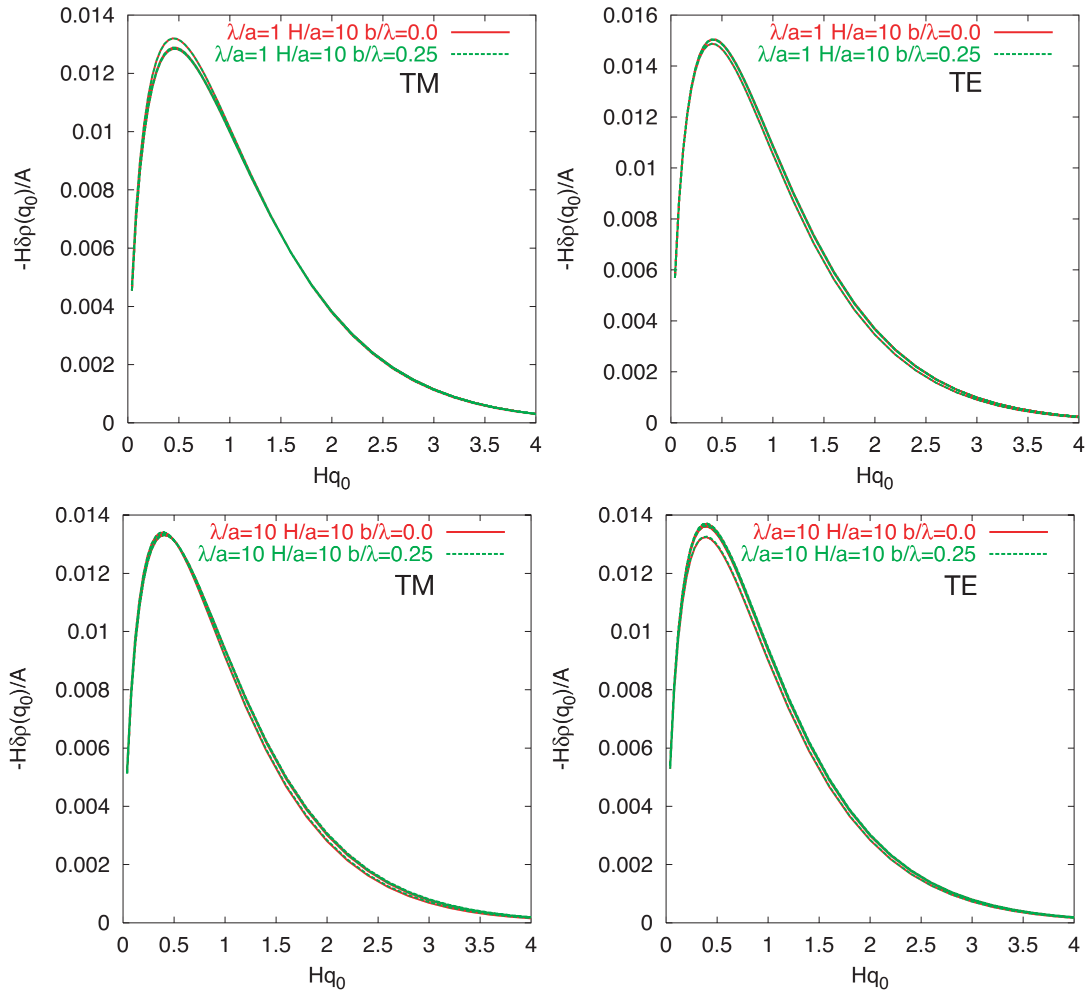

Figure E.2: change of the DOS for TM modes (left column) and TE modes (right column) for finite orders $M = 1, 5, 9, 13$ and for $H/\lambda = 1, 10$ $(\delta/\lambda = 8, 0.8)$. The curves for $b/\lambda = 0$ and $b/\lambda = 0.25$ are almost indistinguishable, contrary to the curves in Fig. E.1.

$b = \lambda/4$. On the other hand, the normal force can be expected to be larger as well, since the local distance of the surface will be the reduced to $\delta = H - 2a$ for one half of the deformation wavelength. Thus, the amplification of the change of the DOS reveals the stronger interaction at $b = \lambda/4$. The shift of the maximum of the change of the DOS to larger frequencies for TM modes, cf. Fig. E.1, reflects the fact that for $b = \lambda/4$, the main contribution results from modes with smaller wavelengths. However, for TE modes, this is not the case.

In the following, we consider the change of the change of the DOS at fixed distance $H = 10a$

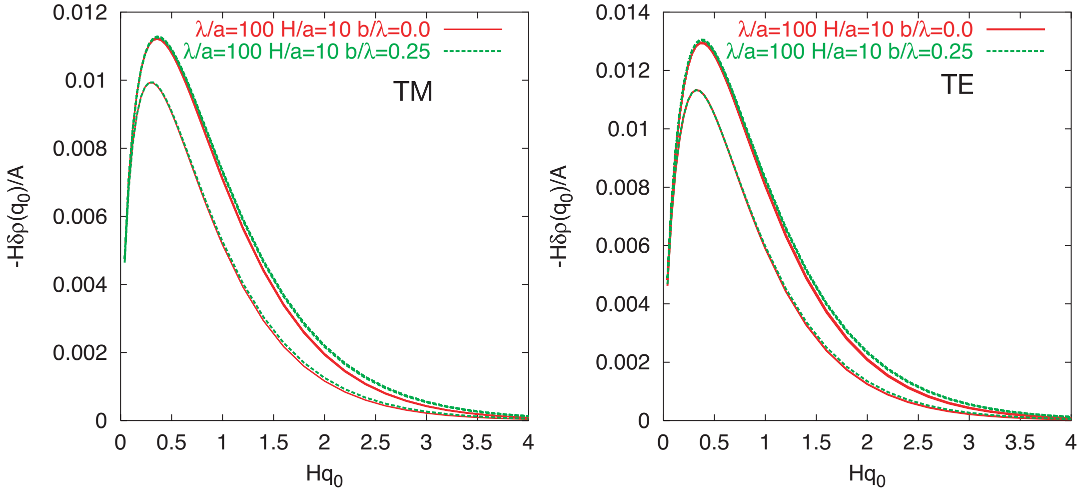

Figure E.3: change of the DOS for TM modes (left column) and TE modes (right column) for finite orders $M = 1, 5, 9, 13$ and for $H/\lambda = 100$ ($\delta/\lambda = 0.08$). The curves for $b/\lambda = 0$ and $b/\lambda = 0.25$ are almost indistinguishable, contrary to the curves in Fig. E.1.

and for $b = 0$. Figs. E.4 and E.5 display the numerical results for the change of the DOS for TM modes (left part) and TE modes (right part) as a function of Hq_0, for $\lambda/a = 1, 10, 100$, respectively. These values cover two orders of magnitude for the ratio H/λ. The figures also display the result for flat plates at distance $H(= 10a)$ and at reduced distance $\delta = H - 2a(= 8a)$. At reduced distance, the change of the DOS is amplified over the whole range of frequencies q_0 due to the stronger interaction at smaller distances. The maximum is shifted to larger values of q_0, which is consistent with the fact that the dominant contribution to the interaction comes from frequencies $q_0 \sim 1/H$.

While in the intermediate regime for $H/\lambda = 1$, cf. Fig. E.4, the numerical results for the corrugated surfaces are similar for TM and TE modes, significant differences emerge for $H/\lambda = 0.1$ and $H/\lambda = 10$. Since for small frequencies $q_0 \ll 1/\lambda$, the wavelengths of the modes are large compared to the corrugation wavelength λ, one can expect that these modes are confined by the outer segments of the plates and the change of the DOS approaches effectively the change of the DOS for flat plates at reduced distance. In Fig. E.4, this expectation is confirmed by the behaviour of the TE modes. However, the result for TM modes appears to be more closely located to the result for flat plates. In chapter D (see Pg. 67), it was assumed that the concave corners of the rectangular profile might pose a stronger restriction to TE waves, which satisfy Neumann conditions, than to TM waves. This could give an explanation for the unexpected behaviour of the TM modes.

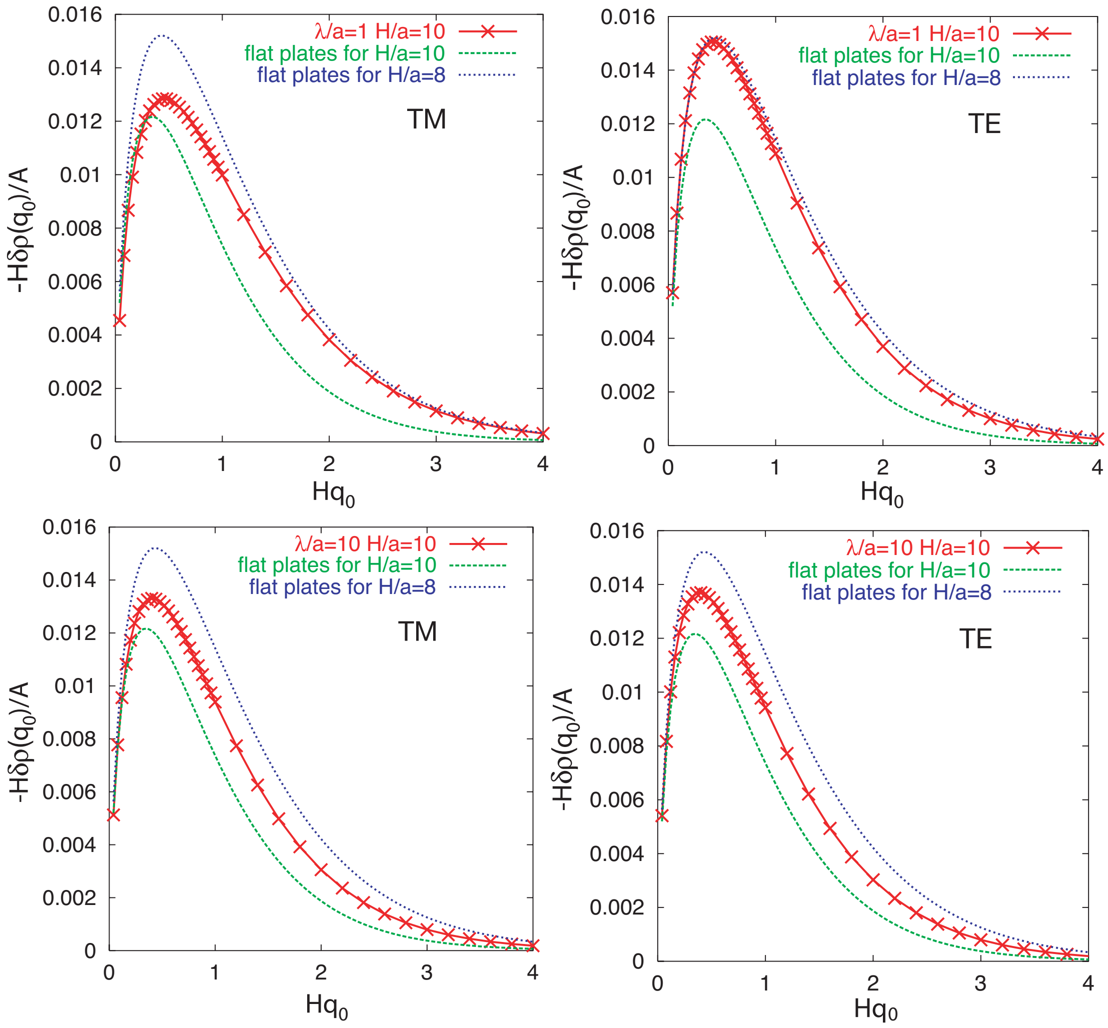

Figure E.4: change of the DOS $\delta\rho(q_0)$ for the geometry in Fig. D.11 for $b/\lambda = 0$, $H = 10a$ and $\lambda/a = 1, 10$ and for finite cutoff order $M = 13$ for TM modes (left) and TE modes (right). Shown are also the results for flat plates at $H = 10a$ (dashed curves) and at reduced distance $H = 8a$ (dotted curves). For the rescaled frequency (Hq_0)–axis, $H = 10a$.

Fig. E.5 shows the change of the DOS for $H/\lambda = 0.1$ and $q_0 \gg 1/\lambda$. The TM result is located close to the result for flat plates apart for frequencies close to the maximum. The result for TE modes appears to be only slightly amplified compared to the result for flat plates. Since frequencies in the range $q_0 \gg 1/\lambda$ are expected to resolve the surface structure, these results suggest that in the limit $H \ll \lambda$, the change of the DOS can be obtained as a sum of its contributions from *local* space domains. This would be in accordance with the

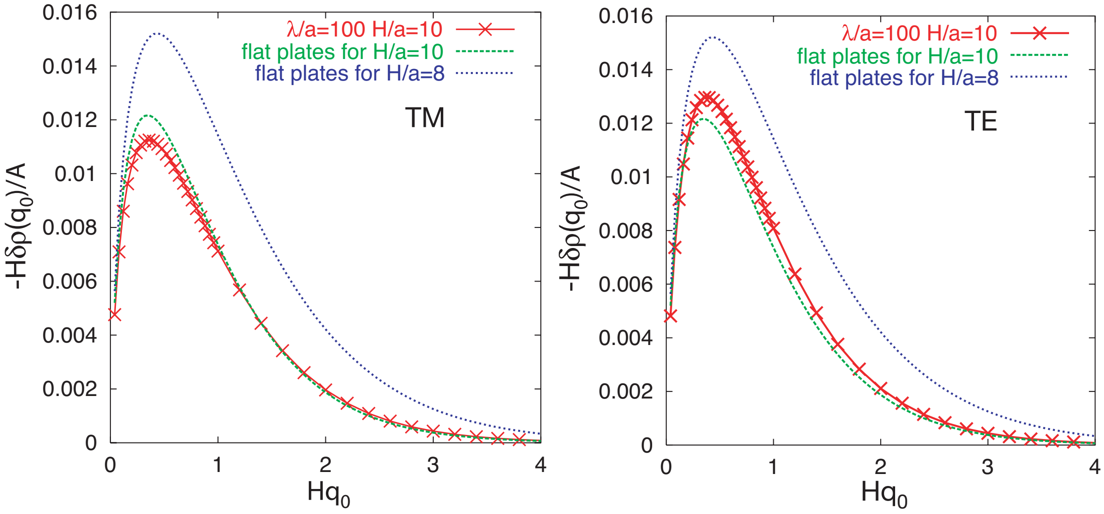

Figure E.5: Same plot as E.4 for TM modes (left) and TE modes (right) for $\lambda/a = 100$.

observation that both lateral and normal Casimir forces can be described by the proximity approximation in the regime $H \ll \lambda$, where diffraction at the edges can be neglected and the interaction is obtained as a sum over its *local* contributions.

3 Summary

Past the derivation of the trace formula for the change of the DOS in chapter C, in the present chapter we dedicated the attention to the behaviour of the change of the DOS as a function of the frequency q_0. The numerical method introduced in the second part of chapter C was applied to calculate the change of the DOS numerically for a geometry with square wave corrugated plates. A rapid convergence of the finite–order approximation of the change of the DOS could be observed. Moreover, a qualitatively different behaviour of the TM and TE mode contributions to the DOS was found for the cases that the ratio H/λ between the surface distance and the deformation wavelength becomes either large or small. We expect a perturbation expansion of the DOS to be feasible and beneficial in order to understand these differences at an analytical level, at least for small and smooth surface deformations.

F Appendix

1 Correlation functions and the density of states

In this appendix, we use the scalar field quantization in Euclidean space to derive a relation between the 2–point correlation function (Green function) for a given geometry with boundary surfaces and the free Green function for the system without boundaries. The deduction presented here follows closely the approach outlined in [53], but allows for Dirichlet, Neumann, and also mixed mode boundary conditions. In the second part, we derive from the relation between the density of states (DOS) and the Green function in Eq. (C1.9) the trace formula Eq. (C1.14) using the relation for the Green functions deduced in the first part.

1.1 The Green function for boundaries

The massless scalar field is described by the Gaussian action in Euclidean space by

$$S\{\Phi\} = \frac{1}{2}\int d^4X(\nabla\Phi)^2 \tag{F1.1}$$

with the nabla operator ∇ in 4D Euclidean spacetime. Given a family of S_α of submanifolds in the Euclidean spacetime enumerated by the (discrete) index α, each point of the manifold is represented by a vector $X_\alpha(\mathbf{u}) = (X^\mu_\alpha(\mathbf{u}))_{\mu=0,\dots 3}$ where the 3D parametrization vector is given by $\mathbf{u} = (u_0, \mathbf{u}_\|)$. Note that $\mathbf{u}_\|$ is not necessarily cartesian. Since the further discussion will be restricted to manifolds which correspond to rigid surfaces in space (i.e. the shape of the surfaces is constant in time), and moreover, to stationary problems, each point of the manifold is given by $X_\alpha(\mathbf{u}) = \big(u_0, \mathbf{s}_\alpha(\mathbf{u}_\|)\big)$. However, the formalism is sufficiently general to allow for fluctuating surfaces in arbitrary dimensions as well, see Ref. [53] for further details.

The generating functional for correlation functions is given by

$$\mathscr{Z}\{J\} = \left\langle e^{\int d^4X\, J(X)\Phi(X)} \right\rangle \tag{F1.2}$$

with the average $\langle \dots \rangle$ defined by

$$\langle F\rangle \equiv \mathscr{N}^{-1}\int \mathscr{D}\Phi(X)\prod_\alpha\prod_{X_\alpha}\delta\left[\hat{\mathcal{D}}_\alpha\Phi(X_\alpha)\right] e^{-S\{\Phi\}}\,F, \tag{F1.3}$$

where $\mathscr{N}$ is the normalization constant, such that $\langle 1\rangle = 1$. Correlation functions of Nth order can be obtained via functional derivatives from the generating functional as $\big\langle \Phi(X_1)\dots\Phi(X_N)\big\rangle = \delta^N \mathcal{Z}\{J\}/\big(\delta J(X_1)\dots\delta J(X_N)\big)\big|_{\{J\}=0}$. The differential operator $\hat{\mathcal{D}}_\alpha$ determines the kind of boundary condition, e.g. $\hat{\mathcal{D}}_\alpha = 1$ for Dirichlet–BC, $\hat{\mathcal{D}}_\alpha = \partial_{\hat{\mathbf{n}}_\alpha} = \hat{\mathbf{n}}_\alpha\cdot\nabla$ for Neumann–BC, any linear combination of both (as e.g. the boundary condition used in the scalar field based derivation of the Lifshitz theory). More generally, an arbitrary linear operator $\hat{\mathcal{D}}_\alpha(\nabla)$ is feasible. The delta functions in Eq. (F1.3) can be represented as a functional integral over an auxiliary field Ψ_α for all α as

$$\prod_{X_\alpha} \delta\left[\hat{\mathcal{D}}_\alpha \Phi(X_\alpha)\right] \;=\; \int \mathscr{D}\Psi_\alpha(X_\alpha)\, e^{i\sum_\alpha \int_{S_\alpha} dX_\alpha \Psi_\alpha(X_\alpha)\,\hat{\mathcal{D}}_\alpha \Phi(X_\alpha)}. \tag{F1.4}$$

Via partial integration, the differential operators $\hat{\mathcal{D}}_\alpha$ in Eq. (F1.4) can now be shifted onto the auxiliary fields Ψ_α. This changes the sign at every single derivative in the operators, which may be denoted by $\hat{\mathcal{D}}^-_\alpha \equiv \hat{\mathcal{D}}_\alpha(-\nabla)$. Transforming the integration over the surface S_α in the exponent on the right hand side of Eq. (F1.4) to the integration over the parametrization vector $\mathbf{u}$, one gets

$$\begin{aligned}\prod_{X_\alpha} \delta\left[\hat{\mathcal{D}}_\alpha \Phi(X_\alpha)\right] \;&=\; \int \mathscr{D}\Psi_\alpha\big(X_\alpha(\mathbf{u})\big)\, e^{i\sum_\alpha \int d\mathbf{u}\, \Phi[X_\alpha(\mathbf{u})]\, \hat{\mathcal{D}}^-_\alpha \Psi_\alpha[X_\alpha(\mathbf{u})]\sqrt{g_\alpha(\mathbf{u})}} \\ &\equiv\; \int \mathscr{D}\Psi_\alpha\big(X_\alpha(\mathbf{u})\big)\, e^{\int d^4X\, \Phi(X)\rho(X)}.\end{aligned} \tag{F1.5}$$

g_α is the determinant of the induced metric which appears in the surface measure, see Eq. (B1.19). The field ρ is defined by the integral relation in the exponential function of Eq. (F1.5), it is introduced formally to perform the Gaussian integration over $\Phi(X)$, which is done by inserting the left hand side of Eq. (F1.5) into Eq. (F1.3) for $F \to 1$. This leads to

$$\mathscr{N} \;=\; \int \prod_\alpha \mathscr{D}\Psi_\alpha\big(X_\alpha(\mathbf{u})\big)\, e^{\frac{1}{2}\int_X\int_{X'} \rho(X)\, \mathcal{G}_{\mathsf{E},0}(X,X')\rho(X')} \tag{F1.6}$$

with the free Euclidean Green function $\mathcal{G}_{\mathsf{E},0}$. The evaluation of $\mathcal{Z}\{J\}$ corresponds to substituting $\rho \to \rho + J$ in Eq. (F1.6). This gives

$$\mathcal{Z}\{J\} \;=\; \mathscr{N}^{-1} C \int \prod_\alpha \mathscr{D}\Psi_\alpha(X_\alpha)\, e^{-S_{\mathsf{eff}}\{\Psi,J\}}, \tag{F1.7}$$

with the constant $C = e^{\frac{1}{2}\int_X\int_{X'} J(X)\, \mathcal{G}_{\mathsf{E},0}(X,X') J(X')}$, and the effective action can be read off by inserting the fields $\rho(X)$ and shifting the operators $\hat{\mathcal{D}}_\alpha$ onto the free Green function by partial integration. This leads to

$$\begin{aligned} S_{\mathsf{eff}}\{\Psi, J\} = \frac{1}{2}\sum_{\alpha\beta}\int_{\mathbf{u}}\int_{\mathbf{u}'} \psi_\alpha(\mathbf{u})\,\sqrt{g_\alpha(\mathbf{u})}\,\hat{\mathcal{D}}_\alpha\hat{\mathcal{D}}'_\beta\mathcal{G}_{\mathsf{E},0}\left(X_\alpha(\mathbf{u}), X_\beta(\mathbf{u}')\right)\sqrt{g_\beta(\mathbf{u}')}\,\psi_\beta(\mathbf{u}') \\ -\, i\sum_\alpha\int_X\int_{\mathbf{u}}\psi_\alpha(\mathbf{u})\,\sqrt{g_\alpha(\mathbf{u})}\,\hat{\mathcal{D}}_\alpha\mathcal{G}_{\mathsf{E},0}\big(X_\alpha(\mathbf{u}), X\big)\,J(X) \end{aligned} \tag{F1.8}$$

with the new auxilary fields $\psi_\alpha(\mathbf{u}) = \Psi_\alpha\big(X_\alpha(\mathbf{u})\big)$. The prime at the operator denotes that it acts on the primed variable. To get an measure for the path integral which is invariant under transformations of the local coordinates [42, 104], we introduce the field $\phi_\alpha(\mathbf{u}) \equiv g_\alpha(\mathbf{u})^{1/4}\psi_\alpha(\mathbf{u})$ which is weighted by the quartic root of the determinant of the induced Riemannian metric. Hence, Eq. (F1.7) can be reformulated as

$$\mathcal{Z}\{J\} = \mathscr{N}^{-1}C\int\prod_\alpha\mathscr{D}\phi_\alpha(\mathbf{u})\,e^{-S_{\mathsf{eff}}\{\phi,J\}}, \tag{F1.9}$$

with

$$S_{\mathsf{eff}}\{\phi, J\} = \frac{1}{2}\sum_{\alpha\beta}\int_{\mathbf{u}}\int_{\mathbf{u}'}\phi_\alpha(\mathbf{u})\,\hat{\mathcal{M}}_{\alpha\beta}\left(\mathbf{u},\mathbf{u}'\right)\phi_\beta(\mathbf{u}') - i\sum_\alpha\int_X\int_{\mathbf{u}}\phi_\alpha(\mathbf{u})\,\eta_\alpha(\mathbf{u}, X)\,J(X), \tag{F1.10}$$

and $\hat{\mathcal{M}}_{\alpha\beta}\left(\mathbf{u},\mathbf{u}'\right) \equiv g_\alpha(\mathbf{u})^{1/4}g_\beta(\mathbf{u}')^{1/4}\hat{\mathcal{D}}_\alpha\hat{\mathcal{D}}'_\beta\mathcal{G}_{\mathsf{E},0}\big(X_\alpha(\mathbf{u}), X_\beta(\mathbf{u}')\big)$, cf. Eqs. (B4.67)–(B4.68), and $\eta_\alpha(\mathbf{u}, X) \equiv g_\alpha(\mathbf{u})^{1/4}\hat{\mathcal{D}}_\alpha\mathcal{G}_{\mathsf{E},0}\big(X_\alpha(\mathbf{u}), X\big)$. The Gaussian integration in Eq. (F1.9) can be performed. Setting $\hat{\eta}_\alpha(\mathbf{u}) \equiv -i\int_X\eta_\alpha(\mathbf{u}, X)J(X)$, one gets

$$\begin{aligned} \mathcal{Z}\{J\} &= Ce^{\frac{1}{2}\sum_{\alpha\beta}\int_{\mathbf{u}}\int_{\mathbf{u}'}\hat{\eta}_\alpha(\mathbf{u})\,\hat{\mathcal{M}}^{-1}_{\alpha\beta}(\mathbf{u},\mathbf{u}')\,\hat{\eta}_\beta(\mathbf{u}')} \\ &= Ce^{-\frac{1}{2}\int_X\int_{X'}J(X)\,K(X,X')\,J(X')} \\ &= e^{-\frac{1}{2}\int_X\int_{X'}J(X)\left\{\mathcal{G}_{\mathsf{E},0}(X,X') - K(X,X')\right\}J(X')}, \end{aligned} \tag{F1.11}$$

where $K(X, X') \equiv \sum_{\alpha\beta}\int_{\mathbf{u}}\int_{\mathbf{u}'}\eta_\alpha(X, \mathbf{u})\,\hat{\mathcal{M}}^{-1}_{\alpha\beta}\left(\mathbf{u},\mathbf{u}'\right)\eta_\beta(\mathbf{u}', X')$. The kernel K can now be expressed in terms of the Green functions, since the metric factors $g_\alpha^{1/4}$ cancel each other. The Euclidean 2–point–correlation function between the points X and X' can now directly be obtained from the generating functional as

$$\begin{aligned} \mathcal{G}_{\mathsf{E}}\left(X, X'\right) &= \frac{\delta^2\mathcal{Z}\{J\}}{\delta J(X)\delta J(X')}\Big|_{\{J\}=0} = \mathcal{G}_{\mathsf{E},0}(X, X') - K(X, X') \\ &= \mathcal{G}_{\mathsf{E},0}(X, X') - \sum_{\alpha\beta}\int_{\mathbf{u}}\int_{\mathbf{u}'}\hat{\mathcal{D}}_\alpha\mathcal{G}_{\mathsf{E},0}\big(X, X_\alpha(\mathbf{u})\big)\,\mathcal{M}^{-1}_{\alpha\beta}\left(\mathbf{u},\mathbf{u}'\right)\,\hat{\mathcal{D}}'_\beta\mathcal{G}_{\mathsf{E},0}\big(X_\beta(\mathbf{u}'), X'\big) \end{aligned} \tag{F1.12}$$

with the matrix $\mathcal{M}_{\alpha\beta}\left(\mathbf{u},\mathbf{u}'\right) = \hat{\mathcal{D}}_\alpha \hat{\mathcal{D}}'_\beta \mathcal{G}_{\mathsf{E},0}\left(X_\alpha(\mathbf{u}), X_\beta(\mathbf{u}')\right)$ which was used before in the discussion of periodic geometries. Since the density of states is related to the *correction* of the Green function (for the given geometry) to the *free* Green function for the vacuum space $\tilde{\mathcal{G}}_{\mathsf{E}}\left(X,X'\right) \equiv \mathcal{G}_{\mathsf{E}}\left(X,X'\right) - \mathcal{G}_{\mathsf{E},0}\left(X,X'\right)$, the DOS is governed by the second term on the right hand side of Eq. (F1.12). To proceed, the partially Fourier transformed Euclidean Green function is to be evaluated:

$$\tilde{\mathcal{G}}_{\mathsf{E}}\left(q_0, q_0'; \mathbf{x}, \mathbf{x}'\right) \; = \; \int_{x_0} \int_{x_0'} e^{-iq_0x_0 - iq_0'x_0'}\, \tilde{\mathcal{G}}_{\mathsf{E}}\left(X, X'\right). \tag{F1.13}$$

Due to the choice of *static* boundaries and the homogenity of the Green function, the kernel $\mathcal{M}$ and its inverse are homogenious as well. Using these properties, Eq. (F1.13) transforms into

$$\begin{aligned}
\tilde{\mathcal{G}}_{\mathsf{E}}\big(q_0, q_0'; \mathbf{x}, \mathbf{x}'\big) \; &= \; -\sum_{\alpha\beta} \int_{x_0}\int_{x_0'}\int_{\mathbf{u}}\int_{\mathbf{u}'} e^{-iq_0x_0 - iq_0'x_0'}\, \hat{\mathcal{D}}_\alpha \mathcal{G}_{\mathsf{E},0}\big(x_0 - u_0, \mathbf{x} - \mathbf{s}_\alpha(\mathbf{u}_\parallel)\big) \\
&\qquad\qquad \times\; \mathcal{M}^{-1}_{\alpha\beta}\big(\mathbf{u},\mathbf{u}'\big)\, \hat{\mathcal{D}}'_\beta \mathcal{G}_{\mathsf{E},0}\big(u_0' - x_0', \mathbf{s}_\beta(\mathbf{u}_\parallel') - \mathbf{x}'\big) \\
&= -\sum_{\alpha\beta} \int_{x_0}\int_{x_0'}\int_{\mathbf{u}}\int_{\mathbf{u}'}\int \frac{dp_0}{2\pi}\int \frac{dp_0'}{2\pi}\int \frac{dq_0}{2\pi}\, e^{-iq_0x_0 - iq_0'x_0'}\, e^{ip_0(x_0-u_0) + ip_0'(u_0'-x_0') + iq_0(u_0 - u_0')} \\
&\qquad \times\; \hat{\mathcal{D}}_\alpha \mathcal{G}_{\mathsf{E},0}\big(p_0; \mathbf{x} - \mathbf{s}_\alpha(\mathbf{u}_\parallel)\big)\, \mathcal{M}^{-1}_{\alpha\beta}\big(q_0; \mathbf{u}_\parallel, \mathbf{u}_\parallel'\big)\, \hat{\mathcal{D}}'_\beta \mathcal{G}_{\mathsf{E},0}\big(p_0'; \mathbf{s}_\beta(\mathbf{u}_\parallel') - \mathbf{x}'\big) \\
&= -2\pi\delta(q_0 + q_0') \sum_{\alpha\beta} \int_{\mathbf{u}_\parallel}\int_{\mathbf{u}_\parallel'} \hat{\mathcal{D}}_\alpha \mathcal{G}_{\mathsf{E},0}\big(q_0; \mathbf{x} - \mathbf{s}_\alpha(\mathbf{u}_\parallel)\big) \mathcal{M}^{-1}_{\alpha\beta}\big(q_0; \mathbf{u}_\parallel, \mathbf{u}_\parallel'\big) \hat{\mathcal{D}}'_\beta \mathcal{G}_{\mathsf{E},0}\big(q_0; \mathbf{s}_\beta(\mathbf{u}_\parallel') - \mathbf{x}'\big).
\end{aligned} \tag{F1.14}$$

Since $\tilde{\mathcal{G}}(q_0, q_0'; \,\cdot\,) = 2\pi\delta(q_0 + q_0')\, \tilde{\mathcal{G}}(q_0; \,\cdot\,)$, one obtains for Dirichlet and Neumann boundary conditions explicitly

$$\tilde{\mathcal{G}}_{\mathsf{E}}\big(q_0; \mathbf{x}, \mathbf{x}'\big) \; = \; -\sum_{\alpha\beta} \int_{\mathbf{u}}\int_{\mathbf{u}'} \mathcal{G}_{\mathsf{E},0}\big(q_0; \mathbf{x} - \mathbf{s}_\alpha(\mathbf{u})\big)\, \mathcal{M}^{-1}_{\mathsf{D},\alpha\beta}\big(q_0; \mathbf{u}, \mathbf{u}'\big)\, \mathcal{G}_{\mathsf{E},0}\big(q_0; \mathbf{s}_\beta(\mathbf{u}') - \mathbf{x}'\big) \tag{F1.15}$$

where, for simplicity of notation, $\mathbf{u}$ is now considered to be the 2D parametrization vector. The kernel is given by $\mathcal{M}_{\mathsf{D},\alpha\beta}\left(q_0; \mathbf{u}, \mathbf{u}'\right) = \mathcal{G}_{\mathsf{E},0}\big(q_0; \mathbf{s}_\alpha(\mathbf{u}) - \mathbf{s}_\beta(\mathbf{u}')\big)$. Anologously, Neumann boundary conditions yield

$$\tilde{\mathcal{G}}_{\mathsf{E}}\big(q_0; \mathbf{x}, \mathbf{x}'\big) = -\sum_{\alpha\beta} \int_{\mathbf{u}}\int_{\mathbf{u}'} \partial_{\hat{\mathbf{n}}_\alpha} \mathcal{G}_{\mathsf{E},0}\big(q_0; \mathbf{x} - \mathbf{s}_\alpha(\mathbf{u})\big) \mathcal{M}^{-1}_{\mathsf{N},\alpha\beta}\big(q_0; \mathbf{u}, \mathbf{u}'\big)\, \partial_{\hat{\mathbf{n}}'_\beta} \mathcal{G}_{\mathsf{E},0}\big(q_0; \mathbf{s}_\beta(\mathbf{u}') - \mathbf{x}'\big) \tag{F1.16}$$

with the kernel $\mathcal{M}_{\mathsf{N},\alpha\beta}\left(q_0; \mathbf{u}, \mathbf{u}'\right) = \partial_{\hat{\mathbf{n}}_\alpha} \partial_{\hat{\mathbf{n}}'_\beta} \mathcal{G}_{\mathsf{E},0}\big(q_0; \mathbf{s}_\alpha(\mathbf{u}) - \mathbf{s}_\beta(\mathbf{u}')\big)$.

1.2 The trace formula

To calculate the density of states for the given geometry, the trace over the Green function for $\mathbf{x} = \mathbf{x}'$ must be calculated, which yields

$$
\begin{aligned}
\int d^3\mathbf{x}\, \tilde{\mathcal{G}}_{\mathsf{E}}(q_0;\mathbf{x},\mathbf{x}) \;&=\; -\sum_{\alpha\beta} \int_{\mathbf{x}}\int_{\mathbf{u}}\int_{\mathbf{u}'} \hat{\mathcal{D}}_\alpha \mathcal{G}_{\mathsf{E},0}\big(q_0;\mathbf{x}-\mathbf{s}_\alpha(\mathbf{u})\big) \\
&\qquad\qquad \times\; \mathcal{M}^{-1}_{\alpha\beta}\big(q_0;\mathbf{u},\mathbf{u}'\big)\, \hat{\mathcal{D}}'_\beta \mathcal{G}_{\mathsf{E},0}\big(q_0;\mathbf{s}_\beta(\mathbf{u}')-\mathbf{x}\big) \\
&= -\sum_{\alpha\beta} \int_{\mathbf{x}}\int_{\mathbf{u}}\int_{\mathbf{u}'}\int \frac{d^3q}{(2\pi)^3}\, e^{i\mathbf{q}\cdot(\mathbf{x}-\mathbf{s}_\alpha(\mathbf{u}))}\, \frac{\hat{\mathcal{D}}_\alpha(i\mathbf{q})}{q_0^2+\mathbf{q}^2}\, \mathcal{M}^{-1}_{\alpha\beta}\left(q_0;\mathbf{u},\mathbf{u}'\right) \\
&\qquad \times \int \frac{d^3q'}{(2\pi)^3}\, e^{i\mathbf{q}'\cdot(\mathbf{s}_\beta(\mathbf{u}')-\mathbf{x}')}\, \frac{\hat{\mathcal{D}}'_\beta(i\mathbf{q}')}{q_0^2+\mathbf{q}'^2} \qquad\qquad \text{(F1.17)} \\
&= -\sum_{\alpha\beta} \int_{\mathbf{u}}\int_{\mathbf{u}'} \mathcal{M}^{-1}_{\alpha\beta}\left(q_0;\mathbf{u},\mathbf{u}'\right) \int_{\mathbf{q}} e^{i\mathbf{q}\cdot(\mathbf{s}_\beta(\mathbf{u}')-\mathbf{s}_\alpha(\mathbf{u}))}\, \frac{\hat{\mathcal{D}}_\alpha(i\mathbf{q})\hat{\mathcal{D}}'_\beta(i\mathbf{q})}{\left(q_0^2+\mathbf{q}^2\right)^2} \\
&= \frac{1}{2q_0}\sum_{\alpha\beta} \int_{\mathbf{u}}\int_{\mathbf{u}'} \mathcal{M}^{-1}_{\alpha\beta}\left(q_0;\mathbf{u},\mathbf{u}'\right) \frac{\partial}{\partial q_0}\left[\hat{\mathcal{D}}_\alpha\hat{\mathcal{D}}'_\beta \int_{\mathbf{q}} \frac{e^{i\mathbf{q}\cdot(\mathbf{s}_\beta(\mathbf{u}')-\mathbf{s}_\alpha(\mathbf{u}))}}{q_0^2+\mathbf{q}^2}\right].
\end{aligned}
$$

Since the term in squared brackets is the transposed matrix kernel $\mathcal{M}_{\alpha\beta}(\mathbf{u}',\mathbf{u})$, Eq. (F1.17) yields

$$
\begin{aligned}
\int d^3\mathbf{x}\, \tilde{\mathcal{G}}_{\mathsf{E}}(q_0;\mathbf{x},\mathbf{x}) \;&=\; \frac{1}{2q_0}\sum_{\alpha\beta} \int_{\mathbf{u}}\int_{\mathbf{u}'} \mathcal{M}^{-1}_{\alpha\beta}\big(q_0;\mathbf{u},\mathbf{u}'\big)\, \frac{\partial}{\partial q_0}\, \mathcal{M}_{\beta\alpha}\big(q_0;\mathbf{u}',\mathbf{u}\big) \\
&= \frac{1}{2q_0}\frac{\partial}{\partial q_0}\,\mathrm{Tr}\ln\left(\mathcal{M}\right),
\end{aligned}
\qquad \text{(F1.18)}
$$

where the trace is taken over the set of "free" variables, i.e. at fixed q_0. Since the integral in Eq. (F1.18) extends over the whole space, we consider its disjunct partition into the volumes V_ν separated by the boundary surfaces of the geometry. The regularization of Eq. (F1.18) is performed by subtracting from the left hand side the part for which the distance H between the surfaces is taken to asymptotically large values. Then,

$$
\int_{\bigcup_\nu V_\nu} d^3\mathbf{x}\, \tilde{\mathcal{G}}_{\mathsf{E}}(q_0;\mathbf{x},\mathbf{x}) - \text{"}H\to\infty\text{"} \;=\; \frac{1}{2q_0}\frac{\partial}{\partial q_0}\mathrm{Tr}\ln\left(\mathcal{M}\mathcal{M}_\infty^{-1}\right). \qquad \text{(F1.19)}
$$

Since the left hand side of Eq. (F1.19) times the factor $-2q_0/\pi$ is the change of the Euclidean density of states $\delta\rho(q_0)$ for the whole system, see Eq. (C1.9), we get the trace formula

$$
\delta\rho(q_0) = -\frac{1}{\pi}\frac{\partial}{\partial q_0}\mathrm{Tr}\ln\left(\mathcal{M}\mathcal{M}_\infty^{-1}\right). \qquad \text{(F1.20)}
$$

2 Fourier transform of the rectangular corrugation

We calculate analytically the Fourier transform of them Matrix $\mathcal{M}$ of the rectangular corrugation model discussed in chapter D. Both plates are assumed to have a rectangular corrugation profile with the same wavelength λ, and amplitudes a_1, a_2.

We start with Dirichlet boundary conditions. Performing first the Fourier transformation of the orthogonal spacetime and frequency–momentum components defined by $\mathbf{x}_\perp = (x_0, x_2)$ and $\mathbf{p}_\perp = (p_0, p_2)$, respectively, we have

$$\begin{aligned}\tilde{\mathcal{M}}_{\mathsf{D}}^{\alpha\beta}(\mathbf{p},\mathbf{q}) &= \int_{\mathbf{x}_\perp}\int_{\mathbf{y}_\perp}\int_{x_1}\int_{y_1} e^{i\mathbf{p}_\perp\cdot\mathbf{x}_\perp + i\mathbf{q}_\perp\cdot\mathbf{y}_\perp} e^{ip_1x_1+iq_1y_1} \\ &\qquad \times\ \mathcal{G}\left(\mathbf{x}_\perp - \mathbf{y}_\perp, x_1 - y_1; h_\alpha(x_1) - h_\beta(y_1) + H(\delta_{\alpha 2} - \delta_{\beta 2})\right) \\ &= (2\pi)^2\delta^{(2)}(\mathbf{p}_\perp + \mathbf{q}_\perp)\int_{x_1}\int_{y_1}\int_{p_1'} e^{i(p_1-p_1')x_1+i(q_1+p_1')y_1} \\ &\qquad \times\ \frac{e^{-\sqrt{p_\perp^2+p_1'^2}\,|h_\alpha(x_1)-h_\beta(y_1)+H(\delta_{\alpha 2}-\delta_{\beta 2})|}}{2\sqrt{p_\perp^2+p_1'^2}}.\end{aligned} \tag{F2.21}$$

To evaluate this last expression analytically, it is necessary to find a simplified expression for the dependence of the second exponential term on x_1 and y_1. At this point, the use of piecewise constant profiles for the material plates becomes crucial: Since $h_\alpha = \pm a_\alpha$, for $\alpha = \beta$ we can write

$$e^{-\tilde{p}|h_\alpha(x_1)-h_\alpha(y_1)|} = e^{-a_\alpha\tilde{p}}\left[\cosh(a_\alpha\tilde{p}) + a_\alpha^{-2}\, h_\alpha(x_1)h_\alpha(y_1)\sinh(a_\alpha\tilde{p})\right]. \tag{F2.22}$$

Similarly, for $\alpha \neq \beta$, we get

$$\begin{aligned}e^{-\tilde{p}|h_\alpha(x_1)-h_\beta(y_1)+H(\delta_{\alpha 2}-\delta_{\beta 2})|} &= e^{-\tilde{p}H}\ \left[\cosh(a_\alpha\tilde{p}) - (-1)^\alpha a_\alpha^{-1}h_\alpha(x_1)\sinh(a_\alpha\tilde{p})\right] \\ &\quad \times\ \left[\cosh(a_\beta\tilde{p}) - (-1)^\beta a_\beta^{-1}h_\beta(x_1)\sinh(a_\beta\tilde{p})\right].\end{aligned} \tag{F2.23}$$

To keep the notation short, we introduced $\tilde{p} = \sqrt{p_\perp^2 + p_1'^2}$. We now insert the Fourier series expression for h_α given by

$$h_\alpha(x_1) = \frac{2a_\alpha}{\pi}\sum_{n=-\infty}^{\infty}\frac{(-1)^{n-1}}{2n-1}\, e^{\frac{2\pi i}{\lambda}(2n-1)(x_1+\delta_{\alpha 2}b)} \tag{F2.24}$$

into the right hand side of Eqs. (F2.22) and (F2.23). Then, inserting those into Eq. (F2.21), the remaining integrals over x_1, y_1 and p_1' can easily be performed. This yields the periodic formula

$$\tilde{\mathcal{M}}_{\mathsf{D}}(\mathbf{p},\mathbf{q}) = (2\pi)^3\delta^{(2)}(\mathbf{p}_\perp + \mathbf{q}_\perp)\sum_{m=-\infty}^{\infty}\delta\left(p_1 + q_1 + 2\pi m/\lambda\right)\, N_{\mathsf{D},m}(q_\perp, q_1) \tag{F2.25}$$

with the matrices

$$
\begin{aligned}
N_{\mathsf{D},m}\left(q_\perp,q_1\right) \;=\; & \begin{pmatrix} A^{\mathsf{D}}_{m,1}\left(q_\perp,q_1\right) & B^{\mathsf{D}}_{m,12}\left(q_\perp,q_1\right) \\ \gamma^m B^{\mathsf{D}}_{m,21}\left(q_\perp,q_1\right) & \gamma^m A^{\mathsf{D}}_{m,2}\left(q_\perp,q_1\right) \end{pmatrix} \\
& + \; \delta_{m0} \begin{pmatrix} \frac{1}{4q}(1+e^{-2a_1q}) & \frac{e^{-qH}}{2q}\cosh(a_1q)\cosh(a_2q) \\ \frac{e^{-qH}}{2q}\cosh(a_1q)\cosh(a_2q) & \frac{1}{4q}(1+e^{-2a_2q}) \end{pmatrix}
\end{aligned}
\tag{F2.26}
$$

for m even, and

$$
N_{\mathsf{D},m}\left(q_\perp,q_1\right) \;=\; \begin{pmatrix} 0 & C^{\mathsf{D}}_{m,12}\left(q_\perp,q_1\right) \\ C^{\mathsf{D}}_{m,21}\left(q_\perp,q_1\right) & 0 \end{pmatrix}
\tag{F2.27}
$$

for m odd. The entries of the matrices are given as follows

$$
A^{\mathsf{D}}_{m,\alpha}\left(q_\perp,q_1\right) \;=\; \frac{(-1)^{\frac{m}{2}}}{\pi^2}\sum_{k=-\infty}^{\infty}\frac{1}{(m-2k+1)(2k-1)}\frac{e^{-2a_\alpha\tilde{q}_{2k-1}}-1}{\tilde{q}_{2k-1}}\,, \tag{F2.28}
$$

$$
\begin{aligned}
B^{\mathsf{D}}_{m,\alpha\beta}\left(q_\perp,q_1\right) \;=\; & 2\,\frac{(-1)^{\frac{m}{2}}}{\pi^2}\sum_{k=-\infty}^{\infty}\frac{\gamma^{(2k-1)(\delta_{\beta2}-\delta_{\alpha2})}}{(m-2k+1)(2k-1)}\frac{e^{-\tilde{q}_{2k-1}H}}{\tilde{q}_{2k-1}} \\
& \times\,\sinh(a_\alpha\tilde{q}_{2k-1})\sinh(a_\beta\tilde{q}_{2k-1})\,,
\end{aligned}
\tag{F2.29}
$$

and

$$
\begin{aligned}
C^{\mathsf{D}}_{m,\alpha\beta}\left(q_\perp,q_1\right) \;=\; & \frac{(-1)^{\frac{m+1}{2}}}{m\pi}\left[(-1)^{\alpha}\gamma^{m\delta_{\alpha2}}\frac{e^{-qH}}{q}\sinh(a_\alpha q)\cosh(a_\beta q)\right. \\
& \left. +\;(-1)^{\beta}\gamma^{m\delta_{\beta2}}\frac{e^{-\tilde{q}_mH}}{\tilde{q}_m}\sinh(a_\beta\tilde{q}_m)\cosh(a_\alpha\tilde{q}_m)\right]\,,
\end{aligned}
\tag{F2.30}
$$

where the phase factor $\gamma = e^{2\pi ib/\lambda}$ was introduced. We note that the off–diagonal entries $B^{\mathsf{D}}_{m,\alpha\beta}$ and $C^{\mathsf{D}}_{m,\alpha\beta}$ implicitly depend on b through γ. Furthermore, we introduced the short hand notation $\tilde{q}_n = \left[q_\perp^2 + (q_1 + 2\pi n/\lambda)^2\right]^{1/2}$, which implies $q = \tilde{q}_0$.

In chapter D.1, the matrices $N_{\mathsf{D},m}$ have the symmetry $N_{\mathsf{D},m}\left(q_\perp,-q_1\right) = N_{\mathsf{D},-m}\left(q_\perp,q_1\right)$, and analogously for the Neumann matrices $N_{\mathsf{N},m}$. We remark that this symmetry is no longer valid here for either type of boundary conditions, since $h_2(x_1) \neq h_2(-x_1)$ in general. It is only recovered for $a_2 = 0$ or $b = l\lambda/2$ for any integer l.

The matrix $\tilde{\mathcal{M}}_{\mathsf{N}}$ for the Neumann boundary condition is obtained similarly as for the Dirichlet boundary condition. Evaluating first the Fourier transform of the orthogonal components as done in expression (F2.21), the result is

$$\begin{aligned}\tilde{\mathcal{M}}_{\mathsf{N}}^{\alpha\beta}(\mathbf{p},\mathbf{q}) &= (2\pi)^2\delta^{(2)}(\mathbf{p}_\perp+\mathbf{q}_\perp)\times\int_{x_1}\int_{y_1} e^{ip_1x_1+iq_1y_1}\\ &\qquad\times(-1)^{\alpha+\beta}\left(-\partial_{x_3}^2+\left(h'_\alpha(x_1)+h'_\beta(y_1)\right)\partial_{x_1}\partial_{x_3}-h'_\alpha(x_1)h'_\beta(y_1)\,\partial_{x_1}^2\right)\\ &\qquad\times\int_{p'_1} e^{-ip'_1(x_1-y_1)}\,\frac{e^{-\sqrt{p_\perp^2+p_1'^2}\,|x_3-y_3|}}{2\sqrt{p_\perp^2+p_1'^2}}\Bigg|_{\substack{x_3=h_\alpha(x_1)+H\delta_{\alpha2}\\ y_3=h_\beta(y_1)+H\delta_{\beta2}}}\\ &= (2\pi)^2\delta^{(2)}(\mathbf{p}_\perp+\mathbf{q}_\perp)\int_{x_1}\int_{y_1}\int_{p'_1} e^{i(p_1-p'_1)x_1+i(q_1+p'_1)y_1}\\ &\qquad\times\frac{(-1)^{\alpha+\beta}}{2}\left[-\sqrt{p_\perp^2+p_1'^2}-\frac{ip'_1}{\sqrt{p_\perp^2+p_1'^2}}\,(\partial_{x_1}-\partial_{y_1})-\frac{p_1'^2}{(p_\perp^2+p_1'^2)^{\frac{3}{2}}}\,\partial_{x_1}\partial_{y_1}\right]\\ &\qquad\times e^{-\sqrt{p_\perp^2+p_1'^2}\,|h_\alpha(x_1)-h_\beta(y_1)+H(\delta_{\alpha2}-\delta_{\beta2})|}.\end{aligned}\tag{F2.31}$$

We apply partial integration to obtain

$$\begin{aligned}\tilde{\mathcal{M}}_{\mathsf{N}}^{\alpha\beta}(\mathbf{p},\mathbf{q}) &= (2\pi)^2\delta^{(2)}(\mathbf{p}_\perp+\mathbf{q}_\perp)\times\frac{(-1)^{\alpha+\beta}}{2}\int_{p'_1}\Bigg[-\sqrt{p_\perp^2+p_1'^2}\\ &\qquad-\frac{p'_1}{\sqrt{p_\perp^2+p_1'^2}}\,(p_1-q_1-2p'_1)+\frac{p_1'^2}{(p_\perp^2+p_1'^2)^{\frac{3}{2}}}(p_1-p'_1)(q_1+p'_1)\Bigg]\\ &\qquad\times\int_{x_1}\int_{y_1} e^{i(p_1-p'_1)x_1+i(q_1+p'_1)y_1}\,e^{-\sqrt{p_\perp^2+p_1'^2}\,|h_\alpha(x_1)-h_\beta(y_1)+H(\delta_{\alpha2}-\delta_{\beta2})|}.\end{aligned}\tag{F2.32}$$

This expression will be treated analogously to the case of the matrix for the Dirichlet boundary condition, cf. Eq. (F2.21). It differs from the Dirichlet–kernel by the additional p'_1–dependent term. This yields again expression (F2.25), but now with $N_{\mathsf{D},m}$ substituted by the Neumann matrices $N_{\mathsf{N},m}$, which are given by

$$\begin{aligned}N_{\mathsf{N},m}(q_\perp,q_1) &= \begin{pmatrix} A^{\mathsf{N}}_{m,1}(q_\perp,q_1) & B^{\mathsf{N}}_{m,12}(q_\perp,q_1)\\ \gamma^m B^{\mathsf{N}}_{m,21}(q_\perp,q_1) & \gamma^m A^{\mathsf{N}}_{m,2}(q_\perp,q_1)\end{pmatrix}\\ &\quad+\delta_{m0}\begin{pmatrix} -\frac{q}{4}(1+e^{-2a_1q}) & \frac{q}{2}e^{-qH}\cosh(a_1q)\cosh(a_2q)\\ \frac{q}{2}e^{-qH}\cosh(a_1q)\cosh(a_2q) & -\frac{q}{4}(1+e^{-2a_2q})\end{pmatrix}\end{aligned}\tag{F2.33}$$

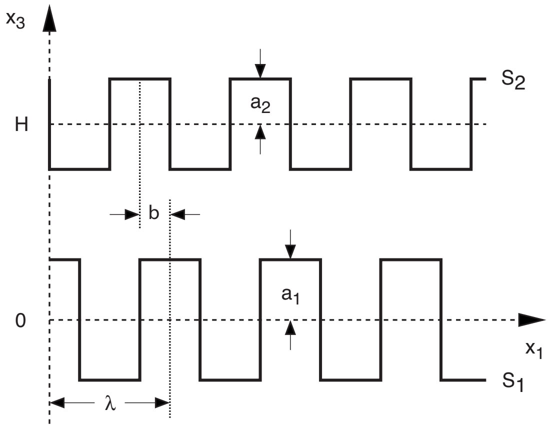

Figure F.1: Two stepwise constant plates with the same wavelength λ but with different amplitudes a_1 and a_2. The plates are translationally invariant into the y–direction.

for m even, and

$$N_{\mathsf{N},m}\left(q_\perp,q_1\right) = \begin{pmatrix} 0 & C^{\mathsf{N}}_{m,12}\left(q_\perp,q_1\right) \\ C^{\mathsf{N}}_{m,21}\left(q_\perp,q_1\right) & 0 \end{pmatrix} \tag{F2.34}$$

for m odd. The entries are now given by

$$\begin{aligned} A^{\mathsf{N}}_{m,\alpha}\left(q_\perp,q_1\right) &= \frac{(-1)^{\frac{m}{2}}}{\pi^2}\sum_{k=-\infty}^{\infty}\frac{1}{(m-2k+1)(2k-1)}\,\frac{1-e^{-2a_\alpha\tilde{q}_{2k-1}}}{\tilde{q}^3_{2k-1}} \\ &\qquad\times\phi_{mk}(q_\perp,q_1), \qquad\qquad (\mathrm{F2.35}) \\ B^{\mathsf{N}}_{m,\alpha\beta}\left(q_\perp,q_1\right) &= 2\,\frac{(-1)^{\frac{m}{2}}}{\pi^2}\sum_{k=-\infty}^{\infty}\frac{\gamma^{(2k-1)(\delta_{\beta2}-\delta_{\alpha2})}}{(m-2k+1)(2k-1)}\,\frac{e^{-\tilde{q}_{2k-1}H}}{\tilde{q}^3_{2k-1}} \\ &\qquad\times\sinh(a_\alpha\tilde{q}_{2k-1})\sinh(a_\beta\tilde{q}_{2k-1})\,\phi_{mk}(q_\perp,q_1), \qquad (\mathrm{F2.36}) \end{aligned}$$

and

$$\begin{aligned} C^{\mathsf{N}}_{m,\alpha\beta}\left(q_\perp,q_1\right) = \frac{(-1)^{\frac{m+1}{2}}}{m\pi}&\Bigg[(-1)^\alpha\gamma^{m\delta_{\alpha2}}\,e^{-qH}\left(q+\frac{2\pi m}{\lambda}\frac{q_1}{q}\right)\sinh(a_\alpha q)\cosh(a_\beta q) \\ &+\,(-1)^\beta\gamma^{m\delta_{\beta2}}e^{-\tilde{q}_mH}\left(\tilde{q}_m-\frac{2\pi m}{\lambda}\frac{q_1+2\pi m/\lambda}{\tilde{q}_m}\right) \\ &\times\,\sinh(a_\beta\tilde{q}_m)\cosh(a_\alpha\tilde{q}_m)\Bigg], \end{aligned} \tag{F2.37}$$

using the function

$$\begin{aligned}\phi_{mk}(q_\perp, q_1) \;=\;& q_1\big(q_1 + 2\pi m/\lambda\big)\big(q_1 + 2\pi(2k-1)/\lambda\big)^2 \\ &+ 2q_\perp^2\big(q_1 + \pi m/\lambda\big)\big(q_1 + 2\pi(2k-1)/\lambda\big) + q_\perp^4 .\end{aligned} \tag{F2.38}$$

As in the case of the Dirichlet–matrices, the off–diagonal elements depend on b via the phase factor $\gamma = e^{2\pi i b/\lambda}$. The matrices of the previous discussion of the rectangular corrugation model are now simply recovered by performing the limit $a_2 \to 0$ and by defining $a = a_1$.

3 Reduced distance for the matrices N_m

In this appendix, the limit $\lambda \to 0$ of the matrices $N_m(q_\perp, q_1)$ for the rectangular corrugation model of chapter D will be performed (cf. section 2 of this appendix for $a = a_1$, $a_2 = 0$ and $\lambda \to 0$), which corresponds to the limit of reduced distance, cf. Eq. (D1.10). These matrices depend on the distance of the argument q_1 to the positions $2\pi n/\lambda$, which requires diverse distinctions of cases. Considering this, for the Dirichlet case we find the simplified expressions

$$N_{\mathsf{D},0}\left(q_\perp, q_1 + 2\pi n/\lambda\right) \overset{\lambda\to 0}{=} \begin{cases} \begin{pmatrix} \frac{e^{-2aq}+1}{4q} & \frac{e^{-qH}}{2q}\cosh(aq) \\ \frac{e^{-qH}}{2q}\cosh(aq) & \frac{1}{2q} \end{pmatrix} & \text{for } n = 0 \\ \begin{pmatrix} -\frac{1}{\pi^2 n^2}\frac{e^{-2aq}-1}{q} & \epsilon \\ \epsilon & \frac{\lambda}{4\pi|n|} \end{pmatrix} & \text{for } n \text{ odd} \\ \begin{pmatrix} 0 & \epsilon \\ \epsilon & \frac{\lambda}{4\pi|n|} \end{pmatrix} & \text{for } n \text{ even} \end{cases} \tag{F3.39}$$

where we have introduced a small quantity ϵ, which is needed in order to have a non–singular matrix B_{kl}. However, at the end we can safely take $\epsilon \to 0$ in the final expression for the Casimir force. As $\lambda \to 0$, this quantity vanishes as $\epsilon \sim \lambda \exp(-2\pi n(H-a)/\lambda)$. The other matrices for $m \neq 0$ are given by

$$N_{\mathsf{D},m}\left(q_\perp, q_1 + 2\pi n/\lambda\right) \overset{\lambda \to 0}{=} \begin{cases} \begin{pmatrix} 0 & \frac{(-1)^{\frac{m-1}{2}}}{\pi m} \frac{e^{-qH}}{q} \sinh(aq) \\ 0 & 0 \end{pmatrix} & \text{for } n = 0 \\ \begin{pmatrix} 0 & 0 \\ \frac{(-1)^{\frac{m-1}{2}}}{\pi m} \frac{e^{-qH}}{q} \sinh(aq) & 0 \end{pmatrix} & \text{for } n = -m \\ \begin{pmatrix} 0 & 0 \\ 0 & 0 \end{pmatrix} & \text{for } n \notin \{-m, 0\} \end{cases} \tag{F3.40}$$

for odd m and

$$N_{\mathsf{D},m}\left(q_\perp, q_1 + 2\pi n/\lambda\right) \overset{\lambda \to 0}{=} \begin{cases} \begin{pmatrix} -\frac{(-1)^{\frac{m}{2}}}{\pi^2 n(m+n)} \frac{e^{-2aq}-1}{q} & 0 \\ 0 & 0 \end{pmatrix} & \text{for } n \text{ odd} \\ \begin{pmatrix} 0 & 0 \\ 0 & 0 \end{pmatrix} & \text{for } n \text{ even} \end{cases} \tag{F3.41}$$

for even $m \neq 0$. Analogously, for the von–Neumann matrices, we find

$$N_{\mathsf{N},0}\left(q_\perp, q_1 + 2\pi n/\lambda\right) \overset{\lambda \to 0}{=} \begin{cases} \begin{pmatrix} -\frac{q}{4}(e^{-2aq} + 1) & \frac{q}{2} e^{-qH} \cosh(aq) \\ \frac{q}{2} e^{-qH} \cosh(aq) & -\frac{q}{2} \end{pmatrix} & \text{for } n = 0 \\ \begin{pmatrix} \frac{4(-1)^{n-1}}{\lambda^2} \frac{q_1^2}{q^3} (e^{-2aq} - 1) & \epsilon \\ \epsilon & -\frac{\pi |n|}{\lambda} \end{pmatrix} & \text{for } n \text{ odd} \\ \begin{pmatrix} -\frac{1}{\lambda}\left[\frac{\pi |n|}{2} + \frac{2}{\pi} \tilde{C}_0(n)\right] & \epsilon \\ \epsilon & -\frac{\pi |n|}{\lambda} \end{pmatrix} & \text{for } n \text{ even} \end{cases} \tag{F3.42}$$

and

$$N_{\mathsf{N},m}\left(q_\perp, q_1 + 2\pi n/\lambda\right) \overset{\lambda\to 0}{=} \begin{cases} \begin{pmatrix} 0 & \frac{2(-1)^{\frac{m-1}{2}}}{\lambda}\frac{q_1}{q}\, e^{-qH}\sinh(aq) \\ 0 & 0 \end{pmatrix} & \text{for } n = 0 \\ \begin{pmatrix} 0 & 0 \\ -\frac{2(-1)^{\frac{m-1}{2}}}{\lambda}\frac{q_1}{q}\, e^{-qH}\sinh(aq) & 0 \end{pmatrix} & \text{for } n = -m \\ \begin{pmatrix} 0 & 0 \\ 0 & 0 \end{pmatrix} & \text{for } n \notin \{-m, 0\} \end{cases} \tag{F3.43}$$

for m odd, and

$$N_{\mathsf{N},m}\left(q_\perp, q_1 + 2\pi n/\lambda\right) \overset{\lambda\to 0}{=} \begin{cases} \begin{pmatrix} \frac{4(-1)^{\frac{m}{2}}}{\lambda^2}\frac{q_1^2}{q^3}(e^{-2aq} - 1) & 0 \\ 0 & 0 \end{pmatrix} & \text{for } n \text{ odd} \\ \begin{pmatrix} -\frac{2n(n+m)}{\pi\lambda}\tilde{C}_m(n) & 0 \\ 0 & 0 \end{pmatrix} & \text{for } n \text{ even}, n \notin \{-m, 0\} \\ \begin{pmatrix} \pm\frac{mq_1}{\pi^2}\tilde{C}_m(n) & 0 \\ 0 & 0 \end{pmatrix} & \text{for } n \in \{-m, 0\} \end{cases} \tag{F3.44}$$

for even $m \neq 0$.

Here, the asymptotic behaviour of ϵ for $\lambda \to 0$ is $\epsilon \sim \lambda^{-1}\exp(-2\pi n(H \pm a)/\lambda)$. The constant is given by $\tilde{C}_m(n) = (-1)^{m/2}\sum_{l=-\infty}^{\prime\infty}[(2l-1)(2l-1-m)|2l-1+n|\,]^{-1}$, and the prime at the summation sign indicates that $l \neq (1-n)/2$ if n is odd.

Bibliography

[1] Jarle Berntsen, The Computing Centre, University of Bergen, Thormohlens gt. 55, N-5008 Bergen, Norway.

[2] R. Balian and C. Bloch. *Ann. Phys. (N.Y.)*, 60:401, 1970.

[3] R. Balian and C. Bloch. *Ann. Phys. (N.Y.)*, 64:271, 1970.

[4] R. Balian and C. Bloch. *Ann. Phys. (N.Y.)*, 69:76, 1972.

[5] R. Balian and C. Bloch. *Ann. Phys. (N.Y.)*, 85:514, 1974.

[6] R. Balian and C. Bloch. *Ann. Phys. (N.Y.)*, 84:559, 1974.

[7] R. Balian and B. Duplantier. *Ann. Phys. (N.Y.)*, 104:300, 1977.

[8] R. Balian and B. Duplantier. *Ann. Phys. (N.Y.)*, 112:165, 1978.

[9] R. Balian and B. Duplantier. *quant-ph/0408124v1*, 2004.

[10] Yu. S. Barash and V. F. Ginzburg. *Sov. Phys. Usp.*, 18:305, 1973.

[11] V. B. Bezerra, G. L. Klimchitskaya, and V. M. Mostepanenko. *Phys. Rev. A*, 66:062112, 2002.

[12] V. B. Bezerra, G. L. Klimchitskaya, and C. Romero. *Phys. Rev. A*, 65:012111, 2002.

[13] M. Bordag and J. Lindig. *Phys. Rev. D*, 58:045003, 1998.

[14] M. Bordag, U. Mohideen, and V. M. Mostepanenko. *Phys. Rep.*, 353:1, 2001.

[15] M. Bordag, D. Robaschik, and E. Wieczorek. *Ann. Phys. (N.Y.)*, 165:192, 1985.

[16] M. Bordag and K. Scharnhorst. *Phys. Rev. Lett.*, 81:3815, 1998.

[17] M. Born and E. Wolf. *Principles of Optics*. Pergamon Press, Oxford, 1970.

[18] T. Boyer. *Phys. Rev. A*, 9:2078, 1974.

[19] E. Buks and M. L. Roukes. *Phys. Rev. B*, 63:033402, 2001.

[20] A. Bulgac and A. Wirzba. *Phys. Rev. Lett.*, 87:120404, 2001.

[21] A. A. Bytsenko, G. Cognola, L. Vanzo, and S. Zerbini. *Phys. Rep.*, 266:1, 1996.

[22] H. B. G. Casimir. *Proc. K. Ned. Akad. Wet.*, 51:793, 1948.

[23] H. B. G. Casimir and D. Polder. *Phys. Rev.*, 73:360, 1948.

[24] H. B. Chan, V. A. Aksyuk, R. N. Kleinman, D. J. Bishop, and F. Capasso. *Phys. Rev. Lett.*, 87:211801, 2001.

[25] F. Chen, U. Mohideen, G. L. Klimchitskaya, and V. M. Mostepanenko. *Phys. Rev. Lett.*, 88:101801, 2002.

[26] P. C. W. Davis. *Nature (London)*, 382:761, 1996.

[27] B. Derjaguin. *Kolloid-Z.*, 69:155, 1934.

[28] B. V. Derjaguin and I. I. Abricossova. *Sov. Phys. JETP*, 3:819, 1957.

[29] B. V. Derjaguin and I. I. Abricossova. *Sci. Am.*, 203:47, 1960.

[30] B. V. Derjaguin, Y. I. Rabinovic, and N. V. Churaev. *Nature*, 272:313, 1978.

[31] I. D. Dzyaloshinskij, E. M. Lifshitz, and L. P. Pitaevskij. *Sov. Phys. JETP*, 10:161, 1960.

[32] I. D. Dzyaloshinskij, E. M. Lifshitz, and L. P. Pitaevskij. *Sov. Phys. Usp.*, 4:153, 1961.

[33] E. Elizalde and A. Romeo. *Am. J. Phys.*, 59:711, 1991.

[34] T. Emig. *Europhys. Lett.*, 62:466, 2003.

[35] T. Emig, A. Hanke, R. Golestanian, and M. Kardar. *Phys. Rev. Lett.*, 87:260402, 2001.

[36] T. Emig, A. Hanke, R. Golestanian, and M. Kardar. *Phys. Rev. A*, 67:022114, 2003.

[37] A. Erdelyi, W. Magnus, F. Oberhettinger, and F. G. Tricomi. *Higher Transcendental Functions*. Krieger, New York, Vol. 1, 1981.

[38] H. B. Chan et. al. *Scince*, 291:1941, 2001.

[39] P. Cvitanovic et al. *Chaos: Classical and Quantum*. Niels Bohr Insitute, Copenhagen, (www.chaosBook.org), 2003.

[40] W. H. Press et. al. *Numerical Recipes in Fortran*. Cambridge Univ. Press, 1992.

[41] P. P. Ewald. *Ann. d. Physik*, 49:1, 1916.

[42] K. Fujikawa. *Phys. Rev. D*, 23:2262, 1981.

[43] R. Garcia and M. H. W. Chan. *Phys. Rev. Lett.*, 83:1187, 1999.

[44] R. Garcia and M. H. W. Chan. *Phys. Rev. Lett.*, 88:086101, 2002.

[45] B. Geyer, G. L. Klimchitskaya, and V. M. Mostepanenko. *Phys. Rev. A*, 67:062102, 2003.

[46] H. Gies, K. Langfeld, and L. Moyaerts. *J. High Energy Phys.*, 06:018, 2003.

[47] D. Gingell and V. A. Parsegian. *J. Theor. Biol.*, 36:41, 1972.

[48] R. Golestanian and M. Kardar. *Phys. Rev. A*, 58:1713, 1998.

[49] R. Golestanian and M. Kardar. *Phys. Rev. Lett.*, 78:3421, 1998.

[50] A. Gonis and W. H. Butler. *Multiple Scattering in Solids*. Springer, New York, 2000.

[51] C. Gordon, D. L. Webb, and S. Wolpert. *Bull. Am. Math. Soc.*, 27:134, 1992.

[52] M. C. Gutzwiller. *J. Math. Phys. (N.Y.)*, 12:343, 1971.

[53] A. Hanke and M. Kardar. *Phys. Rev. E*, 65:046121, 2002.

[54] J. N. Israelachvili. *Intermolecular and Surface Forces*. Academic, London, 1992.

[55] J. N. Israelachvili and P. M. McGuigan. *Science*, 241:6546, 1990.

[56] C. Itzykson and J. B. Zuber. *Quantum field theory*. McGraw-Hill, New York, 1980.

[57] J. D. Jackson. *Classical Electrodynamics*. John Wiley & Sons, Inc., 1967.

[58] R. L. Jaffe and A. Scardicchio. *Phys. Rev. Lett.*, 92:070402, 2004.

[59] M. Kac. *Amer. Math. Monthly*, 73:1, 1966.

[60] M. Kardar and R. Golestanian. *Rev. Mod. Phys.*, 71:1233, 1999.

[61] G. L. Klimchitskaya. *Int. J. Mod. Phys. A*, 17:751, 2002.

[62] W. Kohn and N. Rostoker. *Phys. Rev. C*, 94:1111, 1954.

[63] J. Kohringa. *Physica (Amsterdam)*, 13:392, 1947.

[64] M. G. Krein. *Mater. Sb.*, 33:597, 1953.

[65] W. E. Lamb and R. C. Retherford. *Phys. Rev.*, 72:241, 1947.

[66] A. Lambrecht and S. Reynaud. *Phys. Rev. Lett.*, 84:5672, 2000.

[67] A. Lambrecht and S. Reynaud. *Eur. Phys. J. D*, 8:309, 2000.

[68] S. K. Lamoreaux. *Phys. Rev. Lett.*, 78:5, 1997.

[69] L. D. Landau and E. M. Lifshitz. *Electrodynamics of Continuous Media*. Pergamon Press, 1966.

[70] D. Langbein. *Solid State Comm.*, 12:853, 1973.

[71] H. Li and M. Kardar. *Phys. Rev. Lett.*, 67:3275, 1991.

[72] H. Li and M. Kardar. *Phys. Rev. A*, 46:6490, 1992.

[73] E. M. Lifshitz. *Sov. Phys. JETP*, 2:73, 1956.

[74] G. J. Maclay. *Phys. Rev. A*, 61:052110, 2000.

[75] A. M. Marvin and V. Celli. *Phys. Rev. B*, 50:14546, 1994.

[76] J. Mehra. *Physica*, 37:145, 1967.

[77] P. W. Milonni. *Phys. Rev. A*, 25:1315, 1981.

[78] P. W. Milonni. *The Quantum Vacuum*. Acad. Press, 1993.

[79] P. W. Milonni and P. B. Lerner. *Phys. Rev. A*, 46:1185, 1992.

[80] P. W. Milonni and M. L. Shih. *Phys. Rev. A*, 45:4241, 1992.

[81] K. A. Milton. *Phys. Rev. D*, 22:1441, 1980.

[82] K. A. Milton. *Phys. Rev. D*, 22:1444, 1980.

[83] K. A. Milton. *The Casimir Effect: Physical Manifestations of Zero-Point Energy*. World Scientific, 2001.

[84] K. A. Milton. *Proceedings of the 6th Workshop on Quantum Field Theory Under the Influence of External Conditions*. Paramus, NJ, Rinton Press, 2004.

[85] D. Mitchell, B. W. Ninham, and P. Richmond. *Biophys. J.*, 13:359, 1973.

[86] D. Mitchell, B. W. Ninham, and P. Richmond. *Biophys. J.*, 13:370, 1973.

[87] U. Mohideen and A. Roy. *Phys. Rev. Lett.*, 81:4549, 1998.

[88] G. T. Moore. *J. Math. Phys.*, 11:2679, 1970.

[89] V. M. Mostepanenko and I. Y. Sokolov. *Sov. Phys. – Dokl. (USA)*, 33:140, 1988.

[90] V. M. Mostepanenko and N. N. Trunov. *Sov. Phys. Usp.*, 31:965, 1988.

[91] V. M. Mostepanenko and N. N. Trunov. *The Casimir effect and its Applications*. Clarendon, Oxford, 1997.

[92] B. W. Ninham and V. A. Parsegian. *Biophys. J.*, 10:646, 1970.

[93] B. W. Ninham and V. A. Parsegian. *J. Theor. Biol.*, 31:405, 1971.

[94] C. W. Oseen. *Ann. d. Physik*, 48:1, 1915.

[95] J. T. G. Overbeek and M. J. Sparnaay. *Disc. Faraday Soc.*, 18:12, 1954.

[96] E. S. Sabisky and C. H. Anderson. *Phys. Rev. A*, 7:790, 1973.

[97] M. Schaden and L. Spruch. *Phys. Rev. A*, 58:935, 1998.

[98] M. Schaden and L. Spruch. *Phys. Rev. Lett.*, 84:459, 2000.

[99] K. Schram. *Phys. Lett. A*, 43:282, 1973.

[100] J. Schwinger. *Lett. Math. Phys.*, 1:43, 1975.

[101] J. Schwinger, L. L. DeRaad, and K. A. Milton. *Ann. Phys. (N.Y.)*, 115:1, 1978.

[102] M. J. Sparnaay. *Physica (Utrecht)*, 24:751, 1958.

[103] M. J. Sparnaay. *The Historical Background of the Casimir Effect*. Elsevier, Amsterdam, 1989.

[104] D. J. Toms. *Phys. Rev. D*, 35:3796, 1987.

[105] T. Ueno, S. Balibar, T. Mizusaki, F. Caupin, and E. Rolley. *Phys. Rev. Lett.*, 90:116102, 2003.

[106] P. H. G. M. van Blockland and J. T. G. Overbeek. *J. Chem. Soc. Faraday Trans.*, 74:2637, 1978.

[107] N. G. van Kampen, B. R. A. Nijboer, and K. Schram. *Phys. Lett.*, 26A:307, 1968.

[108] P. van Nieuwenhuizen and A. Waldron. *Phys. Lett. B*, 389:29, 1996.

[109] P. van Nieuwenhuizen and A. Waldron. *Proceedings of the String Conference, Imperial College, London*, 1996.

[110] E. J. W. Vervey and J. T. G. Overbeek. *Theory of the stability of Lyophobic Colloids*. Elsevier, Amsterdam, 1948.

[111] S. Weinberg. *Rev. Mod. Phys.*, 61:1, 1989.

Kurzzusammenfassung

Casimirkräfte sind fluktuationsinduzierte Kräfte. Wir untesuchen die elektrodynamische Casimirkraft, die von Quantenfluktuationen und thermischen Fluktuationen des elektromagnetischen Feldes erzeugt wird. Mit Hilfe der Pfadintegralquantisierung des elektromagnetischen Eichfeldes wird eine effektive Gaußsche Wirkung hergeleitet, die als Ausgangspunkt für die analytische und numerische Berechnung der Casimirkraft dient. Es werden keine Annahmen über die Unabhängigkeit der geometrieabhängigen und materialabhängigen Beiträge zur Kraft gemacht. Wir untersuchen den Limes flacher Platten und erhalten eine kompakte Darstellung der Lifshitzschen Theorie molekularer Kräfte [73]. Im Limes idealleitender Oberflächen läßt sich die Gaußsche Wirkung explizit angeben. Beide Grenzfälle werden auch im Rahmen der Skalarfeldquantisierung untersucht, die auf translationsinvariante Geometrien angewendet werden kann. Es wird eine nichtperturbative Methode entwickelt, um die Casimirkraft aus der Gaußschen Wirkung für periodisch deformierte, idealleitende Oberflächen numerisch zu berechnen. Die Ergebnisse zeigen zwei Skalenregime für die Casimirkraft als Funktion des Abstandes zwischen den Oberflächen, und ihrer Krümmung. Die Nichtadditivität der Casimirkraft als fluktuationsinduzierte Kraft wird durch die erhaltenen Resultate belegt. Weiterhin wird die numerische Methode auch zur Berechnung der lateralen Casimirkraft zwischen periodisch deformierten Oberflächen verwendet. In bekannten Limites sind unsere Ergebnisse konsistent mit denen anderer Approximationsverfahren, wie der "proximity force approximation" im Falle großer Deformationswellenlängen, bzw. kleiner Oberflächenkrümmung. Es zeigt sich ein qualitativ unterschiedliches Verhalten zwischen der normalen und lateralen Kraft. Darüberhinaus stellen wir eine Beziehung zwischen der Änderung der Zustandsdichte für die skalare Helmholtzgleichung durch die Anwesenheit von beliebig geformten Oberflächen und der Casimirwechselwirkung mit Hilfe der Pfadintegralmethode her. Für statisch deformierte Oberflächen läßt sich diese Beziehung in Form einer neuen Spurformel ausdrücken, die formal ähnlich ist zur sogenannten Krein–Friedel–Lloyd Formel [64]. Während letztere jedoch die Zustandsdichte über die $\mathbb{S}$–Matrix für Quantenstreuprozesse an Potentialen beschreibt, so wird die neue Spurformel auf die freie Greenfunktion, welche auf den Grenzflächen der Geometrie des Problems ausgewertet wird, angewandt. Diese letztere Formulieung ist nicht approximativ und somit exakt.

Erklärung

Ich versichere, daß ich die von mir vorgelegte Dissertation selbstständig angefertigt, die benutzten Quellen und Hilfsmittel vollständig angegeben und die Stellen der Arbeit – einschließlich Tabellen, Karten und Abbildungen –, die anderen Werken im Wortlaut oder dem Sinn nach entnommen sind, in jedem Einzelfall als Entlehnung kenntlich gemacht habe; daß diese Dissertation noch keiner anderen Fakultät oder Universität zur Prüfung vorgelegen hat; daß sie – abgesehen von den unten angegebenen Teilpublikationen – noch nicht veröffentlicht worden ist sowie, daß ich eine solche Veröffentlichung vor Abschluß des Promotionsverfahrens nicht vornehmen werde. Die Bestimmungen dieser Promotionsordnung sind mir bekannt. Die von mir vorgelegte Dissertation ist von Herrn Dr. Thorsten Emig betreut worden.

Köln, den 4. Mai 2005

Rauno Büscher

Teilpublikationen

- Thorsten Emig, Rauno Büscher,
  Towards a theory of molecular forces between deformed media,
  Nucl. Phys. B **696**, 468, (2004).

- R. Büscher and T. Emig,
  Nonperturbative approach to Casimir interactions in periodic geometries,
  Phys. Rev. A **69**, 062101, (2004).

- R. Büscher and T. Emig,
  Geometry and Spectrum of Casimir forces,
  Phys. Rev. Lett. **94**, 133901, (2005).

Danksagung

Mein Dank gilt

- Thorsten Emig, der diese Arbeit ermöglicht und betreut hat, und der mir stets wegweisend zur Seite stand,
- Alexander Altland und Achim Rosch als Referenten,
- Michael Lässig für das Quartier, iMac und Telefonanschluss inklusive,
- Frau S. Esser vom Dekanat der Universität zu Köln für ihre Hilfe und Kooperationsbereitschaft,
- den Leuten aus der Arbeitsgruppe, Bernd Rosenow, Simon Bogner, Andreas Glatz, Yin Jiang, Frank Krüger, Stefan Scheidl und Sergey Malinin, Andreas danke ich insbesondere für seine Hilfe in Computerfragen,
- Peter Jung für seine Unterstützung beim Foliendrucken,
- Philipp Messer und Stana Willmann für die gute Atmosphäre und interessante Diskussionen auch jenseits der Physik in der gemeinsamen Zeit im Büro,
- meiner Mutter, Isolde Büscher, für ihre Unterstützug und Anteilnahme aus der Ferne,
- Daniel Martin, Michael Masa und Fabian Scharf für die gemeinsamen Unternehmungen und die vielen Gespräche, die mir in einer schwierigen Zeit sehr geholfen haben.

Rauno Büscher
Institut für theoretische Physik, Zülpicher Straße 77, 50677 Köln
Tel.: 0221-4703608, E-mail: rb@thp.uni-koeln.de

LEBENSLAUF

PERSÖNLICHE DATEN

Name:	Rauno Büscher
Geburtstag/-ort:	2. April 1974, Göttingen

AUSBILDUNG

ab Februar 2002	Promotion in theoretischer Physik, Universität zu Köln
Juli 2001	Diplom in theoretischer Physik Betreuer der Diplomarbeit: Prof. Dr. K. Schönhammer Titel: Renormierungstheorie wechselwirkender Fermionen in einer Dimension
Oktober 1997	Vordiplom Physik
Juli 1997	Vordiplom Mathematik
WS 1995/96 - SS 2001	Studium der Physik, Universität Göttingen
WS 1995/96 - SS 1997	Studium der Mathematik, Universität Göttingen
Oktober 1994	Abitur
1990 - 1994	Alexander-von-Humboldt Schule, Lima, Peru